INVESTIGATION OF GEOMETRY, ENERGETICS AND ELECTRONIC STRUCTURE OF TWISTED BILAYER GRAPHENE

A THESIS SUBMITTED TO

THE GRADUATE SCHOOL OF ENGINEERING AND SCIENCE

OF BILKENT UNIVERSITY

IN PARTIAL FULFILLMENT OF THE REQUIREMENTS FOR

THE DEGREE OF

MASTER OF SCIENCE

IN

PHYSICS

By

Nouha Amine

August 2024

INVESTIGATION OF GEOMETRY, ENERGETICS AND ELECTRONIC STRUCTURE OF TWISTED BILAYER GRAPHENE
By Nouha Amine
August 2024

We certify that we have read this thesis and that in our opinion it is fully adequate, in scope and in quality, as a thesis for the degree of Master of Science.

Oğuz Gülseren(Advisor)

Haldun Sevinçli

Bekir Sıtkı Kandemir

Approved for the Graduate School of Engineering and Science:

Orhan Arıkan
Director of the Graduate School

ABSTRACT

INVESTIGATION OF GEOMETRY, ENERGETICS AND ELECTRONIC STRUCTURE OF TWISTED BILAYER GRAPHENE

Nouha Amine
M.S. in Physics
Advisor: Oğuz Gülseren
August 2024

Twisted bilayer graphene (TBG) manifests unique electronic properties that hold substantial potential for advancements in nanotechnology, material science, and quantum computing. In this thesis, critical insights into the fundamental characteristics of TBG are uncovered through an in-depth exploration of its geometric configurations, interlayer interactions, and electronic properties.

We begin our investigation with a thorough analysis of the geometrical properties of the twisted bilayer graphene. By plotting the unit cell size against twist angles, we uncover distinct patterns and symmetries that emerge at different angles, offering insights into the fundamental structural properties that influence the material's behavior.

Following this, we examine the interlayer energies using both Lennard-Jones (LJ) and Kolmogorov-Crespi (KC) potentials. Our analysis of local stacking configurations reveals that the interlayer energy remains invariant due to the averaging contributions from AA and AB regions.

We then analyze the band structures across various twist angles using tight-binding calculations, computing parameters such as Fermi velocity and effective mass of the electrons. We observe the emergence of flat bands at "magic angles" and other unique band structures at specific twist angles, highlighting the complex electronic behavior of TBG.

Keywords: Twisted Bilayer Graphene, Moiré Pattern, Lennard-Jones Potential, Kolmogorov-Crespi Potential, Local Stackings, Tight-binding, Band Structure..

ÖZET

BÜKÜLMÜŞ İKİ KATMANLI GRAFENİN GEOMETRİSİNİN, ENERJİTİK VE ELEKTRONİK YAPISININ İNCELENMESİ

Nouha Amine
Fizik, Yüksek Lisans
Tez Danışmanı: Oğuz Gülseren
Ağustos 2024

Bükülmüş çift katmanlı grafen (TBG), nanoteknoloji, malzeme bilimi ve kuantum hesaplama alanlarındaki önemli ilerlemeler için büyük potansiyele sahip benzersiz elektronik özellikler sergiler. Bu tez çalışmasında geometrik konfigürasyonları, katmanlar arası etkileşimleri ve elektronik özellikleri derinlemesine incelenerek, TBG'nin temel özelliklerine dair kritik öngörüler ortaya çıkarılmaktadır.

Araştırmamıza, bükülmüş çift katmanlı grafenin geometrik özelliklerinin ayrıntılı bir analizi ile başlanmıştır. Birim hücre boyutunu bükülme açılarına karşı grafiğe dökerek, farklı açılarda ortaya çıkan belirgin desenleri ve simetrileri incelenmiştir. Bu, malzemenin davranışını etkileyen temel yapısal özellikleri hakkında öngörüler sunmaktadır.

Bunu takiben, hem Lennard-Jones (LJ) hem de Kolmogorov-Crespi (KC) potansiyellerini kullanarak katmanlar arası enerjiler incelenmiştir. Yerel istiflenme konfigürasyonlarının analizi, AA ve AB bölgelerinin ortalama katkılarından dolayı katmanlar arası enerjinin sabit kaldığını ortaya koymaktadır.

Daha sonra, sıkı bağ hesaplamalarını kullanarak çeşitli bükülme açıları boyunca bant yapılarını analiz edilmektedir. Fermi hızı ve elektronların etkin kütlesi gibi parametreleri hesaplanmıştır. "Sihirli açılar"da düz bantların ortaya çıkışı ve belirli bükülme açılarında diğer benzersiz bant yapıları gözlemlenmiş ve böylece TBG'nin karmaşık elektronik davranışı ortaya konulmuştur.

Anahtar sözcükler: Bükülmüş Çift Katmanlı Grafen, Moiré Deseni, Lennard-Jones Potansiyeli, Kolmogorov-Crespi Potansiyeli, Yerel İstiflenmeler, Sıkı Bağ, Bant Yapısı.

Acknowledgement

I would like to extend my heartfelt gratitude to my advisor, Prof. Oğuz Gülseren, for providing me with this invaluable opportunity and for his unwavering guidance, kindness, and patience throughout my academic journey.

I am profoundly grateful to my family—to my father for always believing in me and being my biggest supporter, and to my mother for her unconditional love and support, which have been the foundation of my achievements. This thesis would not have been possible without my backbone, my family.

I am also immensely thankful for the family I gained along the road, my friends. Thank you for being the best support I could ever ask for and for standing by my side through both hardships and ease.

I would also like to extend my gratitude to everyone who helped me during this journey, especially my friends from the department who always provided assistance whenever needed.

Lastly, I would like to recognize the TUBITAK ULAKBIM, High Performance and Grid Computing Center (TRUBA resources), where some of the numerical calculations reported in this paper were conducted.

Contents

List of Figures

Chapter 1

Introduction

When two periodic structures are overlaid with a slight misalignment, they generate a Moiré pattern, leading to intricate interference patterns with significant scientific implications. This pattern significantly alters the material's atomic structure and electronic properties, leading to unprecedented phenomena such as superconductivity and correlated insulating states. This effect is prominently observed in twisted bilayer graphene (TBG), where the unique electronic behavior at specific 'magic angles' has opened a new frontier in condensed matter physics.[1]

Graphene, an isolated single layer of graphite, is a two-dimensional material composed of carbon atoms arranged in a honeycomb lattice, as shown in Figure 2.1. Graphene exhibits sp^2 hybridization, with each carbon atom possessing four valence electrons; three of these electrons form σ bonds with adjacent atoms, while the fourth remains in the $p_z(\pi)$ orbital, perpendicular to the graphene plane. These p_z orbitals overlap with those of neighboring carbon atoms, creating delocalized π bonds that contribute to the material's unique electronic properties.[2]

Twisted bilayer graphene is formed when two graphene layers are superimposed with one layer rotated relative to the other. This concept gained attention due to the discovery of extraordinary properties in bilayers of graphene twisted at small angles, leading to the inception of twistronics. Twistronics, the study of electronic

properties modulated by the twist angle between layers, has revealed that TBG demonstrates superconducting properties at specific 'magic angles,' making it crucial for quantum computing, as it helps in the development of qubits and various quantum devices.[3] Moreover, TBG exhibits high electron mobility and tunability, making it extremely useful for next-generation high-speed electronic devices and advanced optoelectronic applications.[1] Because of these properties, TBG holds immense promise for future technologies. Ongoing research continues to explore bilayer graphene's electronic properties at various twist angles, with a particular focus on magic angles, and the underlying energetics driving these phenomena remain a topic of discussion. Despite significant progress, gaps in understanding the energetics of TBG still exist.

This thesis aims to explore the geometric configurations and energetic landscape of twisted bilayer graphene, focusing on how variations in the twist angle influence its structural and electronic properties. Utilizing computational methods, this study examines the TBG structure at different angles, computes their corresponding energies through empirical potentials, and employs the Tight Binding method to explore the associated electronic structure and band gaps.

This thesis is divided into three main chapters. Chapter Two reviews the geometric structure of graphene and twisted bilayer graphene (TBG) across a wide range of twist angles, determining the size of their corresponding unit cells and investigating their variation with twist angle, thereby revealing emerging patterns. Following this, Chapter Three calculates the energies of TBG for the same range of angles using two distinct empirical potentials, while also exploring the local stacking configurations observed in structures with small twist angles. Thereafter, in Chapter Four, the tight binding model is employed to compute the electronic structure of various twisted bilayer graphene configurations, examining the band structures and identifying the flat bands that appear at the magic angles. Additionally, we calculated several key parameters and identified other unusual band structures. Finally, Chapter Five concludes with a summary of the key findings and outlines potential future research directions.

Chapter 2

Geometrical Properties of Twisted Bilayer Graphene

2.1 Structural Analysis

Exploring the lattice geometry of twisted bilayer graphene (TBG) is essential for understanding its unique properties and behavior. Our investigation begins with a review of the lattice structure of monolayer graphene, the fundamental building block of TBG, to unravel the complexities of this material. To build this foundation, we start by introducing the basis vectors of monolayer graphene.

$$\begin{aligned} \vec{a}_1 &= \left[\frac{\sqrt{3}}{2}a, \frac{1}{2}a\right] \\ \vec{a}_2 &= \left[\frac{\sqrt{3}}{2}a, -\frac{1}{2}a\right] \end{aligned} \tag{2.1}$$

where $a = \sqrt{3}a_0$ is the lattice constant of graphene, and $a_0 = 1.42\text{Å}$ is the carbon-carbon distance. The graphene lattice consists of two triangular sublattices, A and B, with the positions of these atoms determined using the lattice vectors:

$$\begin{aligned} \vec{R}_A &= m\vec{a}_1 + n\vec{a}_2 \\ \vec{R}_B &= \vec{R}_A + \vec{\delta} \end{aligned} \tag{2.2}$$

Where $\vec{\delta} = \frac{\vec{a_1}+\vec{a_2}}{3} = a_0\hat{i}$, indicating that the B atom is shifted from the A atom by $a_0\hat{i}$. In Figure 2.1, the primitive lattice vectors $\vec{a}_1$ and $\vec{a}_2$, along with an arbitrary lattice vector $\vec{R}_{mn}$ for $(m, n) = (2, -1)$, are depicted for monolayer graphene.

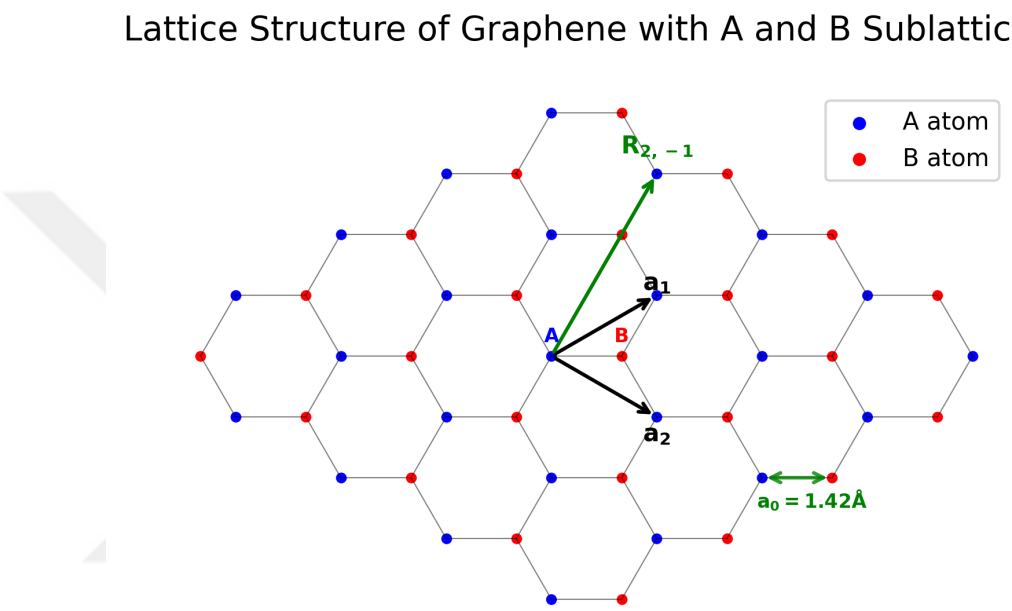

Figure 2.1: Lattice structure of monolayer graphene, illustrating the A and B sublattices, basis vectors, and lattice vector $\vec{R}_{2,-1}$.

Twisted bilayer graphene is created by rotating the top layer of an AA or AB stacked bilayer graphene around a rotation axis where atoms from both layers coincide, forming a larger periodic structure known as a superlattice. At certain twist angles, more atoms from the top and bottom layers align within the superlattice. These specific angles are referred to as commensuration angles, and the resulting superlattice structures are known as commensurate structures. Aiming to determine the rotation angles where these alignments occur, we utilize the fact that when atoms from both layers coincide, their corresponding lattice vectors must be of equal length.[4] We define these lattice vectors as follows:

$$\begin{aligned} \vec{R}^{(1)}_{mn} &= m\vec{a_1}^{(1)} + n\vec{a_2}^{(1)} \\ \vec{R}^{(2)}_{m'n'} &= m'\vec{a_1}^{(2)} + n'\vec{a_2}^{(2)} \end{aligned} \tag{2.3}$$

In these equations, $\vec{R}mn^{(1)}$ is the lattice vector for the atom in the bottom layer,

and $\vec{R}^{(2)}_{m'n'}$ denotes the lattice vector for the atom in the top layer. The vectors $\vec{a}^{(l)}$ denote the basis vectors, where l (1 or 2) refers to the corresponding layer. By utilizing the fact that these two vectors are equal and choosing a careful selection of lattice vectors, the indices (m', n') of the top layer lattice vector can be made equal to (n, m).[5] This choice will allow us to find the commensuration angles by using (m, n) parameters only.

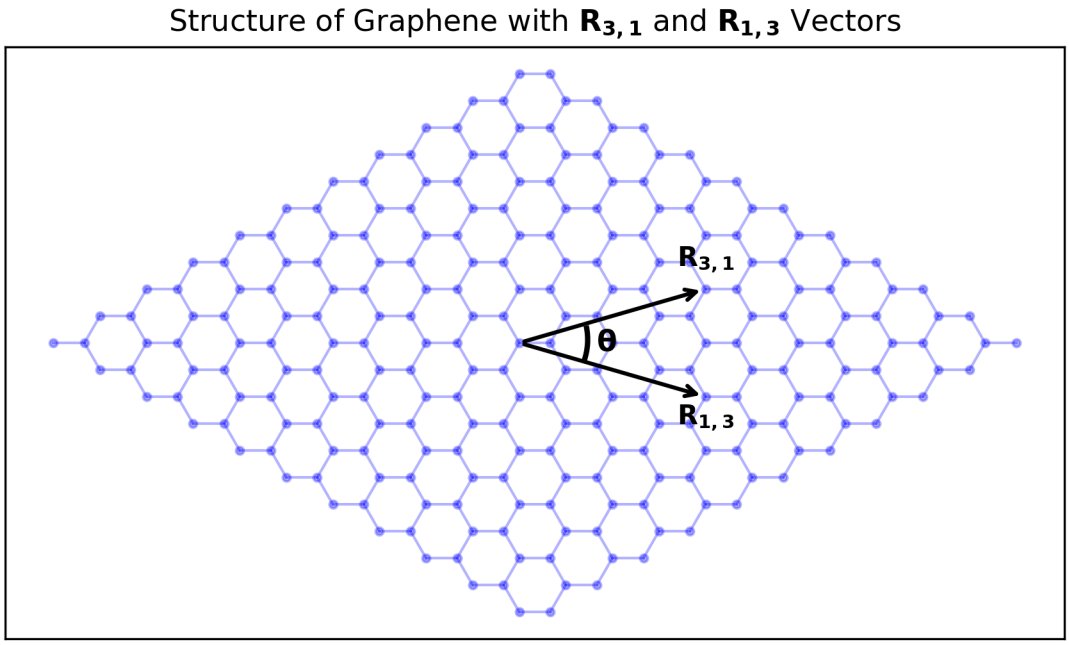

Figure 2.2: Monolayer graphene structure illustrating the two equal lattice vectors $\vec{R}_{mn}$ and $\vec{R}_{nm}$, with lattice parameters $(m, n) = (3, 1)$. The angle θ between these vectors is also depicted.

Figure 2.2 illustrates an example of these vectors, with $(m, n) = (3, 1)$. When the top layer is rotated by the angle θ, shown in the figure, in an anti-clockwise direction, the two lattice vectors coincide. This leads to the alignment of atoms from both layers at this site and at many other sites due to the lattice periodicity. The resulting superstructure is commensurate, and the rotation angle is a commensuration angle. This commensuration angle can be expressed as follows:

$$\cos(\theta) = \frac{\vec{R}^{(1)}_{mn} \cdot \vec{R}^{(2)}_{nm}}{|\vec{R}^{(1)}_{mn}||\vec{R}^{(2)}_{nm}|} = \frac{1}{2}\frac{m^2 + n^2 + 4mn}{m^2 + n^2 + mn} \tag{2.4}$$

Here, we obtained a periodic superlattice characterized by a primitive vector of $\vec{R}^{(1)}_{mn}$, with the second superlattice vector rotated by $\pi/3$ relative to it. Consequently, the superlattice vectors for the commensurate structures are defined as follows:

$$\begin{aligned} \vec{S_1} &= m\vec{a_1} + n\vec{a_2} \\ \vec{S_2} &= -n\vec{a_1} + (m+n)\vec{a_2} \end{aligned} \tag{2.5}$$

Figure 2.3 depicts these vectors for a twisted bilayer graphene structure with $(m, n) = (2, 1)$ and a twist angle $\theta = 21.787°$.

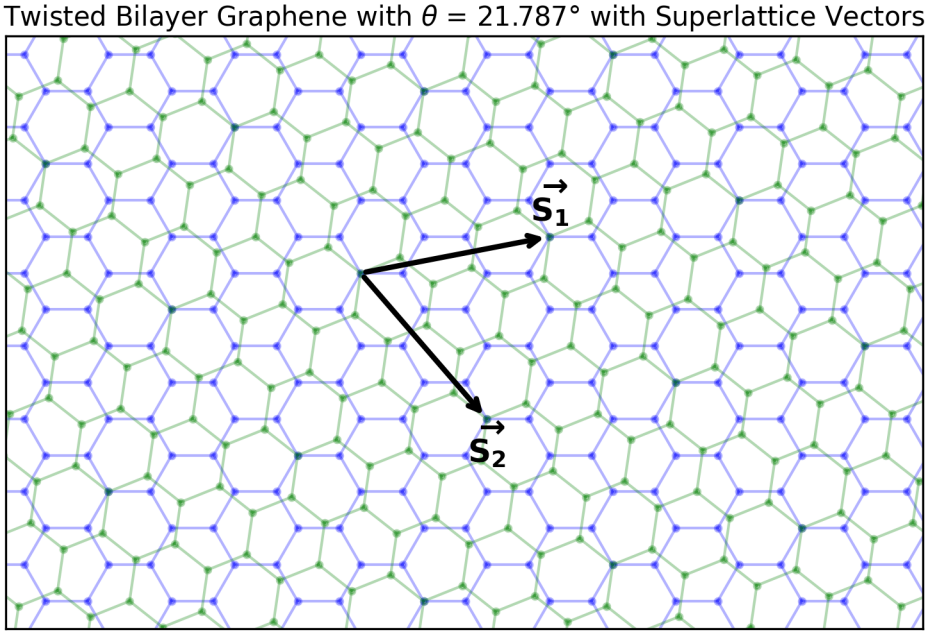

Figure 2.3: Superlattice vectors $\vec{S_1}$ and $\vec{S_2}$ for a twisted bilayer graphene structure with $(m, n) = (2, 1)$ and a twist angle of $\theta = 21.787°$.

Using these lattice vectors, we can construct the unit cell for the commensurate superlattices using only the (m, n) lattice parameters. The number of carbon atoms in these unit cells is given by:

$$N_C = 4 \times \frac{|\left(\vec{S_1} \times \vec{S_2}\right) \cdot \hat{z}|}{|\left(\vec{a}_1 \times \vec{a}_2\right) \cdot \hat{z}|} = 4(n^2 + nm + m^2). \tag{2.6}$$

The factor of 4 arises from the fact that we have two graphene layers, each containing two basis atoms.[4] Examples of these unit cells are shown in Figure 2.4.

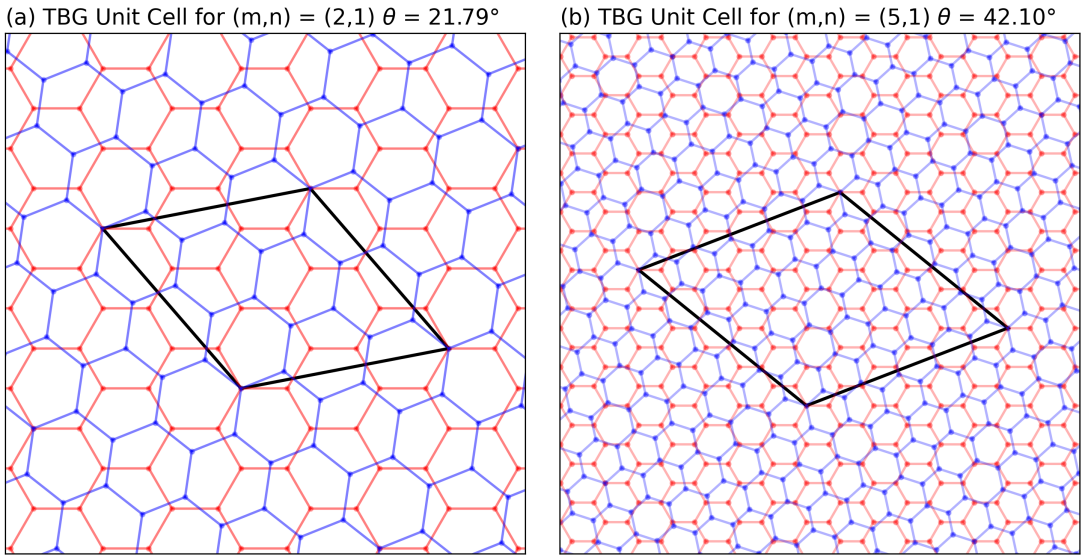

Figure 2.4: Twisted bilayer graphene unit cells for (a) $(m, n) = (2, 1)$ with a twist angle $\theta = 21.79°$; (b) $(m, n) = (5, 1)$ with a twist angle $\theta = 42.10°$.

The superlattice periodicity λ_c, is equal to the magnitude of the superlattice vector:

$$\lambda_c = \sqrt{m^2 + mn + n^2} \cdot a = \frac{|m - n|a}{2\sin(\theta_c/2)} \tag{2.7}$$

The minimum value of $|m - n|$ defines the primitive lattice vector of the Moiré superlattice, which corresponds to $|m - n| = 1$. Thus, the Moiré periodicity becomes [5]

$$\lambda_M = \frac{a}{2\sin(\theta_c/2)} \tag{2.8}$$

2.2 Sublattice Exchange Symmetries: SE-Even and SE-Odd Superlattices

Our next step is to examine various commensuration angles and their corresponding superlattices. During this investigation, we identified two distinct models of superlattices that emerge upon the rotation of twisted bilayer graphene. These models can be distinguished by their symmetries, particularly by their sublattice exchange symmetries. Accordingly, we classify these two models as sublattice exchange even (SE-even) and sublattice exchange odd (SE-odd) structures.[6] In SE-odd structures, four coinciding atoms are located at the corners of the unit cell. However, in SE-even unit cells, besides the four coinciding atoms at the corners, two B atoms from both layers also coincide within the cell. Building upon the methodology outlined in Reference [7], we understand that this condition is satisfied only when $|m-n|$ is divisible by three. Consequently, it can be inferred that when $|m-n|$ is divisible by three, the sublattice exchange symmetry is even (SE-even). The use of the superlattice vectors defined in Equation 2.5 proves inadequate for SE-even structures, as clearly illustrated in Figure 2.5(b), where $\vec{S}_1$ and $\vec{S}_2$ are plotted on an SE-even superlattice. For SE-even structures, the superlattice vectors can be defined as:

$$\begin{aligned} \vec{T}_1 &= \frac{(\bar{m}-\bar{n})}{3}\vec{a}_1 + \frac{(\bar{m}+2\bar{n})}{3}\vec{a}_2 \\ \vec{T}_2 &= \frac{(\bar{m}-2\bar{n})}{3}\vec{a}_1 + \frac{(2\bar{m}+\bar{n})}{3}\vec{a}_2 \end{aligned} \tag{2.9}$$

Where $(\bar{m}, \bar{n})$ are the lattice parameters corresponding to the SE-even unit cell. These vectors are also depicted in Figure 5(b). The number of carbon atoms per unit cell for an even structure can be defined as:

$$N_{\text{even}} = \frac{N_{odd}}{3} = \frac{4}{3}(\bar{n}^2 + \bar{n}\bar{m} + \bar{m}^2) \tag{2.10}$$

The corresponding periodicity of the even structure is given by:

$$\lambda_C = \frac{a}{2\sin\left(\frac{(\pi/3-\theta_C)}{2}\right)} \tag{2.11}$$

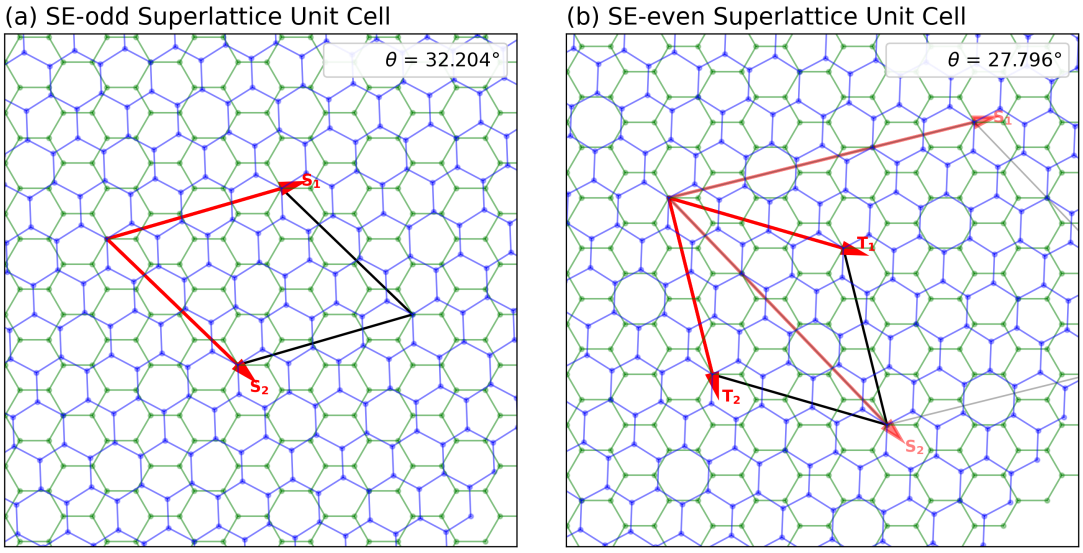

Figure 2.5: (a) TBG with a twist angle of $\theta = 32.204°$, displaying the SE-odd unit cell and its corresponding lattice vectors $\vec{S}_1$ and $\vec{S}_2$. (b) TBG with a twist angle of $\theta = 27.796°$, presenting the SE-even unit cell and demonstrating the inadequacy of $\vec{S}_1$ and $\vec{S}_2$, while showing the correct superlattice vectors $\vec{T}_1$ and $\vec{T}_2$.

Another notable observation is that for each lattice parameter pair $(\bar{m}, \bar{n})$, there exists a corresponding (m,n) pair that defines an SE-odd structure. The unit cells constructed from these two sets of parameters have equal areas and contain the same amount of carbon atoms. Furthermore, the sum of the twist angles associated with these pairs is 60°. These two structures are referred to as commensuration partners,[6] and a clear example of them is shown in Figure 2.5.

2.3 Graph Build-up

Utilizing the relevant information discussed in the previous sections, we employed the Python programming language to generate a graph illustrating the relationship between the size of the unit cell and the twist angle of twisted bilayer graphene. First, it is important to note that due to the intrinsic symmetry of

the graphene lattice, rotating a layer by $-\theta$ is equivalent to rotating it by θ. Additionally, a rotation by $2\pi/3$ (120°) returns the TBG to its original stacking, while a $\pi/3$ (60°) rotation transforms AA-stacked bilayer graphene into AB-stacked bilayer and vice versa. Taking these conditions into account, the study of TBG for angles between 0° and $\pi/3$ (60°) is sufficient and it provides a comprehensive approach to the understanding of TBG. Due to the sixfold symmetry of the trigonal sublattice, the TBG is expected to exhibit a mirror-image symmetry around the angle 30°.[5] To obtain this graph, we followed the methodology illustrated in the flowchart in Figure 2.6.

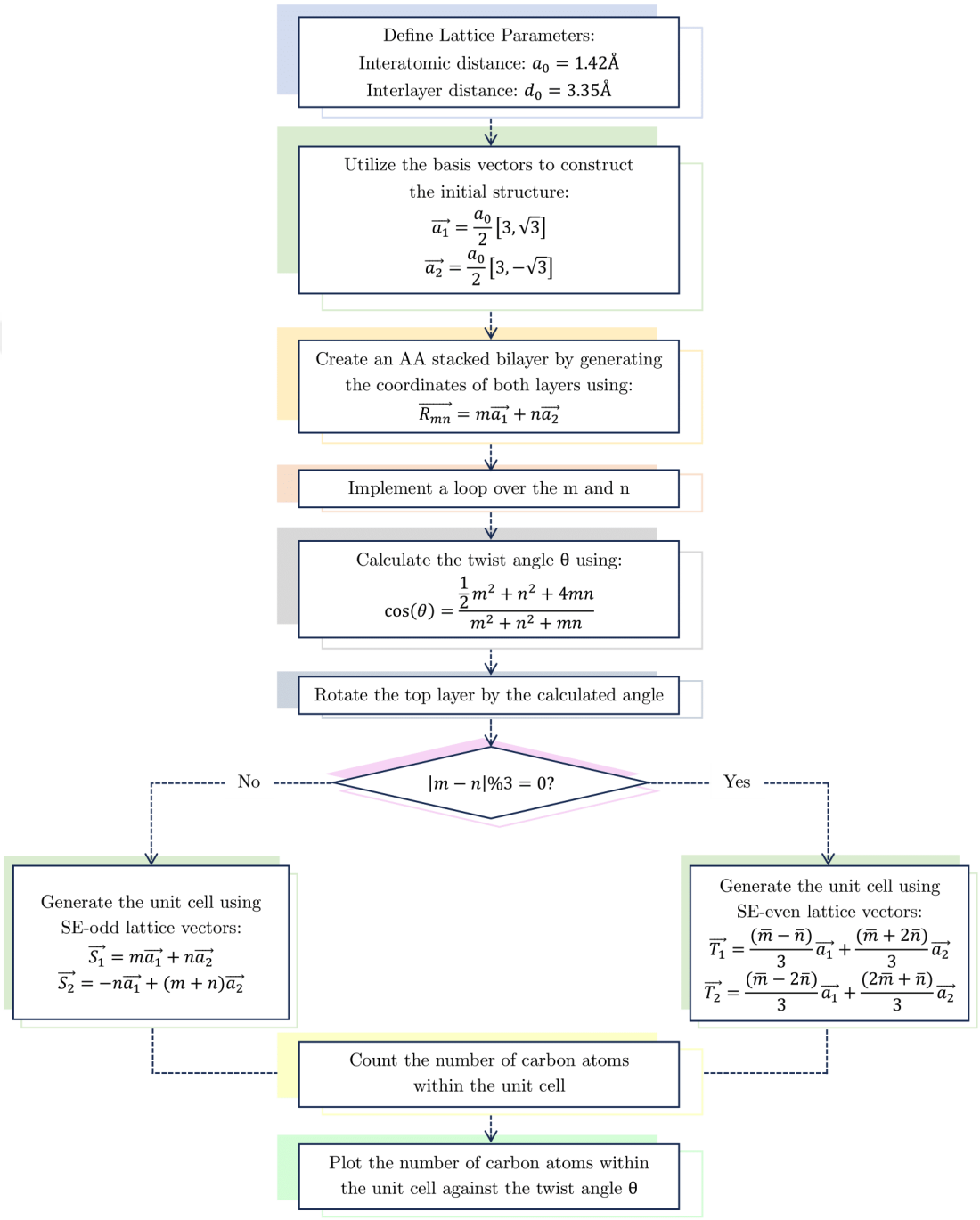

Figure 2.6: Flowchart illustrating the methodology used to obtain the graph of unit cell size versus twist angle.

Note that the size of the unit cell could also be found using N_C and N_{even}, as

given by the formulas in Equations 2.6 and 2.10. Our results are in agreement with these calculations and the generated plot is shown in Figure 2.7.

2.4 Graph Analysis

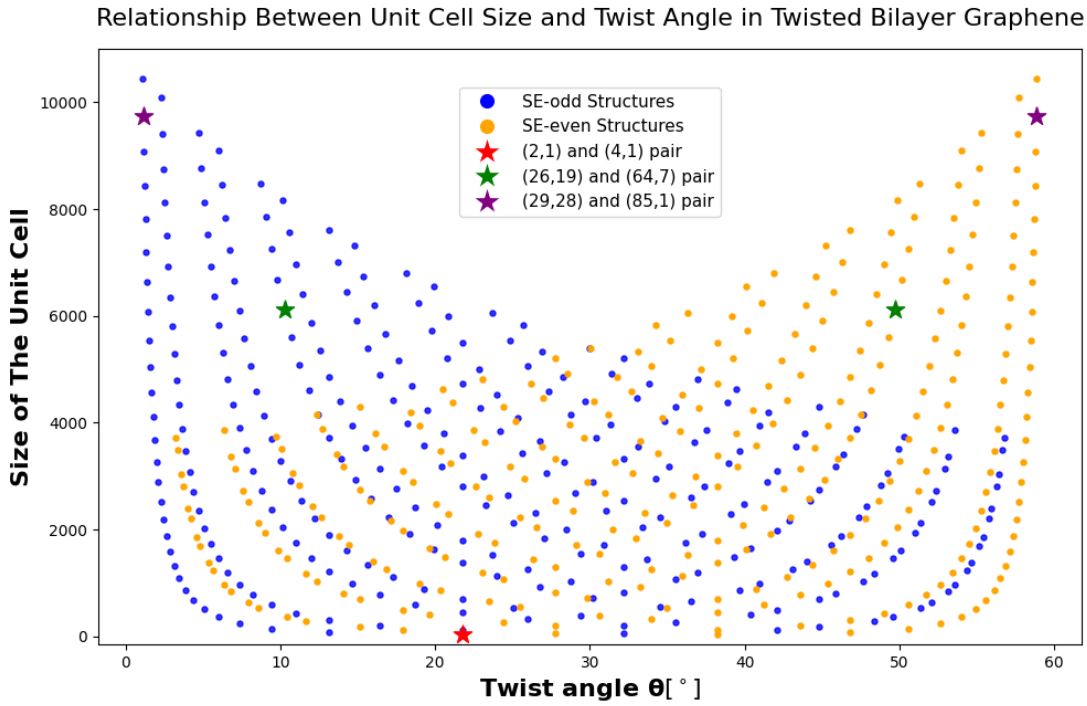

Figure 2.7: Plot of the unit cell size of TBG superlattices against the corresponding twist angles. Blue points represent SE-odd structured TBG, while orange points correspond to SE-even structured TBG. Star points indicate commensuration partners, with their specific parameters elucidated in the legend.

In Figure 2.7, the unit cell sizes of SE-even and SE-odd superlattices are plotted against their corresponding twist angles. Orange points represent SE-even structures, while blue points correspond to SE-odd structures. One of the initial observations from the graph is its symmetry around a rotation angle of 30°, as anticipated. Furthermore, the graph shows the largest unit cells at twist angles near 0° and 60°, while the smallest unit cells appear near 30°. Drawing upon

the knowledge from Section 2.3, it is understood that each unit cell has a commensuration partner with a combined twist angle of 60° and identical unit cell area. Examples include $(2, 1)$ and $(4, 1)$, $(6, 5)$ and $(16, 1)$, $(3, 1)$ and $(5, 2)$, $(5, 1)$ and $(7, 4)$, and $(5, 4)$ and $(26, 2)$. Some of these commensuration partners are highlighted in Figure 2.7. Additionally, rotating AA-stacked TBG by 60° results in an AB-stacked bilayer graphene structure. This symmetry allows us to deduce that reversing the graph represents the evolution from an AB-stacked bilayer structure at 0° to an AA-stacked bilayer structure at 60°. Another noteworthy observation from this graph is that small variations in rotation angles can give rise to structures of significantly different sizes and distinct physical properties. For instance, $(m, n) = (4, 3)$ with a rotation angle of 9.43° has 148 carbon atoms per unit cell, while $(29, 22)$ with a rotation angle of 9.06° has 7852 carbon atoms per unit cell. Although their rotation angles are close, the sizes of their corresponding structures differ significantly.

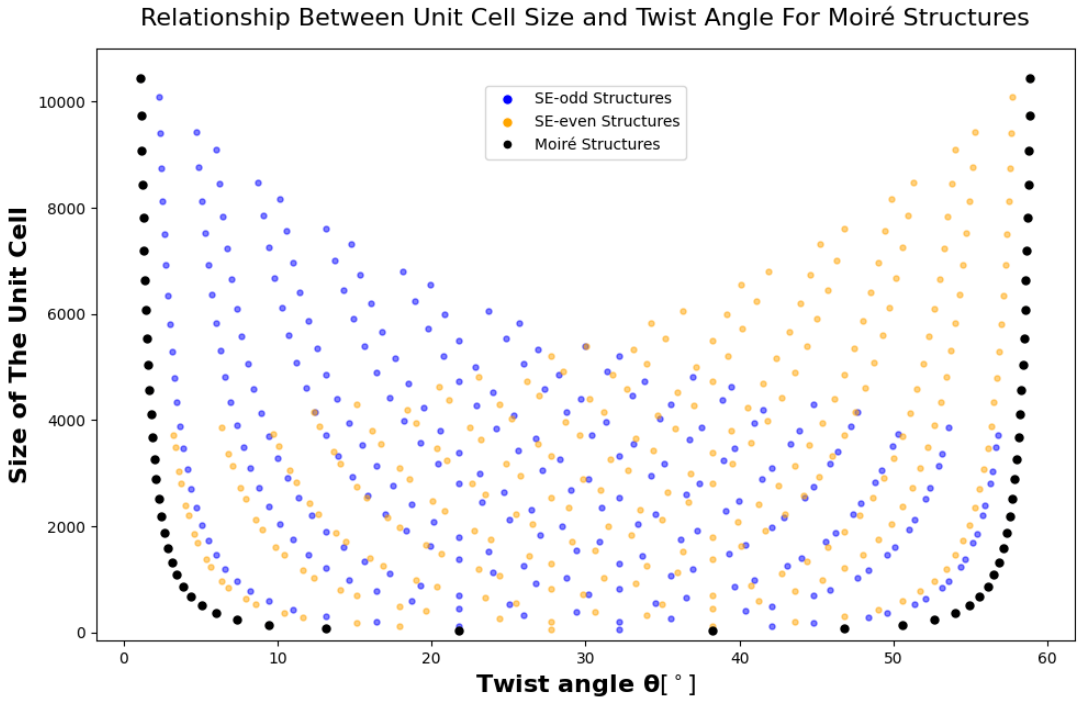

Figure 2.8: Plot of unit cell size as a function of twist angles, highlighting the curve defined by the Moiré equation.

As discussed in Section 2.3, TBG structures with $|m-n| = 1$ satisfy the Moiré equation. These structures, which are the smallest on the graph, are highlighted in Figure 2.8.

2.4.1 Patterns in SE-odd structure graph

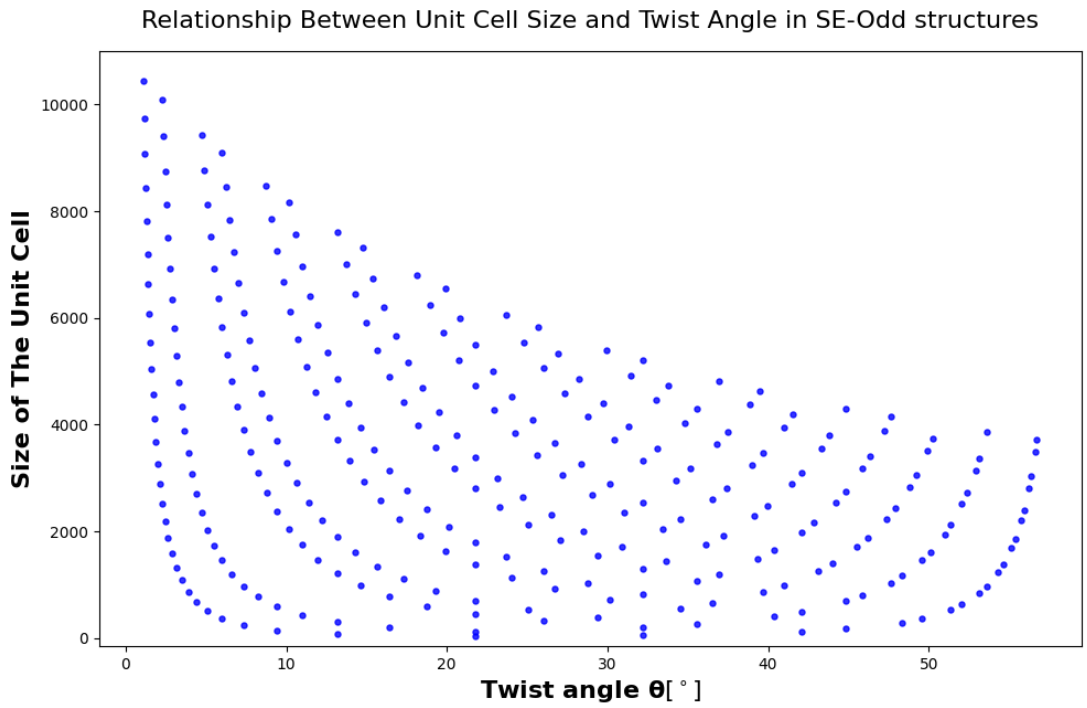

Figure 2.9: Graph depicting the relationship between unit cell size and twist angle for twisted bilayer graphene structures with SE-odd symmetry, where $|m-n|$ is not a divisor of 3.

In the next step of our analysis, we initiate a study to understand the relationship between the lattice parameters (m, n) and the variation of unit cell size with the twist angle. In preparation for our analysis, we present a plot in Figure 2.9 that illustrates the relationship between unit cell size and twist angle, exclusively for odd structures. Here, odd structures refer to the superlattice structures that exhibit SE-odd symmetry.

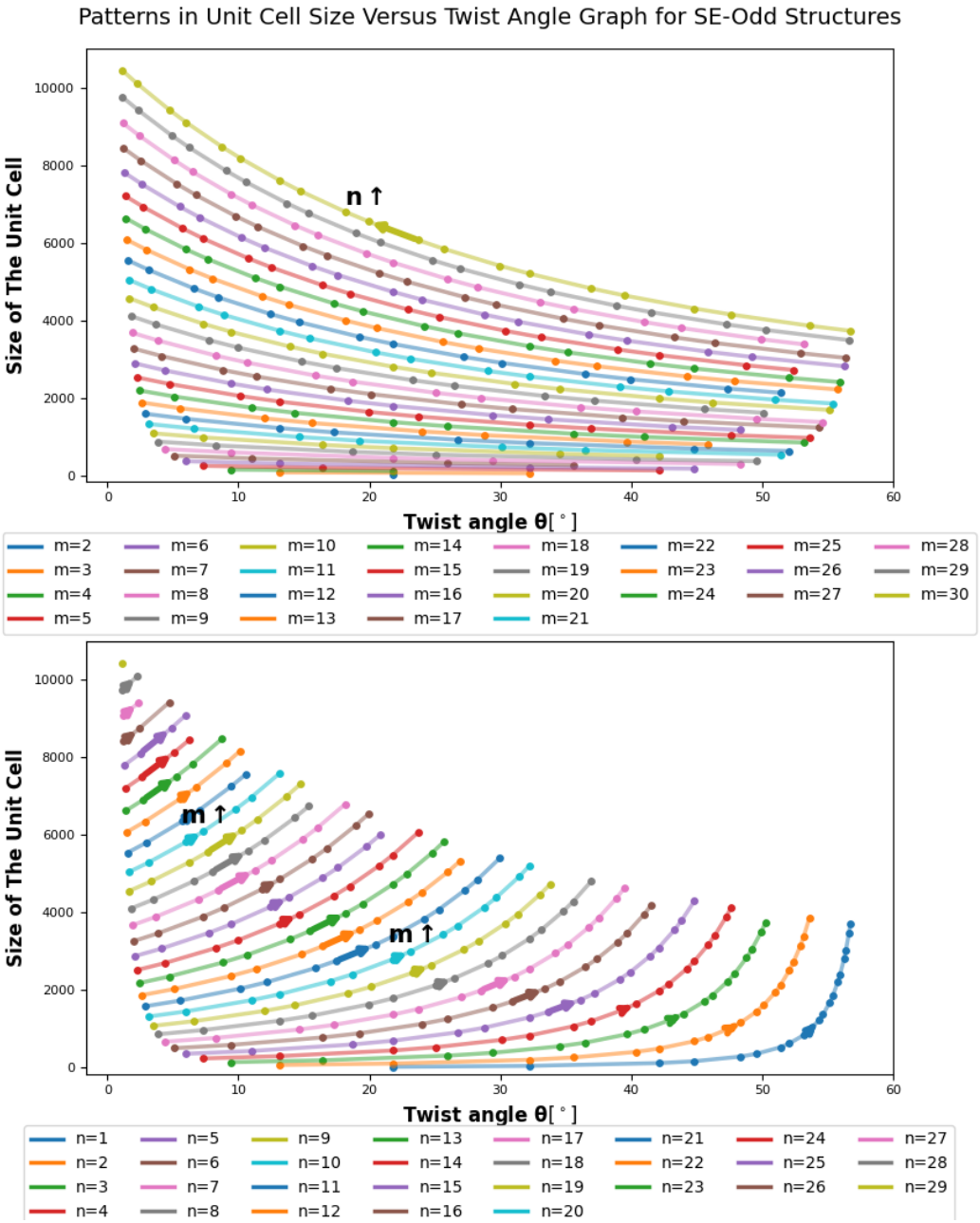

Figure 2.10: Plots illustrating the patterns in the unit cell size versus twist angle graph for SE-odd structures when (a) m value is fixed, where the arrow indicates the direction in which n is increasing (b) n value is fixed, where the arrow indicates the direction in which m is increasing. Legends display the corresponding m and n values.

Our first investigation examines the variation in unit cell size when one of the (m, n) parameters is held constant while the other varies. To illustrate these relationships, we plot lines connecting structures with one identical parameter. Two graphs depicting these patterns are presented in Figure 2.10. In Figure 2.10(a), the lines represent the patterns observed when the m value is fixed. From this analysis, we were able to draw several conclusions. Importantly, when m is held constant, increasing the n parameter leads to a decrease in the twist angle. Thus, for two structures with the same m value, the structure with the smaller n value exhibits a larger twist angle. Furthermore, for higher values of m, the unit cell size is more significantly affected by changes in n. It is also observed that when m is small, regardless of how high the n value is, the unit cell size remains small. This observation is particularly useful for obtaining smaller unit cells at specific angles to avoid computational challenges. By keeping the m value as small as possible, along a wide range of twist angles, we are able to identify smaller unit cells, thus optimizing computational efficiency and addressing many of the challenges associated with TBG's large unit cells. In Figure 2.10(b), the same analysis is conducted with a fixed n value while m varies. Here, the rotation angle increases with increasing m. Another observation is that when n is constant, the unit cell size is at its minimum for smaller θ values. From these plots, we can infer that knowing just one of the lattice parameters allows us to estimate their position on the plot. Additionally, by extending these linear trends, we can identify the optimal pair of lattice parameters that yield the smallest unit cell size and an angle that meets our specific requirements.

Moving forward in our analysis, we examined the patterns that emerge when scatter points corresponding to the same $|m - n|$ value are connected. These patterns are illustrated in Figure 2.11. Notably, structures where the $|m - n|$ values are multiples of 3 are absent, as these structures exhibit SE-even symmetry and are not included in this part of the analysis. The graph reveals that lower $|m - n|$ values correspond to smaller twist angles, consistent with the Moiré equation.

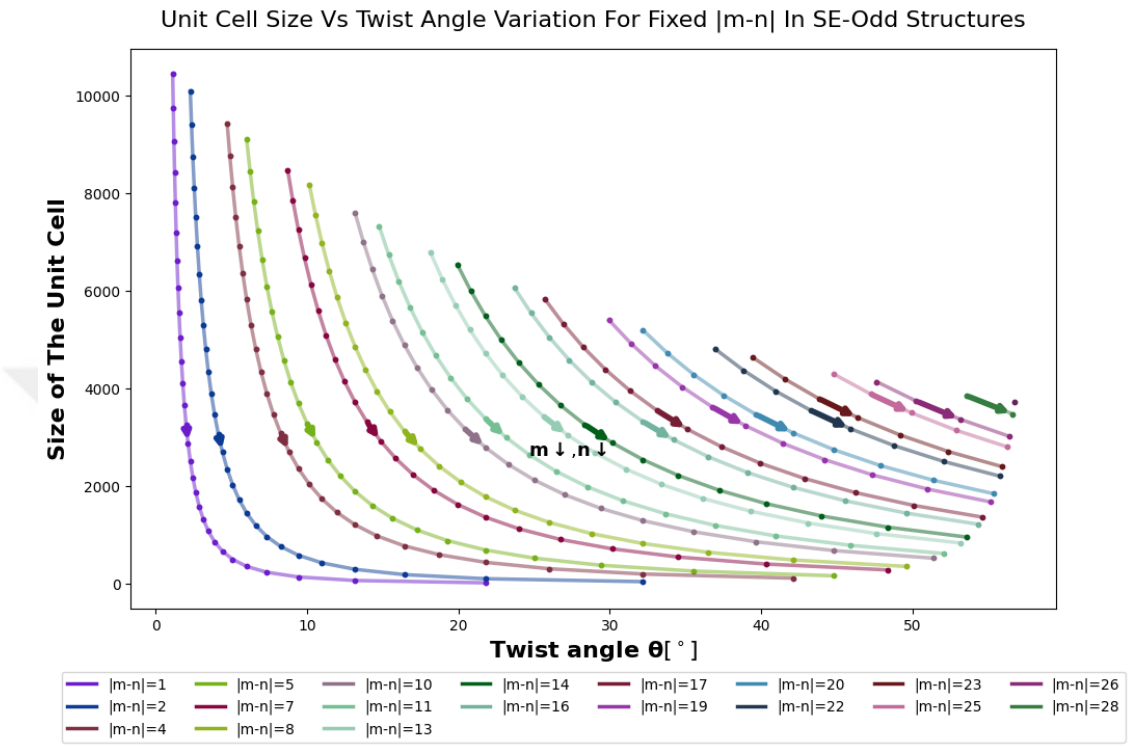

Figure 2.11: Plot illustrating the patterns in the unit cell size versus twist angle graph for SE-odd structures, where $|m-n|$ is held constant. The legend specifies the corresponding $|m-n|$ values.

Following this, we present three figures that reveal distinctive patterns detected while systematically varying the lattice parameters by constant amounts. In Figure 2.12(a), we examine the changes in both unit cell size and twist angle as both n and m increase by one at each step. This graph shows that as both lattice parameters increase, the twist angle decreases while the unit cell size increases.

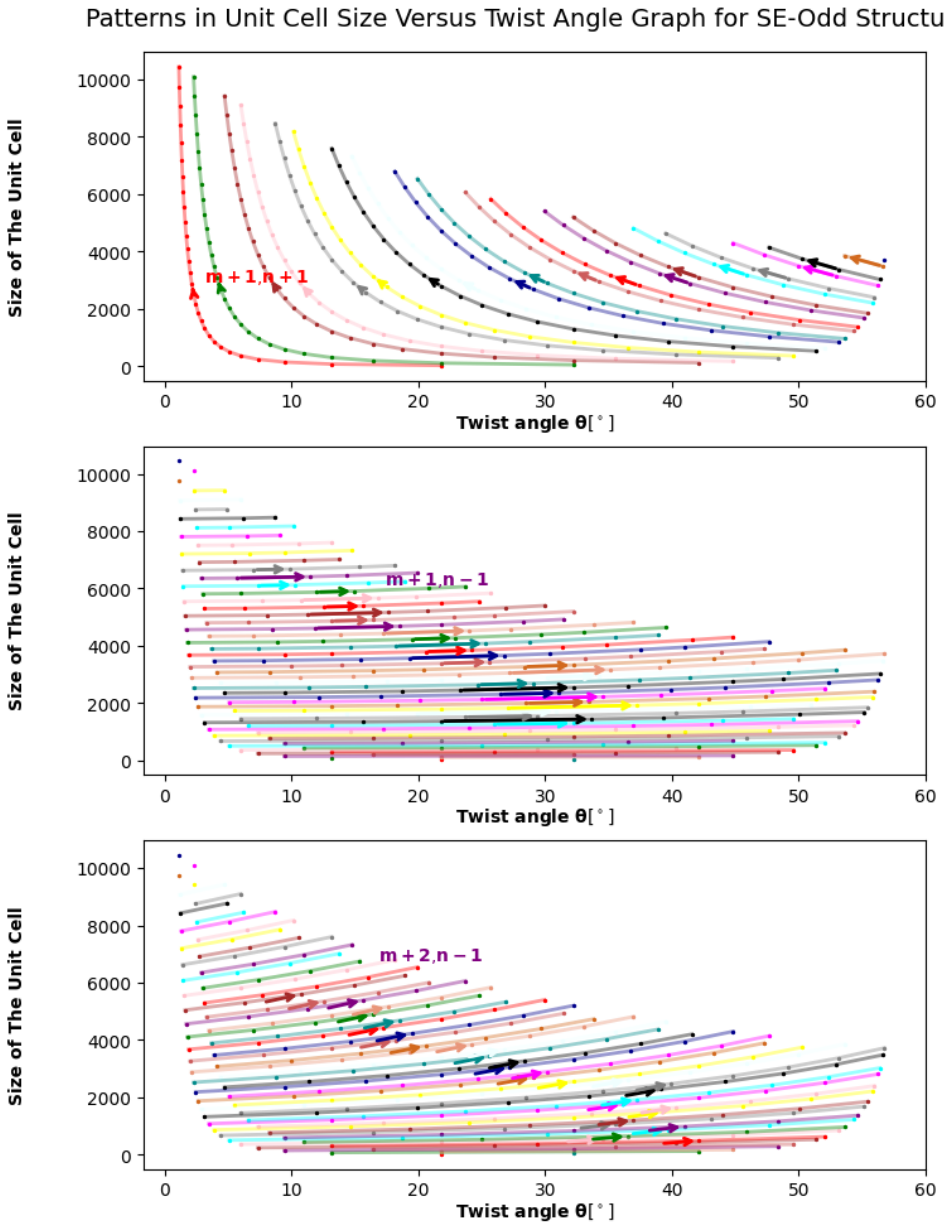

Figure 2.12: Impact of (m, n) variations on twist angle and unit cell size in SE odd structures, in (a) both m and n increase by 1, in (b) m increases by 1, and n decreases by 1, in (c) m increases by 2, and n decreases by 1.

In Figure 2.12(b), we examine the impact of varying (m, n) pairs by increasing m by 1 and decreasing n by 2. During this variation, the rotation angle gradually increases. A notable finding is that the change in unit cell size is minimal. For

instance, one of the lines in our graph connects the structure $(24, 23)$ with a size of 6628 atoms per unit cell and $(30, 17)$ with a size of 6796 atoms per unit cell. The difference in size between these two structures is only 168, which is relatively small compared to the overall size of the unit cell. This suggests that the increase in m compensates for the decrease in n, neutralizing the effect of angle variation on unit cell size. In Figure 2.12(c), we analyze the effects of increasing m by 2 and decreasing n by 1 at each step. As these modifications are implemented, we observe that while the twist angle increases, the size of the unit cell gradually increases. The magnitude of the change in size is larger compared to what we observed in Figure 2.12(b).

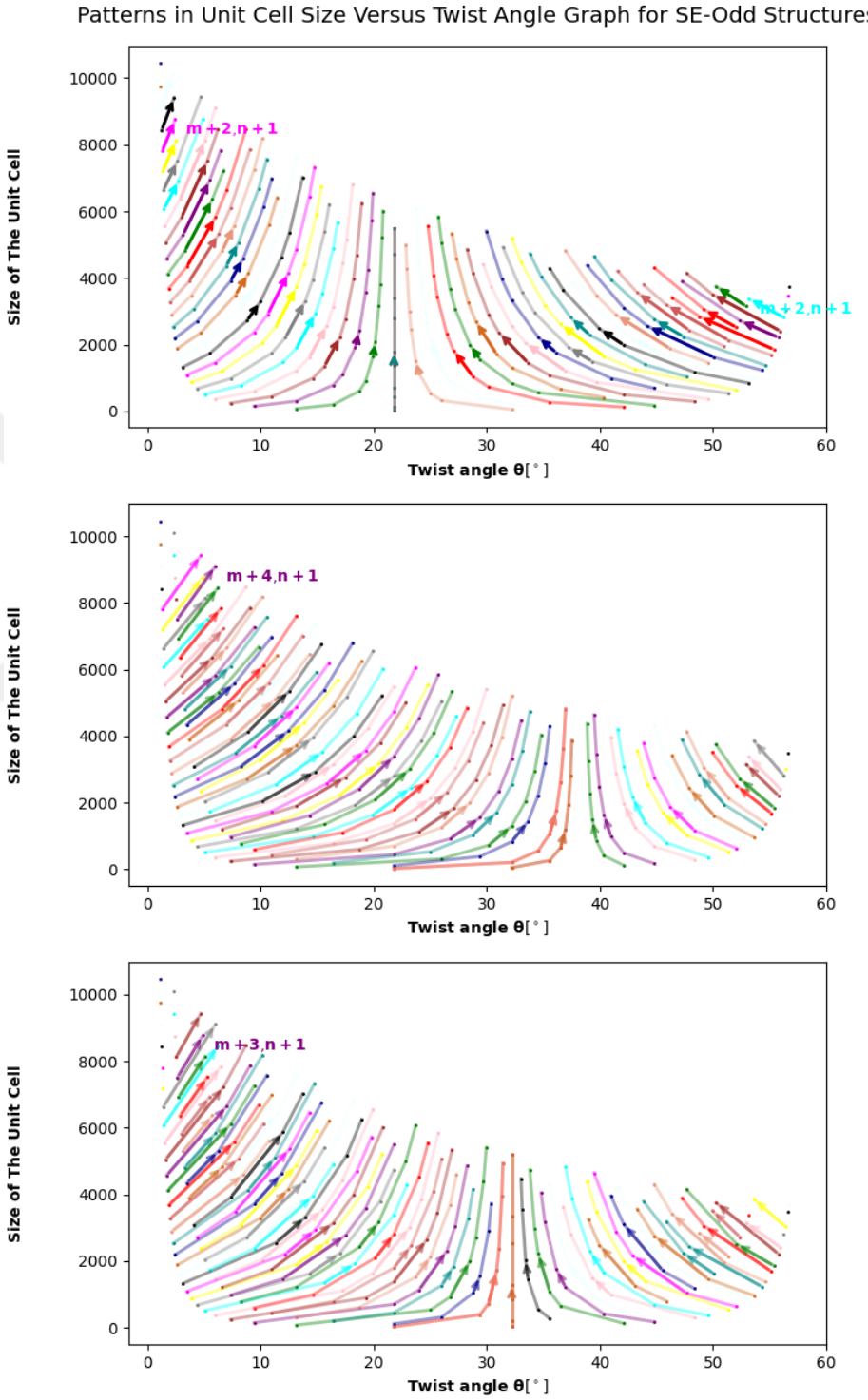

Figure 2.13: Influence of (m, n) variations on twist angle and unit cell size in SE odd structures. The (m, n) increments are as follows: (a) $(2, 1)$, (b) $(4, 1)$, and (c) $(3, 1)$. In each case, the lines converge toward a specific angle.

In Figure 2.13, we present three graphs illustrating the variations in unit cell size and twist angle as the parameters m and n increase by distinct values. These graphs reveal several intriguing patterns. For instance, in Figure 2.13(a), increasing the (m, n) values by $(2, 1)$, respectively, results in the convergence of the pattern towards an angle of 21.787°. Notably, twisted bilayer graphene structures at this twist angle follow a specific equation defining the relationship between their lattice parameters, where m equals twice n ($m = 2n$). In Figure 2.13(b), we examine the effects of increasing m by 4 and n by 1. The results demonstrate a convergence pattern similar to that observed in Figure 2.13(a), towards an angle of 38.213°, in this case. Here, the angle corresponds to structures whose lattice parameters follow the equation $m = 4n$. These structures are not plotted due to their SE-even structure. In Figure 2.13(c), a similar convergence pattern was identified when m increased by 3 and n increased by 1. The lines converged to an angle of 32.204°. As anticipated from the preceding figures, this angle corresponds to the twisted bilayer graphene structures where $m = 3n$. Several general conclusions can be drawn from this figure. Notably, when a line connects the twisted bilayer graphene structures that increase by a constant amount of (x, y), the pattern lines converge to an angle corresponding to structures with lattice parameters obeying the equation of $m = \frac{x}{y}$n. From this observation, we can also infer that the line trajectories connecting structures with increments of $(5, 1)$ and $(6, 1)$ will converge to the twist angles corresponding to TBG structures following the equations $m = 5n$ and $m = 6n$, respectively. This behavior can also be seen in Figure 2.12(a), where the patterns followed an increment of $(1, 1)$, we observed a convergence toward an angle of 0°. This angle corresponds to structures obeying the equation $m = n$, reinforcing our drawn conclusion.

2.4.2 Patterns in SE-even structure graph

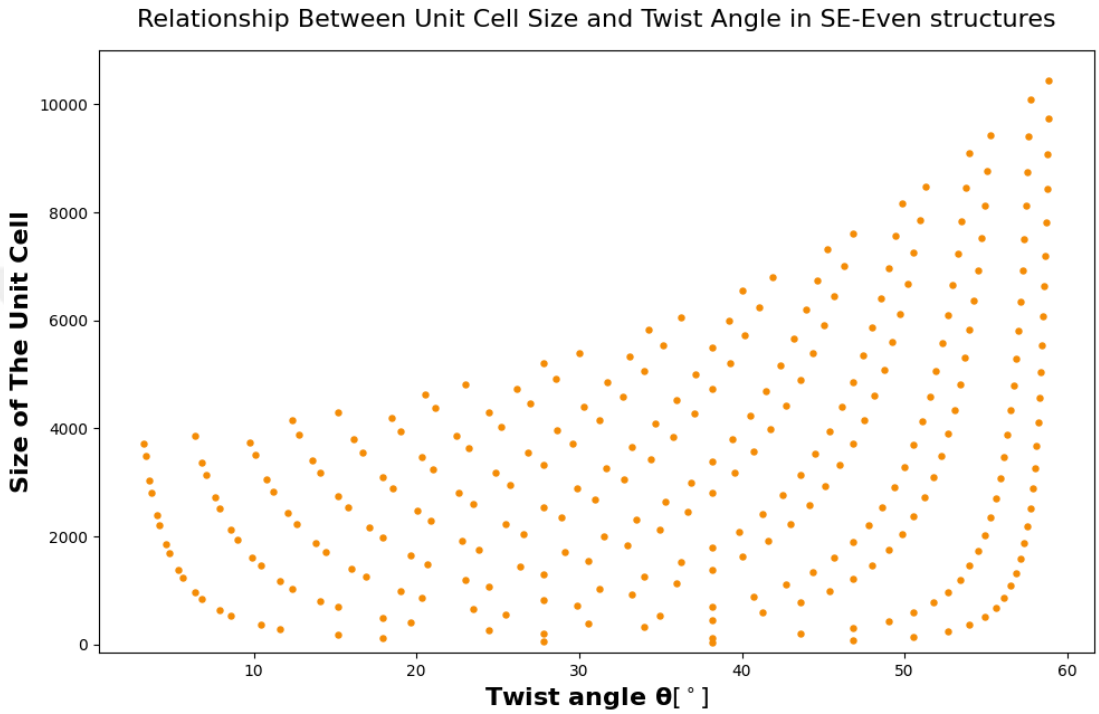

Figure 2.14: Plot illustrating the relationship between unit cell size of TBG and twist angle, exclusively for unit cells exhibiting SE-even symmetry, where $|m-n|$ is a divisor of 3.

After analyzing the pattern observed in SE-odd structures, we move our focus to SE-even structures. We start by plotting the relationship between unit cell size and twist angle for SE-even structures, referring to TBG configurations with SE-even symmetry. This plot is presented in Figure 2.14.

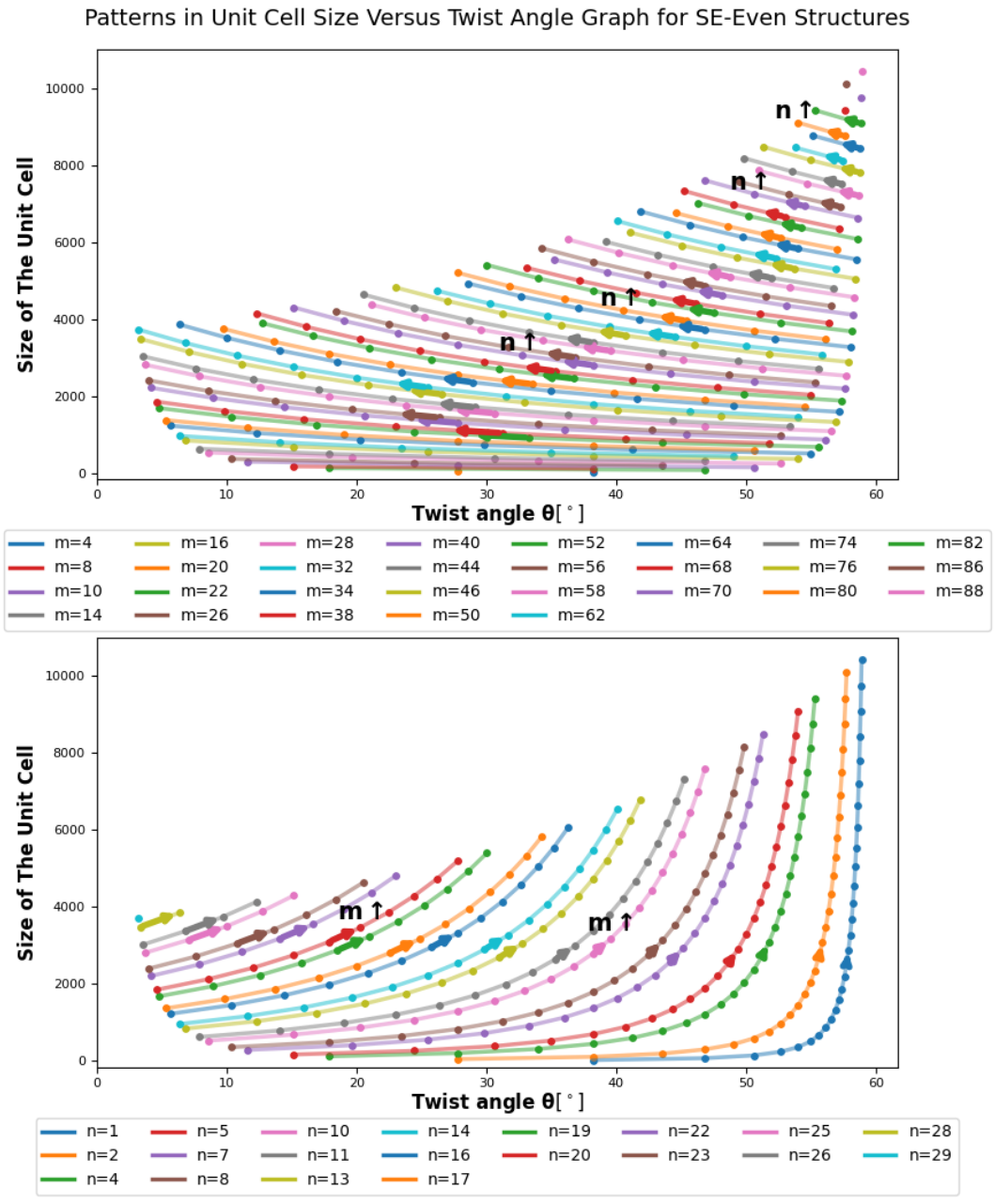

Figure 2.15: Plots illustrating the patterns in the variation of unit cell size with twist angle when one of the two lattice parameters is held constant: (a) m is held constant, with arrows indicating the direction of increasing n; (b) n is held constant, with arrows indicating the direction of increasing m.

For these structures, we similarly analyze the relationship between the lattice

parameters and the unit cell size versus twist angle variation, holding one of the lattice parameters of the even structures constant. In Figure 2.15(a), with m fixed and n varying, we observe a behavior similar to that shown in Figure 2.10(a), where n decreases with the increase of the twist angle. In Figure 2.15(b), we hold n constant and vary m. In this figure, we observe a pattern of exponential growth in unit cell size as the twist angle approaches 60°. We conclude that this behavior is symmetric to that seen in Figure 2.11, which exhibited exponential growth in size as m and n values decreased near 0°. The legends in the figures display the corresponding m and n values. Based on the analysis of Figure 13 in the previous section, we notice that this graph obeys the same rule. Here, n is held constant, so its increment is zero, while m increases by one in each step. It can be observed that the pattern lines converge towards an angle of 60°, which corresponds to TBG structures with a null n lattice parameter. These structures obey the equation $n = 0m$. Another observation from this figure is that in even structures, the m values span a much larger range than the n values, highlighting an interesting behavior. From these observations and Figure 2.10, we conclude that the m parameter has a greater effect on the size of the unit cell than the n parameter. When m is held constant, the change in unit cell size is much less significant compared to when n is held constant, where an increase in m results in a drastic increase in unit cell size.

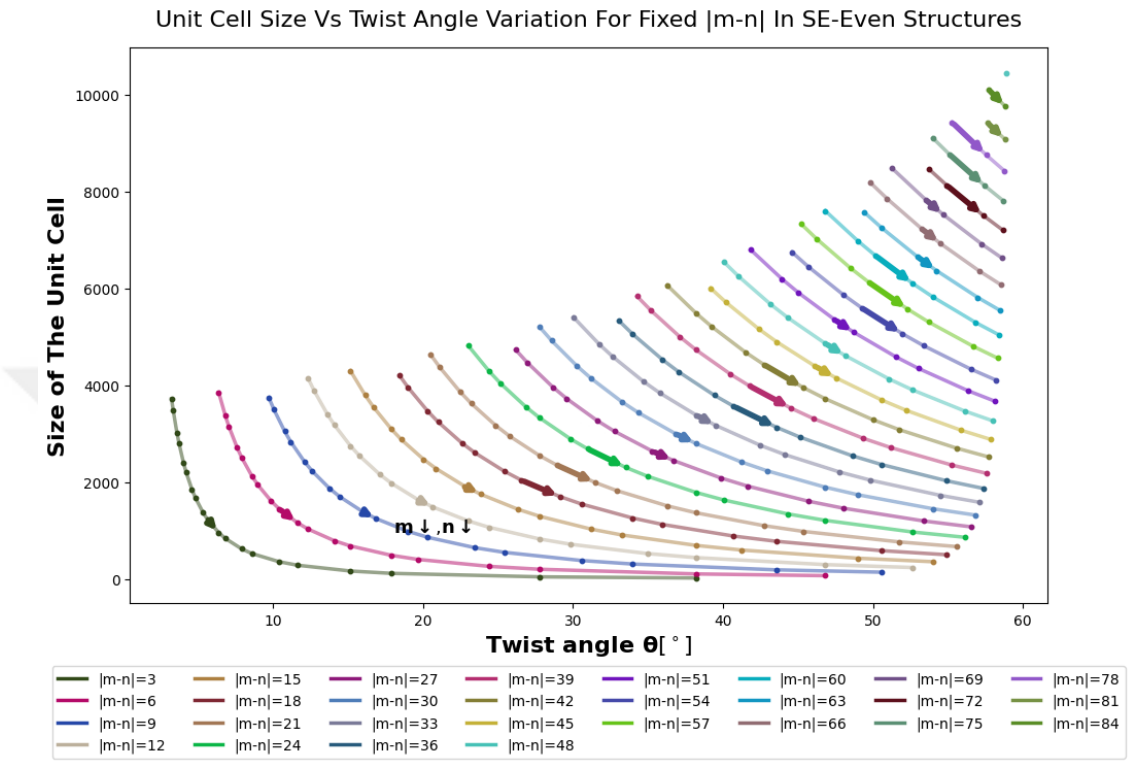

Figure 2.16: Patterns observed when the $|m-n|$ value is held constant in the graph showing the relationship between the unit cell size of TBG and the twist angle for SE even structures. The corresponding $|m-n|$ values are indicated in the legend.

As with the SE odd TBG, we examined the pattern followed by the scatter points when $|m-n|$ is constant, as shown in Figure 2.16. The arrows in the figure indicate the direction in which m and n values decrease. A behavior similar to that observed in Figure 2.11 is evident. The unit cell size also decreases with the reduction in m and n values for each constant $|m-n|$ value. From this figure and Figure 2.11, we conclude that when $|m-n|$ is held constant, the change in unit cell size is more significant at small angles.

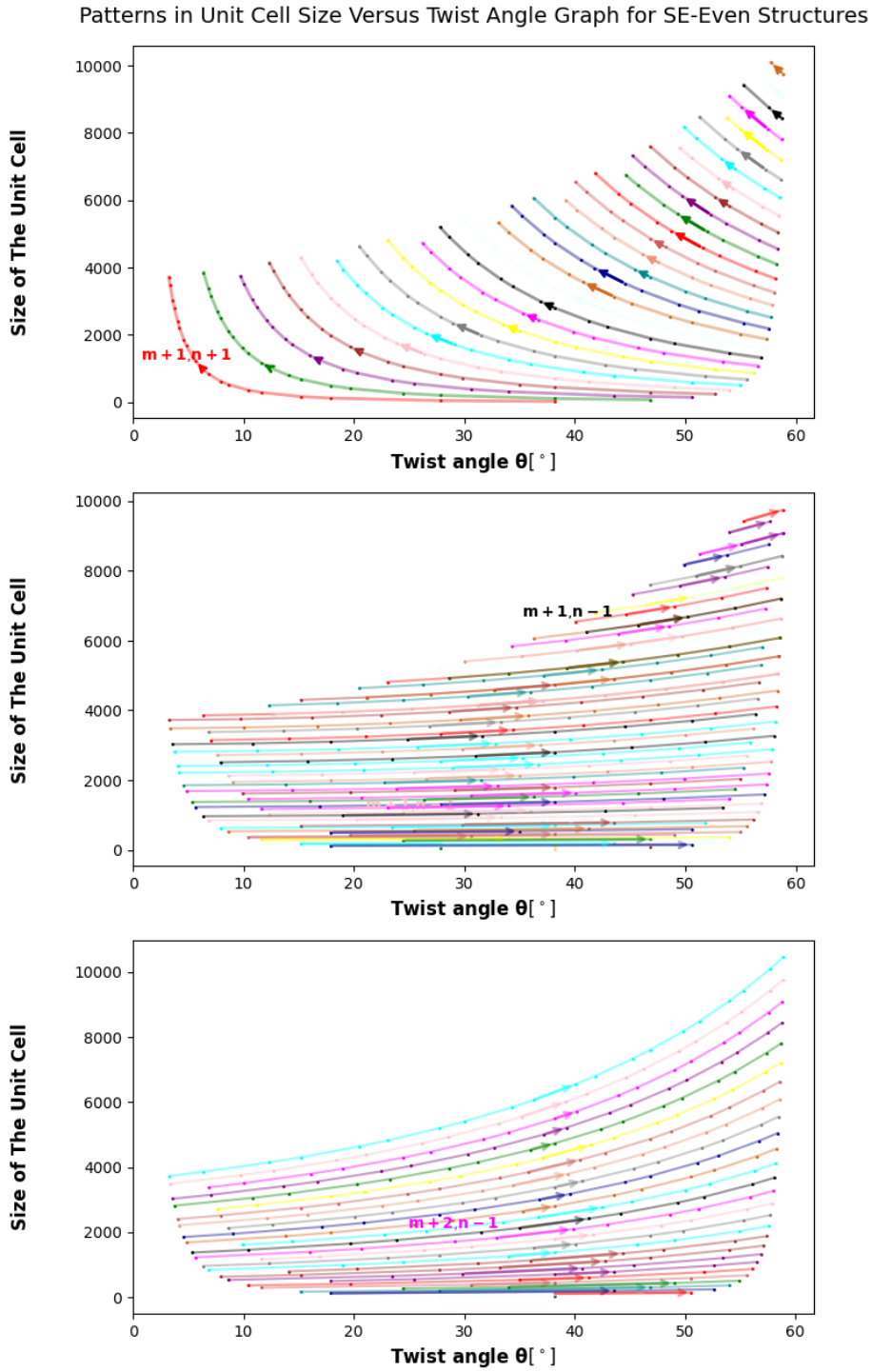

Figure 2.17: Impact of (m, n) variations on twist angle and unit cell size in SE even structures, with (m, n) pairs following the increments of (a) $(1, 1)$; (b) $(1, -1)$; (c) $(2, -1)$.

For even structures, we examined the same variations applied to odd structures in Figure 2.12, with the resulting patterns plotted in Figure 2.17. In Figure 2.17(a), the (m, n) pairs follow an increment of $(1, 1)$ at each step. These patterns exhibit the same convergence behavior shown in Figure 2.12(a). We also explored the impact of changing the (m, n) pairs by $(1, -1)$ and we plotted it in Figure 2.17(b), which demonstrated similar behavior to that observed for odd structures. Specifically, the increase in twist angle has a minimal impact on the change in unit cell size when following this pattern. Hence, the averaging effect is also evident in these observations. In Figure 17(c), the patterns formed by incrementing m by 2 and decrementing n by 1 are observed. Here, the magnitude of the size increase is significant. Generally, we observed that the patterns in these plots are similar for both even and odd structures. Figures 2.12 and 2.17 demonstrate that when both parameters change in the same direction, the size of the unit cell undergoes drastic changes. Conversely, when one parameter increases while the other decreases, an averaging effect moderates this pronounced variation, influenced by the magnitude of the relative variations. Additionally, it is important to note that other distinct patterns emerging from various increments can be identified within the dataset.

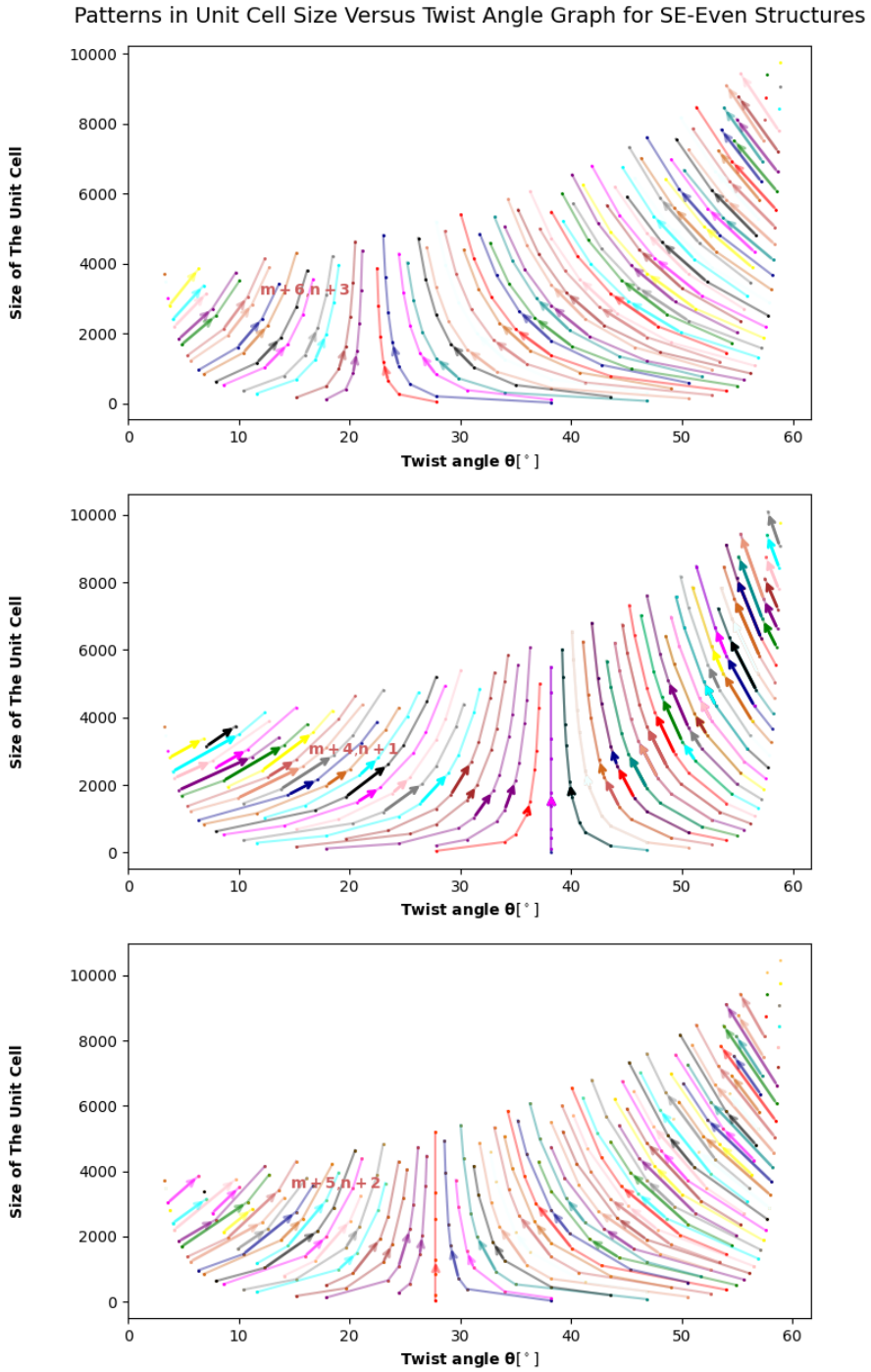

Figure 2.18: Influence of (m, n) variations on twist angle and unit cell size in SE even structures when (m, n) follows (a) an increment of $(6, 3)$. (b) an increment of $(4, 1)$. (c) an increment of $(5, 2)$. Lines are seen to converge towards specific angles.

In Figure 2.18, we present three graphs that highlight the variations in both unit cell size and twist angle as m and n increase by distinct values for structures with SE-even symmetry. In Figure 2.18(a), as m increases by 6 and n increases by 3, the pattern lines converge towards an angle of 21.787°. The behavior observed here is similar to that in Figure 2.13, although the magnitude of the increment differs. This is because, in even structures, $|m - n|$ values are multiples of 3; thus, the increment by $(2, 1)$ cannot be observed. Figure 2.18(b) demonstrates the convergence of lines towards an angle of 38.213° as m increases by 4 and n increases by 1. Finally, in Figure 2.18(c), we observe the patterns followed by an increment of $(5, 2)$, with the patterns converging towards an angle of 27.796°. Comparing Figure 2.18 to Figure 2.13(c), we observe that the patterns in each appear symmetric to one another. This symmetry is also evident when comparing Figures 2.18(a) and 2.13(b), as well as Figures 2.18(b) and 2.13(a). To better visualize this, we plotted the patterns from Figures 2.18(c) and 2.13(c) within the same graph, as shown in Figure 2.19(b). This confirmed the observed symmetry. Recall that $(3, 1)$ and $(5, 2)$ are commensuration partners. These observations confirm that the increments in odd structures result in patterns symmetric to those formed by the respective increments of their commensuration partners. Additionally, we combined Figures 2.13(b) and 2.18(b) into a single graph, as shown in Figure 2.19(a). This comparison illustrates the patterns resulting from similar increments in both even and odd structures. Despite their similar behaviors, the patterns do not align perfectly, due to the relationship $N_{\text{even}} = \frac{N_{\text{odd}}}{3}$.

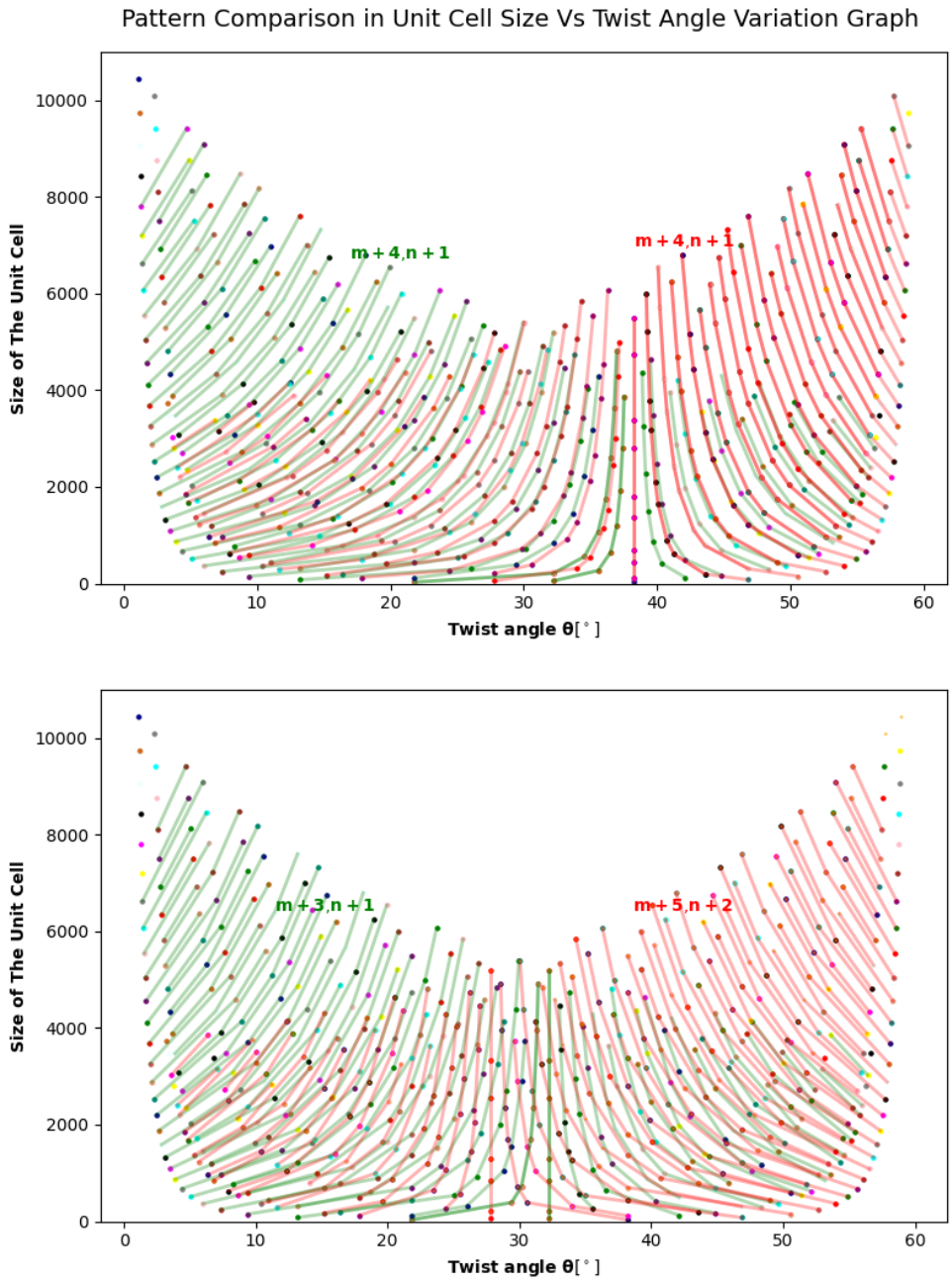

Figure 2.19: Comparison of SE-even and SE-odd TBG structures. (a) Combines data from Figure 2.13(a) and Figure 2.18(b), with green curves representing the odd structure and red lines representing the even structure. (b) Combines data from Figure 2.13(c) and Figure 2.18(c), with the same color scheme: green for the odd structure and red for the even structure.

Based on our previous observations, we can identify a specific relationship between the lattice parameters of even structures and their commensurate partners. This relationship is given by the equation:

$$\begin{pmatrix} \bar{n} \\ \bar{m} \end{pmatrix} = \begin{pmatrix} -1 & 1 \\ 2 & 1 \end{pmatrix} \begin{pmatrix} \mathrm{n} \\ m \end{pmatrix} \tag{2.12}$$

where $(\bar{m}, \bar{n})$ represent the lattice parameters of the even structure and (m, n) correspond to their commensurate partner.[6] Through this comprehensive analysis, we have highlighted several conclusions and rules that help elucidate the relationship between the lattice parameters and the variation of unit cell size versus twist angle. These can be summarized as follows:

- The lattice parameters of SE-even structures have a specific relationship with those of their odd commensuration partners, as demonstrated in the matrix in Equation 2.12.
- For both SE-even and SE-odd structures, the patterns observed in the figures are generally similar, with the most noticeable difference being in the sizes.
- The lattice parameter m has a greater impact on the unit cell size than the parameter n, while n has a larger effect on the corresponding twist angle. This relationship can be utilized to optimize the selection of lattice parameters.
- When the (m, n) pair follows a specific increment, the resulting pattern indicates that when both parameters increase, the effect on the unit cell size is substantial. Conversely, when one parameter decreases, there is an averaging effect that minimizes variation in unit cell size. The greater the increase in one parameter relative to the decrease in the other, the larger the variation in unit cell size observed in the patterns.
- Figures 2.13 and 2.18 reveal a distinct convergence of patterns associated with specific (m, n) increments, such as (x, y), toward the angle corresponding to TBG structures with lattice parameters following the relation $m = \frac{x}{y}n$.

- The convergence and pattern lines observed for certain increments, such as (m, n) for odd structures, are symmetric to those corresponding to increments of $(\bar{m}, \bar{n})$ for even structures.

Utilizing these insights, we can determine the optimal set of lattice parameters (m, n) for studying a specific range of angles while minimizing the unit cell size, which eases computational challenges. This approach helps us avoid extensive calculations to find the most suitable structures.

Moving forward, the next chapter will focus on calculating the interlayer energies of twisted bilayer graphene using empirical potentials. The geometrical properties of TBG established in this chapter will provide a crucial foundation for investigating its energy profiles.

Chapter 3

Structural and Energetic Analysis of Twisted Bilayer Graphene

3.1 Interlayer Energies in Twisted Bilayer Graphene: Lennard-Jones Potential

Despite significant advancements in understanding the electronic properties of graphene, there remain unresolved questions regarding the interlayer potentials and bonding energies in twisted bilayer graphene. The van der Waals force is a distance-dependent interaction between atoms or molecules that is responsible for the binding between separate layers of graphene. Two distinct approaches are used to describe van der Waals potentials for graphene: The first-principles approach that involves solving the Schrödinger equation, and the other approach based on the use of empirical potentials.[8] While the first-principles approach is the most accurate one, it is computationally expensive and limited to studying small systems with a limited number of atoms. On the other hand, empirical interatomic potentials are computationally efficient and easier to apply, making

them suitable for larger systems.[9]

Among these potentials, the Lennard-Jones potential is the most used potential for finding the binding energy between layers of graphene. It's primarily favored due to its simplicity in application, as it depends only on the interatomic distance. This potential successfully predicts the equilibrium layer spacing and the c-axis elastic modulus of graphite in close agreement with experimental values.[10] In our study, to investigate the influence of twist angle on the binding energy of twisted bilayer graphene, we fixed the interlayer distance to be $d_0 = 3.35$Å and we ignored the corrugation induced at small angles.

The Lennard-Jones potential is defined by the following expression:

$$V_{ij}(\mathbf{r_{ij}}) = 4\epsilon \left[\left(\frac{\sigma}{\mathbf{r_{ij}}} \right)^{12} - \left(\frac{\sigma}{\mathbf{r_{ij}}} \right)^{6} \right] \tag{3.1}$$

Here, $\mathbf{r_{ij}}$ represents the distance between atoms i and j while ϵ and σ serve as constants. By setting ϵ to $2.168\, meV$ and σ to 3.36 Å, the inter-layer distance in graphite, which is 3.35 Å, can be accurately reproduced.[10] It is worth noting that the intralayer energy of each individual layer remains unaffected by any changes in the twist angle. Therefore, the difference between the energies of various structures comes primarily from the interlayer energy term. In our subsequent calculations, our focus will solely be on determining the interlayer energy for different graphene structures. The van der Waals (vdW) energy between the two graphene layers is computed by summing the interaction energy between atoms in different layers, as expressed by the following equation:[11]

$$V_{\text{vdW}} = \sum_i \sum_j V_{ij} \tag{3.2}$$

Here, the index i refers to atoms in the bottom layer, while the index j refers to atoms in the top layer. The term V_{ij} represents the Lennard-Jones potential derived from Equation 3.1. To determine the interlayer energy per atom for a specific twisted bilayer graphene system, the obtained total interlayer energy is divided by the number of atoms in the unit cell, then it's divided by two. This division accurately distributes the pair energy contribution to each individual atom. [12] By employing Equation 3.1, we first find the interlayer

energy for both AA and AB stacked bilayer graphene structures. Through this implementation, we determine that the interlayer energy of AA stacked bilayer graphene amounts to $-17.363\,meV$, while the interlayer energy of AB stacked bilayer graphene is calculated to be $-17.7245\,meV$. Notably, we observe that the interlayer energy of the AB configuration is the lowest, ultimately indicating the stability of AB stacked bilayer graphene as the preferred structure for graphene. Using the same approach, we aim to determine the interlayer energy based on Lennard-Jones (LJ) potential for twisted bilayer graphene structures with various twist angles. In this study, we take the two layers of graphene to be infinitely large and initially arranged in the AA stacking configuration before being rotated by the corresponding twist angle.

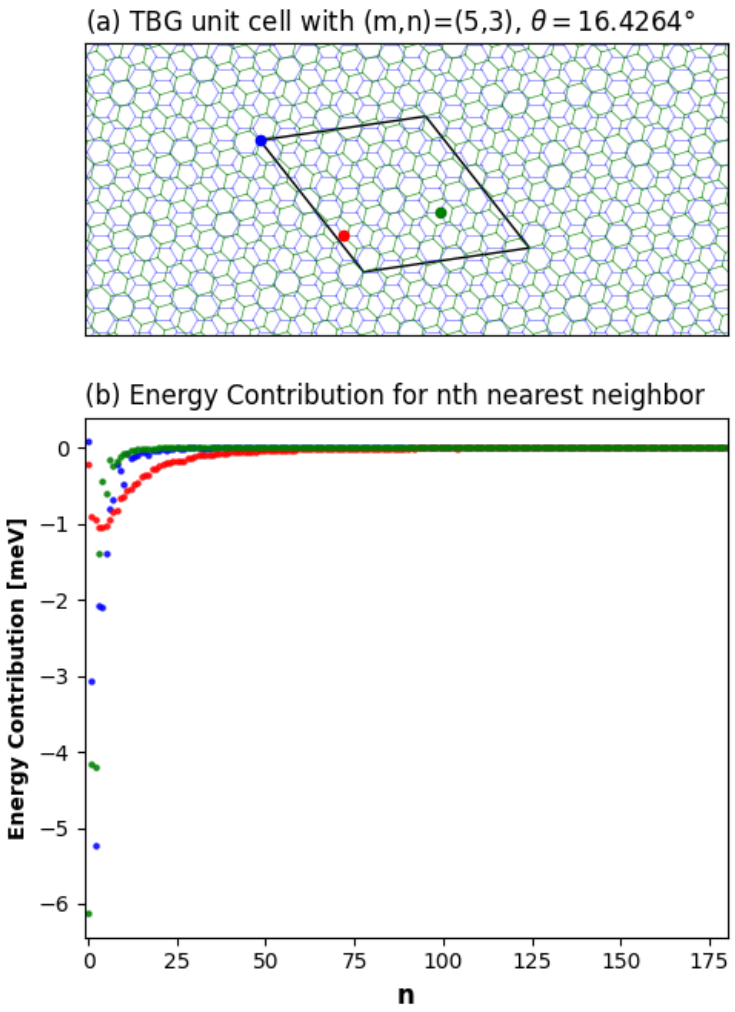

Figure 3.1: (a) Demonstration of the unit cell of TBG with $(m, n) = (5, 3)$ and $\theta = 16.426°$; (b) Energy contributions from the nth nearest neighbors to the total interlayer energy of specific atoms from the structure, with each color corresponding to the atoms highlighted in (a).

In the case of the TBG structure with the given parameters $(m, n) = (5, 3)$ and $\theta = 16.426°$, we plotted in Figure 3.1. the energy contributions from the n-th nearest neighbors to the total interlayer energy of three specific atoms highlighted in Figure 3.1, versus n, the index number of the nearest neighbor. A noteworthy

observation concluded from this plot is that as the value of n increases, representing an increasing distance between the i and j atoms, the corresponding contribution to the total energy gradually decreases until it becomes negligible at a certain distance. This specific distance is referred to as the cut-off distance.

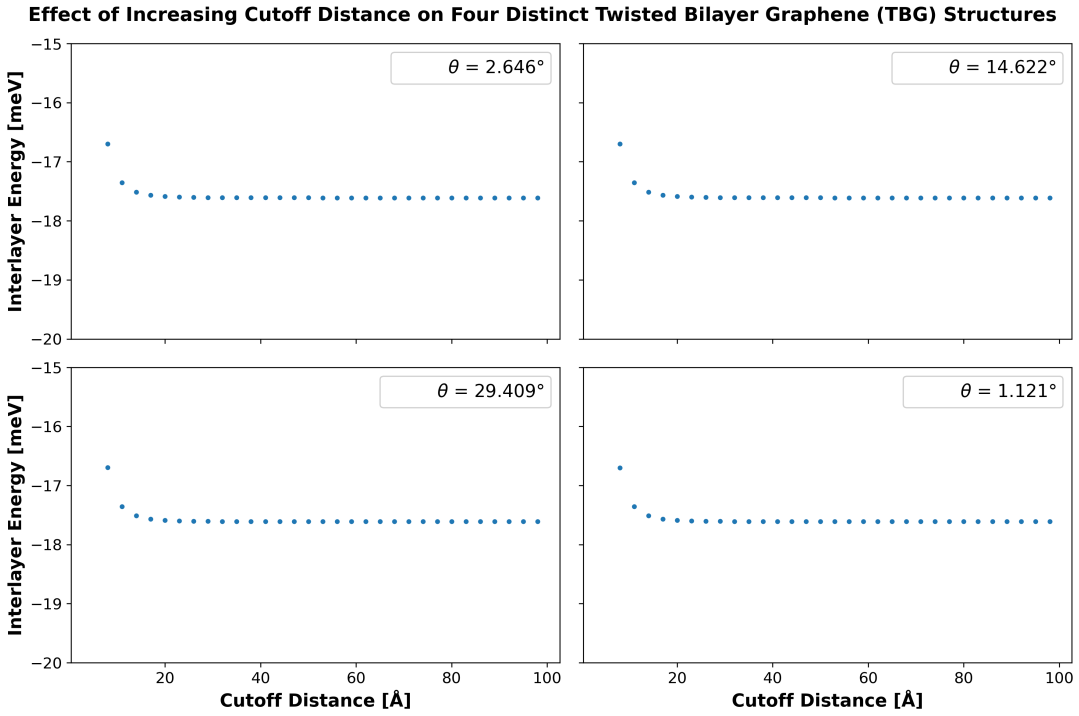

Figure 3.2: Variation of interlayer energy with the increase of cutoff distance for four different TBG structures: (a) $\theta = 2.6459°$, (b) $\theta = 14.6222°$, (c) $\theta = 29.4093°$, and (d) $\theta = 1.1213°$.

To accurately determine the appropriate cutoff distance that can be used in our calculations, we examined four distinct twisted bilayer graphene (TBG) structures with varying angles, as depicted in Figure 3.2. For each of these structures, we calculated the interlayer energy as the cutoff distance increased systematically from 5 to 100Å. It is worth noting that as the cutoff distance increases, the interlayer energy becomes more precise; Nevertheless, beyond a certain distance, the change in energy becomes negligible, as previously mentioned and illustrated in Figure 3.2. Based on these findings, we were able to identify the optimal cutoff distance for all the presented structures, determined to be 60Å. Thus,

this value will be employed in our subsequent calculations. It's noteworthy that the energy E(θ), as the size of the unit cell, is an even and periodic function, where E(θ) = E(-θ) and E(θ + 120) = E(θ).[13] With this in mind, we focus our analysis on TBG structures with twist angles between 0° and 60°, plotting only the corresponding energies. We hence computed the interlayer energies for different twisted bilayer graphene structures by varying the (m, n) parameters within the range of 1 to 30, starting from an initially AA-stacked bilayer graphene configuration. Subsequently, we plotted these interlayer energies as a function of the twist angle, denoted by θ. This plot can be observed in Figure 3.3.

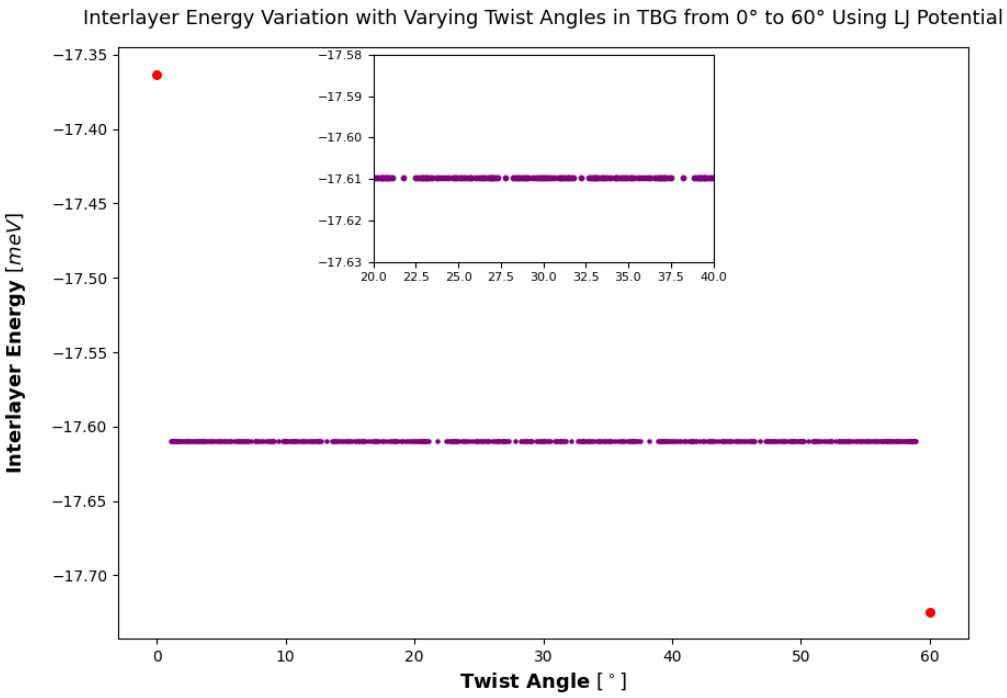

Figure 3.3: Interlayer energy variation of TBG with twist angle ranging from 0° to 60°, calculated using the Lennard-Jones potential. The red scatter points specifically correspond to AA stacked bilayer graphene at $\theta = 0°$ and to AB stacked bilayer graphene at $\theta = 60°$. Inset shows A detailed view of the interlayer energy variation around $\theta = 30°$.

Based on the observations made in Figure 3.3, the interlayer energy was found

to be almost constant at $-17.61\,meV/atom$. This value remains constant even as the twist angle, θ, approaches both $0°$ and $60°$. Notably, at $\theta = 0°$, the energy abruptly transitions to the value of interlayer energy for AA stacked bilayer graphene, $-17.363\,meV$. Similarly, at $\theta = 60°$, the energy abruptly transitions to $-17.7245\,meV$, corresponding to the interlayer energy for AB-stacked bilayer graphene. Nonetheless, we found that the interlayer energy values obtained from our calculation did not align with either first principle calculations or experimental results.[12] This discrepancy comes from the fact that the Lennard-Jones potential used in our computations was only dependent on the interatomic distances between pairs of atoms, this property made it easier to apply but less accurate. To correct this drawback, we substituted the Lennard-Jones potential employed in our computations with the Kolmogorov-Crespi potential introduced in Ref. [14]

3.2 Interlayer Energies in Twisted Bilayer Graphene: Kolmogorov-Crespi Potential

In the previous section, we discussed the limitations of the LJ potential in accurately calculating the interlayer energy for TBG and describing the energy changes during rotational displacements from the original AA configuration of bilayer graphene. These limitations arise from the neglect of short-range Pauli repulsion between overlapping π orbitals of adjacent layers.[8][9] In order to address this issue, Kolmogorov and Crespi (KC) developed a registry-dependent interlayer potential for graphitic structures. This modified potential incorporates the repulsive interactions involving overlapping orbitals, thus ensuring a more accurate representation of the energy changes resulting from transverse displacement.[14] The KC potential includes two terms, the dispersive van der Waals (vdW) attraction between layers, which is defined through the same $\mathbf{r}^{-6}$term employed in the LJ potential; and the repulsive interactions arising from orbital overlap are represented by a Morse-type exponential term, multiplied by configuration-dependent corrections related to the transverse distance between atom pairs. This

latter term is very short-ranged, diminishing to zero at two transverse interatomic distances.[15] The KC potential can be expressed as:

$$
\begin{aligned}
V(\mathbf{r}_{ij}, \mathbf{n}_i, \mathbf{n}_j) &= e^{-\lambda(\mathbf{r}_{ij}-z_0)}[C + f(\rho_{ij}) + f(\rho_{ji})] - A(\frac{\mathbf{r}_{ij}}{z_0})^{-6} \\
\rho_{ij}^2 &= \mathbf{r}_{ij}^2 - (\mathbf{n}_i \mathbf{r}_{ij})^2 \\
\rho_{ji}^2 &= \mathbf{r}_{ij}^2 - (\mathbf{n}_j \mathbf{r}_{ij})^2 \\
f(\rho) &= e^{-(\rho/\Delta)^2} \sum C_{2n} (\rho/\Delta)^{2n}
\end{aligned}
\tag{3.3}
$$

The vector $\mathbf{n}_k$ (where k = i or j) denotes the layer normal at atom k. ρ_{ij} represent the transverse distance between atoms i and j. These vectors are illustrated in Figure 3.4 for TBG structure with twist angle 16.426°. Note that the summation over n in Equation 3.3 is confined within the range of n = 0 to n = 2.

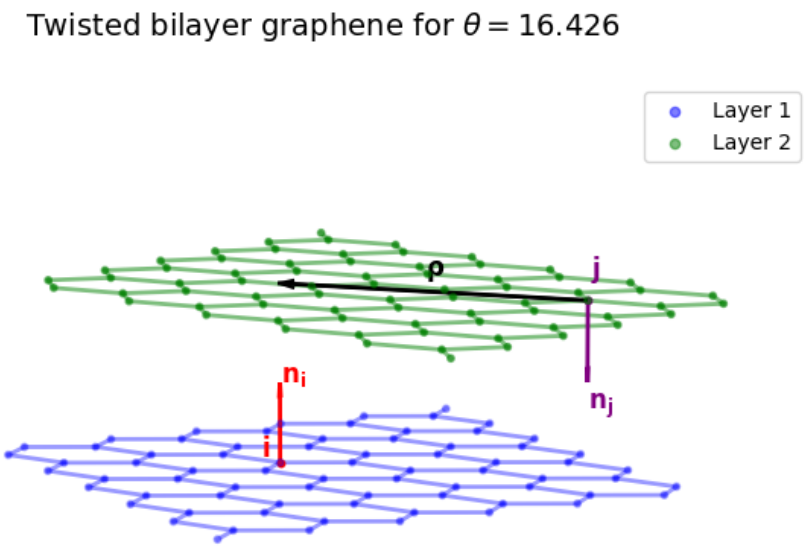

Figure 3.4: Illustration of transverse distance ρ and vectors $\mathbf{n_i}$ and $\mathbf{n_j}$ in a TBG structure with twist angle $\theta = 16.426°$.

While calculating the interlayer energy using the KC potential for TBG, the impact of corrugation was disregarded. For carbon-carbon interactions in graphene bilayer, specific values are assigned to the parameters $C_0 = 15.71\,meV$, $C_2 = 12.29\,meV$, $C_4 = 4.933\,meV$, $C = 3.030\,meV$, $\Delta = 0.578\,\text{Å}$, $\lambda = 3.629\,\text{Å}^{-1}$,

$A = 10.238\,meV$, and $z_0 = 3.34\,\text{Å}$[14] Utilizing the same methodology, the same cutoff distance of 60 Å as the previous section of 60 Å is implemented. Utilizing the methodology employed earlier with the Lennard-Jones potential, we determine the interlayer energy of AA and AB stacked bilayer graphene using the KC potential. The interlayer energy of the AA stacked bilayer graphene is determined to be $-14.499\,meV$, and the interlayer energy of the AB stacked bilayer graphene is calculated to be $-21.795\,meV$. Subsequently, we apply the same procedures to evaluate the interlayer energies of twisted bilayer graphene structures, which correspond to twist angles ranging from 0° to 60°, implementing the KC potential from Equation 3.3. The corresponding energies are plotted against the varying twist angles and presented in Figure 3.5. In addition, the inset in Figure 3.5 offers a closer look into these energy patterns.

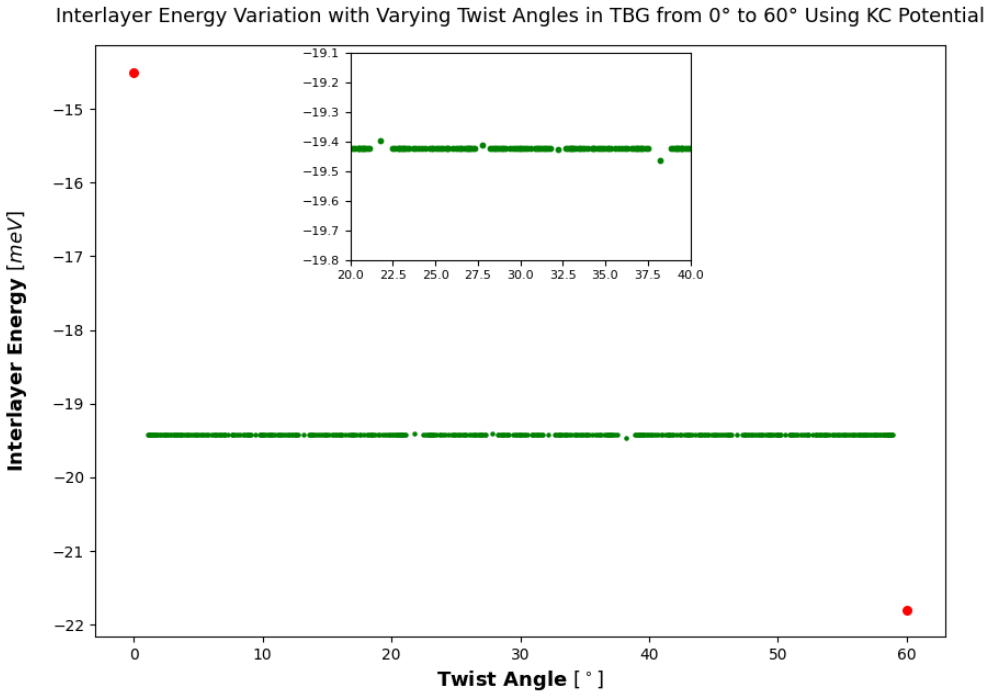

Figure 3.5: (a) Variation of interlayer energy with twist angle in TBG structures, spanning from 0° to 60°, calculated using the KC potential. The red points correspond to the energies of AA and AB bilayer graphene; Inset: Close-up view of the interlayer energy variation around 30°.

A noteworthy observation derived from this plot reveals a nearly constant energy value of $-19.42\,meV/atom$ for all twist angles. However, there are slight variations at specific angles: at 21.787°, where the energy drops slightly to $-19.399\,meV/atom$, and at 38.213°, it increases to $-19.465\,meV/atom$. These small changes highlight the subtle impact of layer alignment on the interlayer interactions in TBG. Additionally, the plot features discontinuous jumps at $\theta = 0°$ and $\theta = 60°$, which correspond to the energies of AA and AB stacked bilayer graphene, respectively. Based on these results, coupled with the findings presented in the previous section, it can be inferred that the interlayer energy within twisted bilayer graphene remains mostly unaffected by variations in the twist angle.

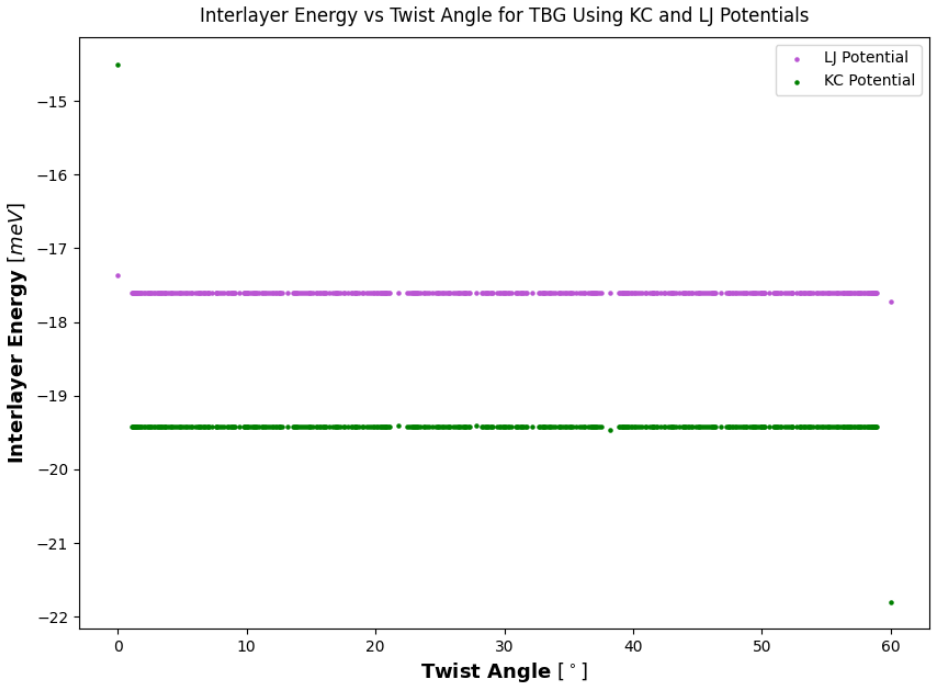

Figure 3.6: Comparison of interlayer energy variations with twist angle for TBG structures, ranging from 0° to 60°, calculated using different potentials: Lennard-Jones potential in purple dots, and KC potential in green dots.

In Figure 3.6, we present the energy plots of twisted bilayer structures obtained

by the implementation of both the LJ and KC potentials. The energies calculated using the LJ potential are depicted in purple, while those obtained using the KC potential are shown in green. Notably, it can be observed that the KC energies are consistently lower compared to the LJ energies, although the overall trends remain similar. The outcomes derived from the KC potential align well with predictions from first principles calculations and experimental data.[14] On the other hand, the LJ calculations prove to be inadequate in capturing this agreement, highlighting the limitations of the LJ potential in accurately capturing the energetics of twisted bilayer graphene.

3.3 Exploring Energy Invariance in Twisted Bilayer Graphene: An Analysis of Local Stackings

In the preceding subsections, we have analyzed the relationship between the energy variation of twisted bilayer graphene and the twist angle. Although these analyses produced differing numerical results, they consistently demonstrated minimal variation in energy when the bilayer graphene is rotated, resulting in nearly flat plot lines depicted in Figure 3.6. To understand the underlying cause of this energy invariance, we conducted an in-depth examination of TBG's structure, uncovering distinctive characteristics and identifying patterns that enhance our understanding of its energetic properties.

In Figure 3.7, we present four TBG structures, each characterized by a distinct twist angle. Here, we plotted the four structures with the following parameters: $(m, n) = (15, 13)$ rotated by $4.723°$, $(4, 3)$ rotated by $9.43°$, $(24, 13)$ rotated by $19.479°$, and $(13, 5)$ rotated by $28.78°$. Notably, a distinct observation emerges from the comparison of the four subplots illustrated in Figure 3.8. The TBG configurations with smaller angles exhibit a Moiré pattern, while TBG structures with higher twist angles do not display such a pattern. Based on this finding, it can be concluded that the observation of a Moiré pattern depend on the value of

the twisting angle in TBG structures.

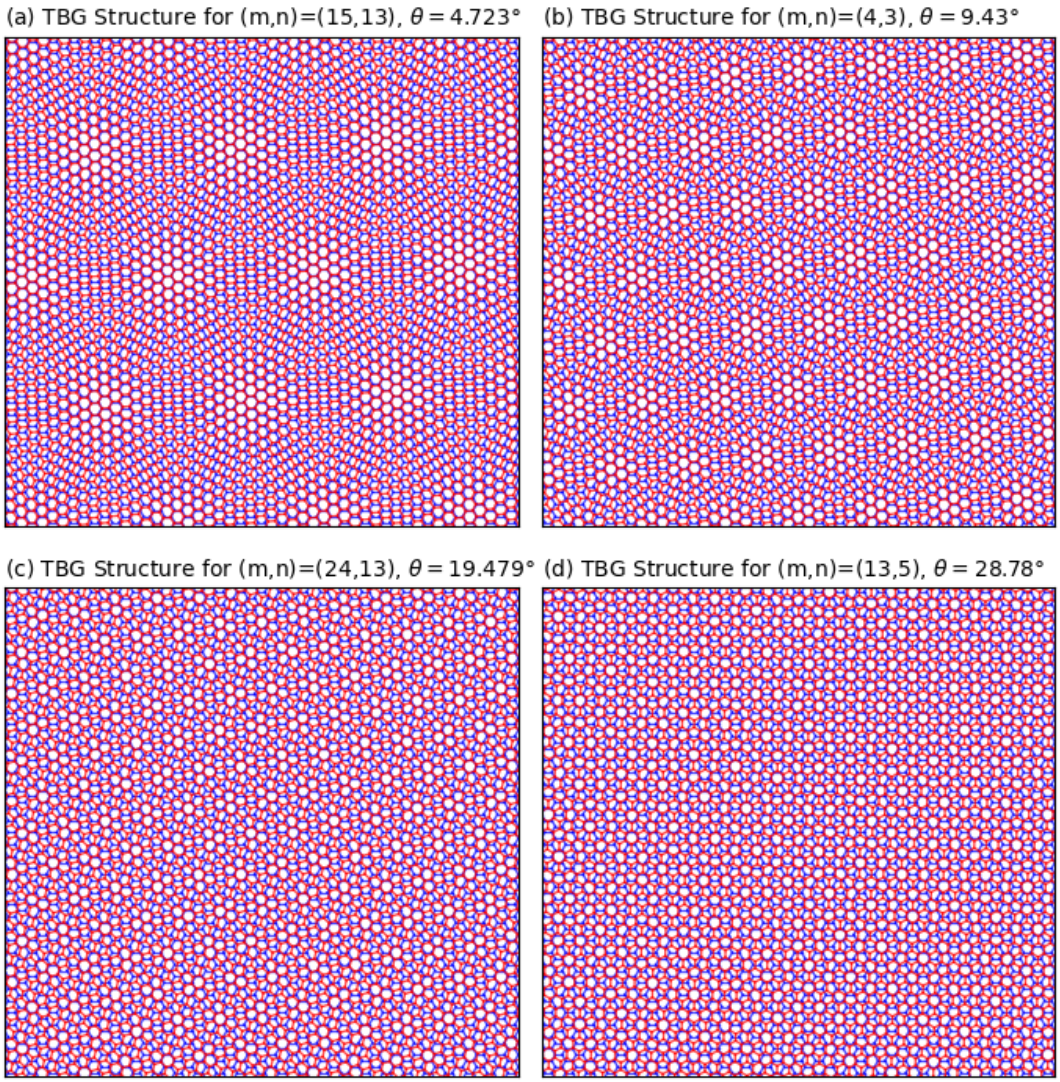

Figure 3.7: Four TBG structures characterized by distinct twist angles. (a) (m, n) $= (15, 13)$ at $4.723°$, (b) $(m, n) = (4, 3)$ at $9.43°$, (c) $(m, n) = (24, 13)$ at $19.479°$, and (d) $(m, n) = (13, 5)$ at $28.78°$.

In Moiré pattern, we observe distinct bright and dark stacking regions: the bright region is called an AA stacking region, where the atoms from both layers nearly align atop each other. The displacement of atoms from the AA stacking

configuration is minimal, resulting in a visually empty and brighter area compared to the surrounding pattern. On the other hand, the dark regions correspond to AB and BA local stacking. In AB regions, an atom is positioned directly on top of a hexagon center, and the atoms in its surroundings exhibit a stacking similar to AB stacking. The BA stacking configuration is different than AB stacking only in the order of the layered atoms.[16] From our observations, we have found that Moiré pattern is only observable in the TBG structures with small twist angles θ, and at the angles $60^\circ - \theta$, corresponding to their commensuration partners. Beyond a certain angle, this pattern is not observable, and the TBG structure becomes turbostratic. To determine this critical angle, we need to consider that this pattern is only depicted when an AA stacking region is present. In our analysis, we denote the linear dimension of the critical angle θ_c as l_0.[17] The visualization of l_0 is present in Figure 3.8(b)

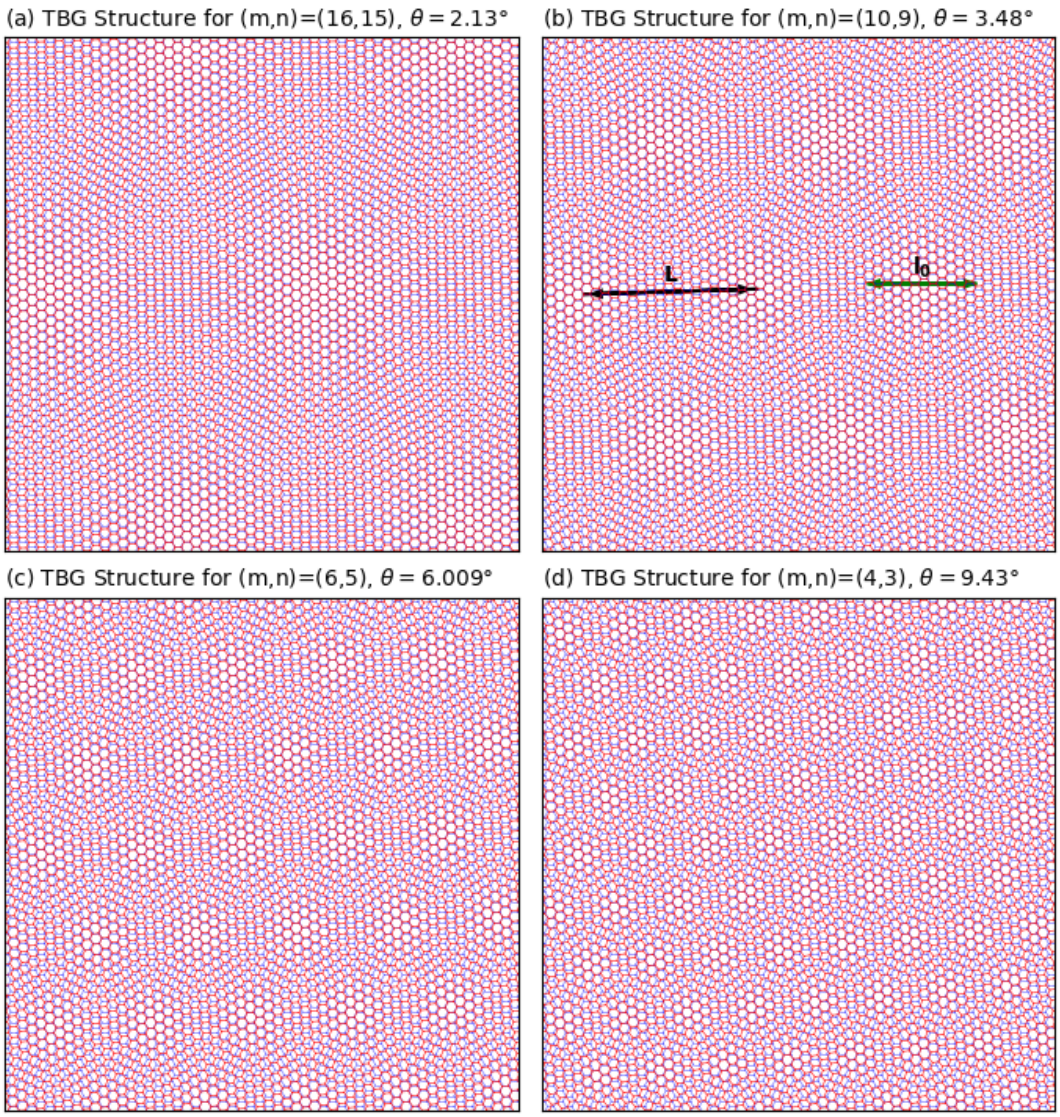

Figure 3.8: Examination of twisted bilayer graphene configurations with small twist angles to analyze the Moiré pattern characteristics. (a) $(m, n) = (16, 15)$ at 2.13°; (b) $(m, n) = (10, 9)$ at 3.48°, illustrating the linear dimension l_0 and Moiré period L; (c) $(m, n) = (6, 5)$ at 6.009°; and (d) $(m, n) = (4, 3)$ at 9.43°.

From our previous knowledge, AA stacking transitions to AB stacking when the atoms are shifted by $a_0\hat{i}$. Utilizing this information, we conclude that the AA stacking region is observed when the rotational shift of the linear dimension $l_0\theta_c$ is smaller than a_0, and it disappears when this shift exceeds this value, at which

point the AA stacking interferes with the AB stacked region. Hence, the local stacking regions are observable when the value of l_0 is significant, where:

$$l_0 = \frac{a}{\theta_c} \tag{3.4}$$

Another important parameter is the Moiré period introduced in Equation 2.7, which represents the distance between two neighboring AA stacking regions. This parameter is also illustrated in Figure 3.8(b). The patterns illustrated satisfy the condition of $|m-n|$=1 in odd structures and satisfy Equation 2.8. In Figure 3.8, we illustrate various twisted bilayer graphene configurations with small angles in order to examine the characteristics of the Moiré pattern. From these figures, it can be concluded that the Moiré period decreases as the twist angle increases, resulting in a gradual decrease in the distance between stacking regions until reaching the critical angle. Using Equation 3.4, we identified the AA stacking regions for a twisted bilayer graphene with a wide range of angles. We determined that when the twist angle θ exceeds 14°, the number of atoms within these regions becomes significantly reduced, and these regions become indistinguishable. When the twist angle approaches 0°, the Moiré period becomes larger. Moreover, our observations reveal that the size of the AA and AB stacking regions decreases as the twist angle increases, with these regions being particularly pronounced at angles close to 0°. Consequently, in TBG structures with nearly 0° twist angle, fewer AA regions are observed, but they account for a larger proportion of the overall stacking in the graphene structure.

Figure 3.9 presents a graph depicting the distribution of AA and AB stacked atoms relative to the rest of the atoms within the unit cell for TBG structures across various twist angles.

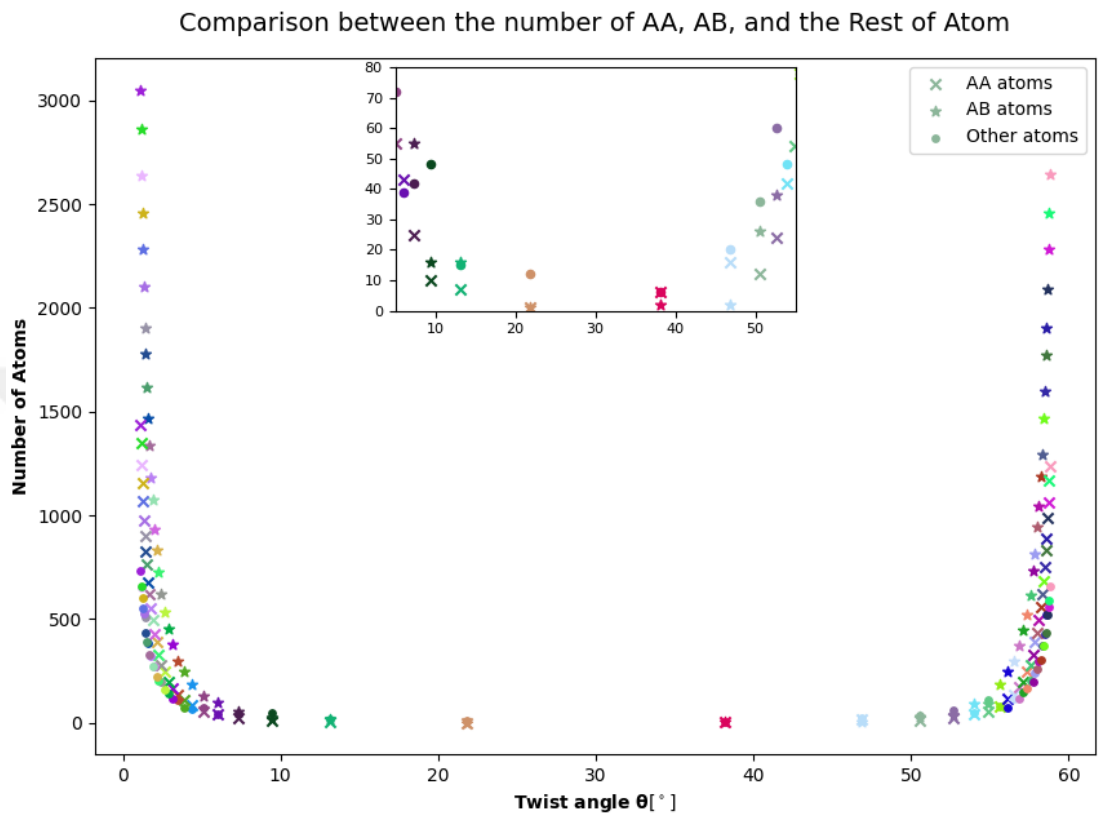

Figure 3.9: (a) The graph illustrates the distribution of atoms belonging to AA and AB regions, alongside the rest of atoms who don't belong to either atomic configurations, within the unit cell of a twisted bilayer graphene structure at angle θ. Inset provides a close-up view of TBG structures with small unit cells. The local stackings here were identified using a threshold distance of $\delta = 0.7$.

In 3.9, we observe that starting from $\theta = 13.17°$, the number of atoms not belonging to either the AA or AB stacking configurations first surpasses the number of AA atoms, followed by AB atoms. An exception occurs at $\theta = 9.43°$, where the quantity of non-AA and non-AB atoms exceeds both AA and AB atoms. It is important to note that at small angles, the two layers are corrugated. The interlayer distance experiences periodic variation dependent on the specific stacking configuration. In the AA stacking region, the interlayer distance exhibits an increase, resulting in the highest separation distance. Meanwhile, the AB stacking regions have the shortest interlayer distance. When the twist angle of

the TBG is larger than θ_c, the corrugation is absent.[17]

After observing the characteristics of Moiré pattern that appears at small angles, to better understand the underlying cause of the energy invariance, we now investigate the energetics of these local stacking regions. Employing the Kolmogorov-Crespi (KC) potential, which yielded more accurate results in our calculations, we aim to uncover the underlying reasons for the observed energy invariance.

From the Moiré patterns observed in Figure 3.7, we can identify the AA, AB, and SP (Saddle Point) stacking configurations, the latest occurring in the area between the AA and AB stacking regions.[18] To accurately identify the AA-stacked atoms, we adopted a method proposed in [16] which involves calculating the transverse distance between each atom in the bottom layer of the unit cell and its nearest neighbor in the top layer. Consequently, the atoms are classified into two distinct groups: *a atoms*, which have a nearest neighbor within a specified threshold distance δ, and *b atoms*, which do not. We identify the AA-stacked regions within the bottom layer by selecting *a atoms* whose three in-plane neighbors are also classified as *a atoms*. This method enables us to determine the atoms that are sufficiently close to each other to form an AA-like stacking configuration. Subsequently, we determined the area of the circle encompassing the AA-stacked atoms, defining its radius as r. In the odd structure of twisted bilayer graphene, these regions are located at the corners of the unit cell, around the points where two atoms from opposing layers coincide. In contrast, for even-structured TBG, this area is centered around the point where the centers of two hexagons align, at a position approximately equivalent to $S_3/3$. These observations are illustrated in Figure 3.10, where the AA-stacked atoms of the bottom layers are highlighted in purple. Drawing from the insights provided in [11] and our observations, we establish the relationship between the areas of the different stacking regions in odd structured TBG: the area of the SP region is $\frac{3}{2}$ times the area of the AB region, which in turn is 3 times the area of the AA region. These regions are plotted for both odd and even structures in Figure 3.10. In our structures, we observe AB and BA regions within each unit cell. In odd structures, these regions

are located within the unit cell, whereas in even structures, one of them is positioned near the corners. The SP region is identified, as mentioned, as the area between the AA and AB stacking regions. The SP-stacked atoms of the bottom layer are depicted in green. Employing this methodology, we have successfully identified the AA, AB, and SP atoms within both the even and odd structures of twisted bilayer graphene. The remaining atoms in the unit cell, are referred to as "U" (unclassified) atoms for the purpose of this analysis. The subsequent step of our investigation will involve the computation of the energies for these local stackings for various TBG structures. Using the KC potential, we computed these energies across a range of twist angles from 0° to 60°. The total energy of the system is the summation of these local stacking energies, with the energies corresponding to U (unclassified) atoms. The resulting data are visualized in the graph presented in Figure 3.11. From the figure, it is evident that the AA stackings have significantly higher energy values compared to all other configurations, while the AB-stacked regions exhibit the lowest energies. The SP-stacked regions have the second-lowest energies, and the U atoms' energies are the second highest. these specific stackings are not observed. Instead, the AA and AB regions are represented by single atoms where both layers align (AA) or where an atom in one layer aligns with the center of a hexagon in the opposing layer (AB). This alignment-dependent occurrence explains the variation in energy values observed within this angle range.

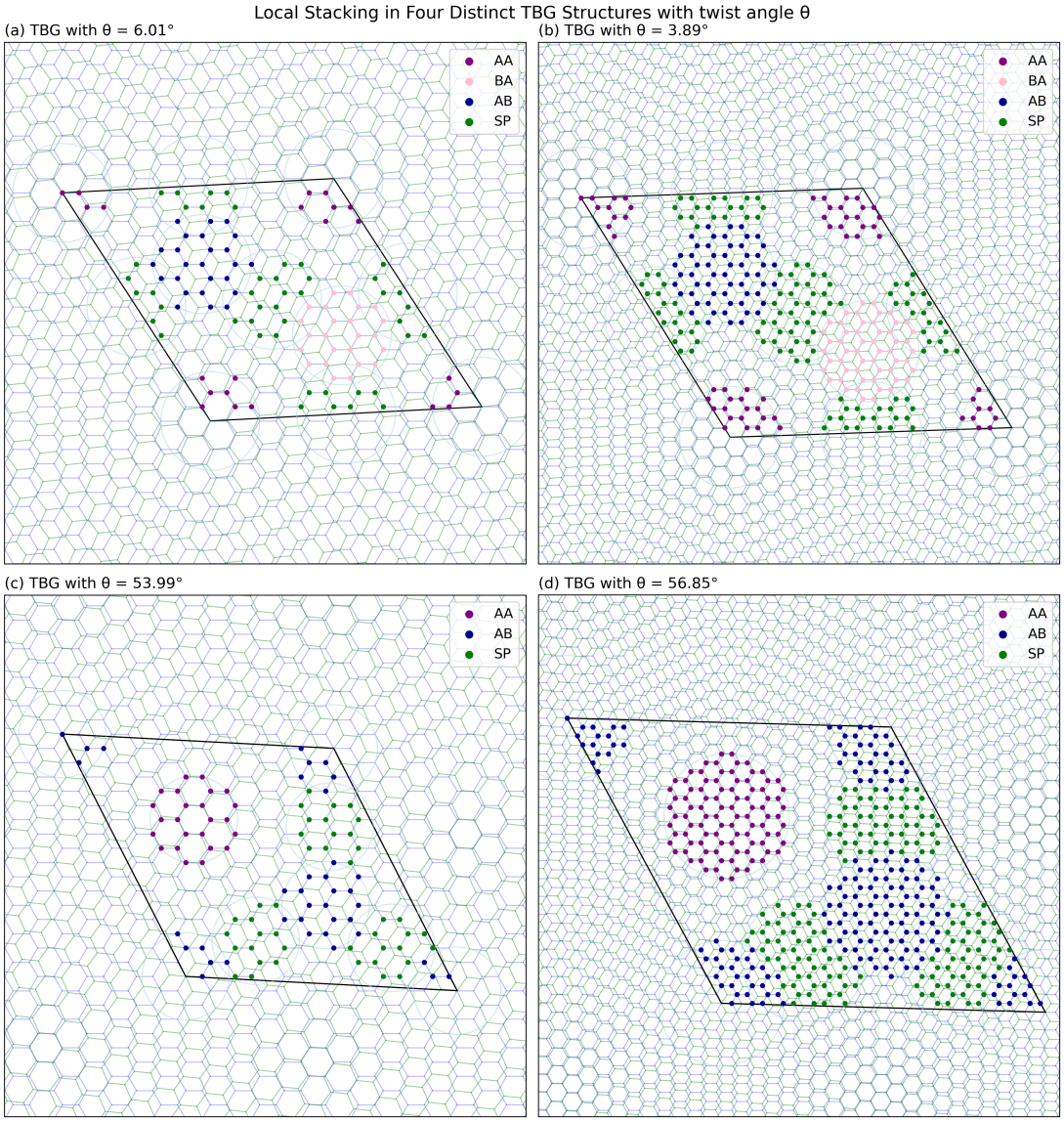

Figure 3.10: Local Stacking in Four Distinct TBG Structures with Twist Angle θ. The areas of AA, AB, BA, and SP stacking regions are plotted for both odd and even structures. The AA atoms are marked in purple, AB atoms in blue, BA atoms in pink, and SP atoms in green. The structures correspond to TBG structures with indices (a) $(m, n) = (6, 5)$ corresponding to twist angle $\theta = 6.01°$; (b) $(m, n) = (9, 8)$ corresponding to twist angle $\theta = 3.89°$; (c) $(m, n) = (16, 1)$ corresponding to twist angle $\theta = 53.99°$; and (d) $(m, n) = (31, 1)$ corresponding to twist angle $\theta = 56.85°$. The local stackings were identified using a threshold distance of $\delta = 0.55$.

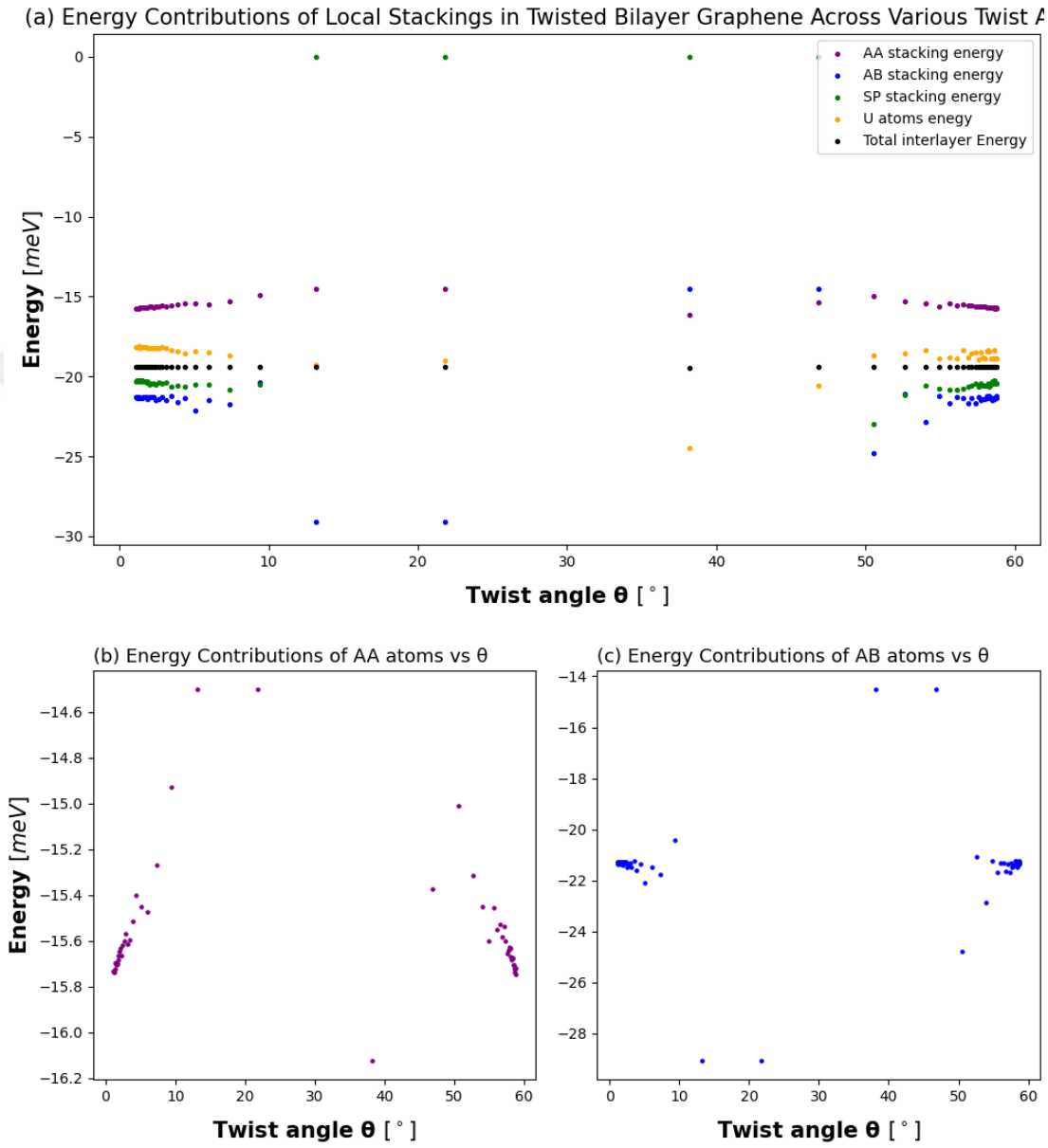

Figure 3.11: Energy contribution of (a) local stackings in twisted bilayer graphene across twist angles from 0° to 60°, calculated using KC Potential across twist angles 0° to 60°; (b) AA stacking region versus twist angle; (c) AB stacking region versus twist angle.

Before proceeding to analyze these observed variations, to gain a more precise understanding of the energy distribution and to visualize it more clearly, we separately computed the interlayer energy for all the atoms in the bottom layer of two

distinct twisted bilayer graphene structures characterized by (m, n) parameters of $(6, 5)$ and $(10, 9)$. This computation revealed a non-uniform distribution of energy levels among the atoms, with some exhibiting higher energies and others lower. These variations are illustrated in Figure 3.12, employing a color-coded scheme where atoms with higher energy levels are presented in yellow, and those with lower energy levels are depicted in purple. A notable observation from this visual representation is the distinct energy distribution patterns within different stacking regions. Specifically, the AA stacking regions, located at the corners of the unit cells in odd structures, consist predominantly of atoms with higher energies. In contrast, the AB and BA stacking regions comprise a mixture of both high-energy and low-energy atoms. The graphical representation suggests that the AA regions exhibit the highest interlayer energy levels among all observed configurations, as it was shown in Figure 3.11(a).

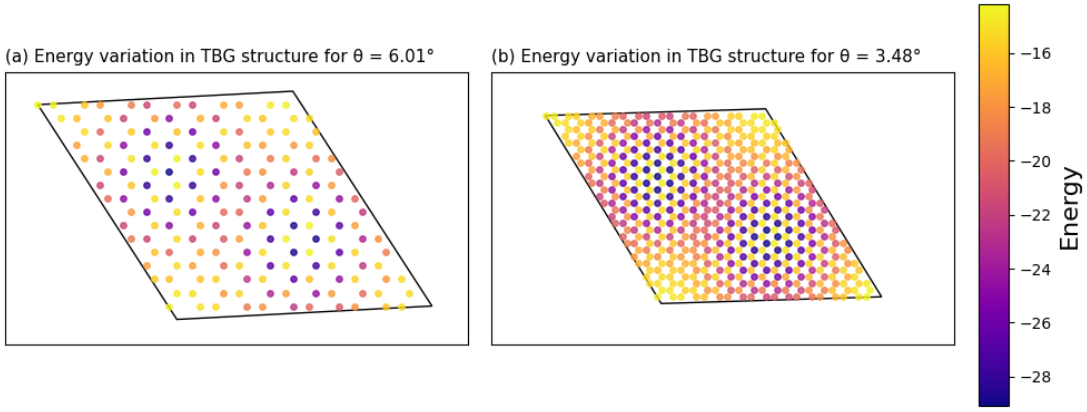

Figure 3.12: The interlayer energy distribution for atoms in the bottom layer of two twisted bilayer graphene structures, characterized by (m, n) parameters of (a) $(6, 5)$ with twist angle $\theta = 6.01°$ and (b) $(10, 9)$ with twist angle $\theta = 3.48°$. The prism on the right indicates the interlayer energy corresponding to each color, with the color gradient ranging from yellow (higher energy) to purple (lower energy).

In Figures 3.11(b) and 3.11(c), we notice some patterns: as the twist angle increases, the energy of AA-stacked atoms increases, whereas the energy of AB-stacked atoms decreases. Building on earlier observations from Figure 3.9, we

find that as the twist angle increases, the number of AA-stacked atoms decreases. Consequently, the area of the AA-stacked regions diminishes, becoming confined to atoms situated closer to the center of these regions. These central atoms possess higher energies relative to those positioned farther from the center, as illustrated in Figure 3.12. This effect influences the average energy value of AA-stacked atoms in these structures, elucidating the results presented in Figure 3.11. To gain deeper insights into the local stackings and their impact on the total energy of twisted bilayer graphene, we investigated the variation in the energy difference between AA and AB stackings as the twist angle increases from 0° to 60°. This analysis is illustrated in Figure 3.13(a), which depicts the evolution of Δ, defined as the difference between the AA and AB stacking energies ($\Delta = E_{AA} - E_{AB}$). It is important to note that in the angle range of 10° to 50°, these local stackings are not discernible, and consequently, data points for this interval have been omitted. From the plot, we observe that as the twist angle θ increases from 0° to 10°, and symmetrically decreases from 60° to $60^\circ - \theta$, the difference between the AA and AB stacking energies increases non-linearly. This behavior can be attributed to the significant rise in AA stacking energies when their corresponding areas are reduced as the twist angle increases. In contrast, AB stacking areas consist of a combination of atoms with high and low energies, as illustrated in Figure 3.12, which leads to them being less affected by changes in the twist angle compared to AA stackings. The significant increase in AA stacking energy, coupled with the relatively smaller variation in AB stacking energy, leads to the observed increase in the energy difference as the angle θ increases.

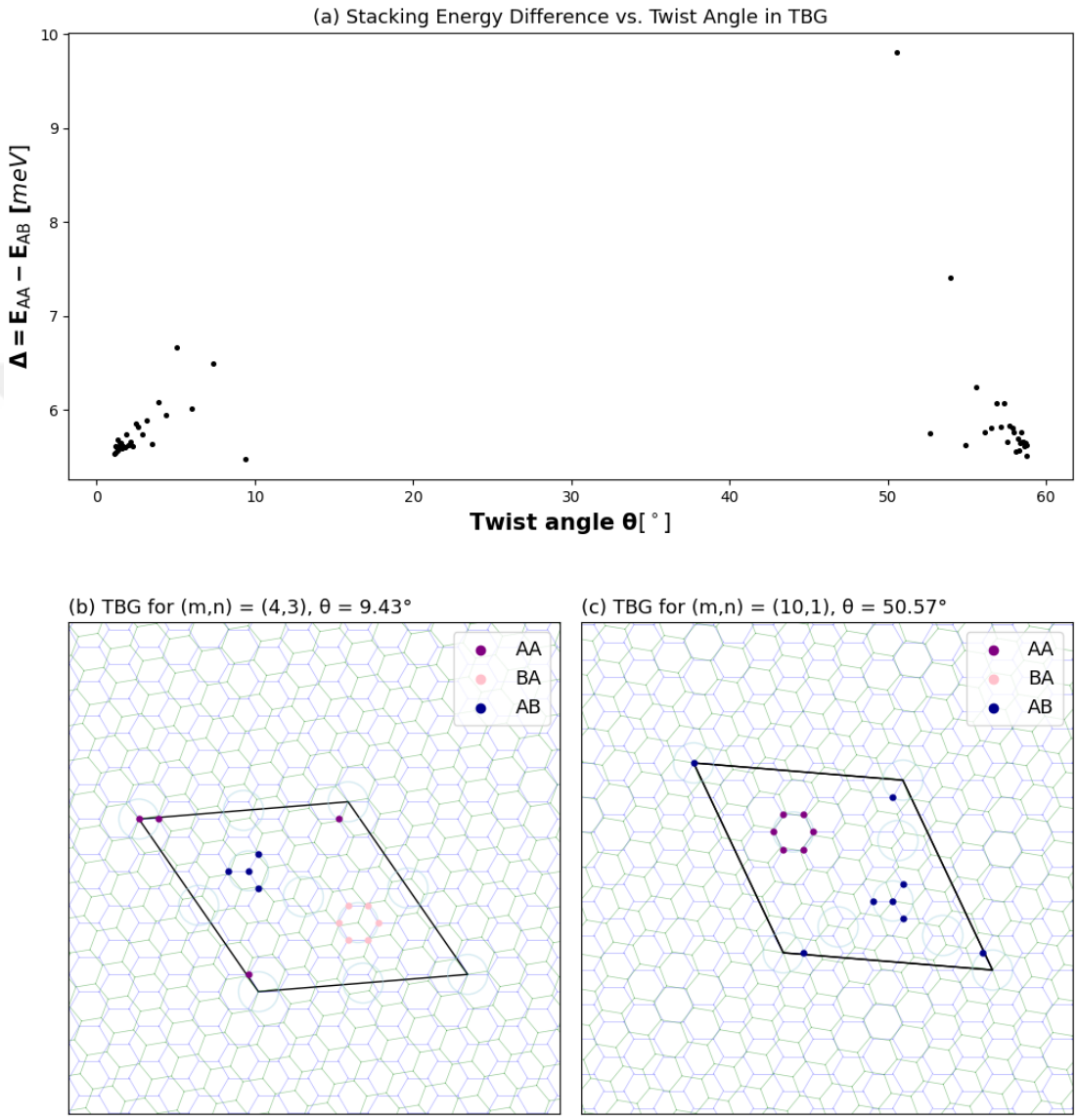

Figure 3.13: (a)Evolution of the energy difference (Δ) between AA and AB stackings in twisted bilayer graphene as the twist angle θ increases from 0° to 60°; (b) TBG structure at $\theta \approx 9.43°$ with indices $(m, n) = (4, 3)$; (c) TBG structure at $\theta \approx 50.57°$ with indices $(m, n) = (10, 1)$.

Another notable observation from the graph is that at an angle close to 10°, we observe the minimum value of Δ. This angle corresponds to the TBG structure with indices $(m, n) = (4, 3)$. To examine this in more detail, Figure 3.13(b)

displays this specific structure. We can see from this figure that the unit cell of this structure is small, containing a limited number of both AA and AB stacked atoms. Analyzing the stacking energies, we find that this structure exhibits the maximum AA stacking energy of $-14.93\,meV/atom$ and the maximum AB stacking energy of all the structures with $-20.41\,meV/atom$. The difference between these two maximum energy values results in a small Δ. Another feature that stands out in Figure 3.13(a) is the TBG structure at an angle of 50.5°, corresponding to the even structure of TBG with $(m, n) = (10, 1)$, shown in figure 3.13(c). When we examine the energies of this structure, we observe that it has a high AA stacking energy of $-15\,meV/atom$ and a minimum AB stacking energy of $-24.81\,meV/atom$, which results in a substantial difference between these energies, leading to a maximum value of Δ. Therefore, Δ is influenced by both the size of the unit cell and the area of the stacking regions within it. This observation aligns with our previous analysis.

In our investigation, we examined the energy contribution of AA and AB stacking configurations in twisted bilayer graphene, where AA represents the highest energy state and AB has the lowest. To quantitatively assess whether these configurations average out in their contribution to the overall interlayer energy, we analyzed the energy ratios across a range of twist angles from 0° to 60°, as depicted in Figure 3.14. Our analysis revealed that these ratios remain nearly constant at approximately 1.35, with only minor variations that disappear when the energy contributions of SP and U atoms are considered. From these findings, we draw the conclusion that despite variations in the atomic structure within each Moiré cell and the presence of different local stacking regions, these differences do not significantly impact the total energy. This is primarily because the energy contributions from AA and AB stacking largely cancel each other out, leading to approximately constant interlayer energy. Consequently, the KC energy remains stable despite variations in the twist angle, as illustrated in Figure 3.5.

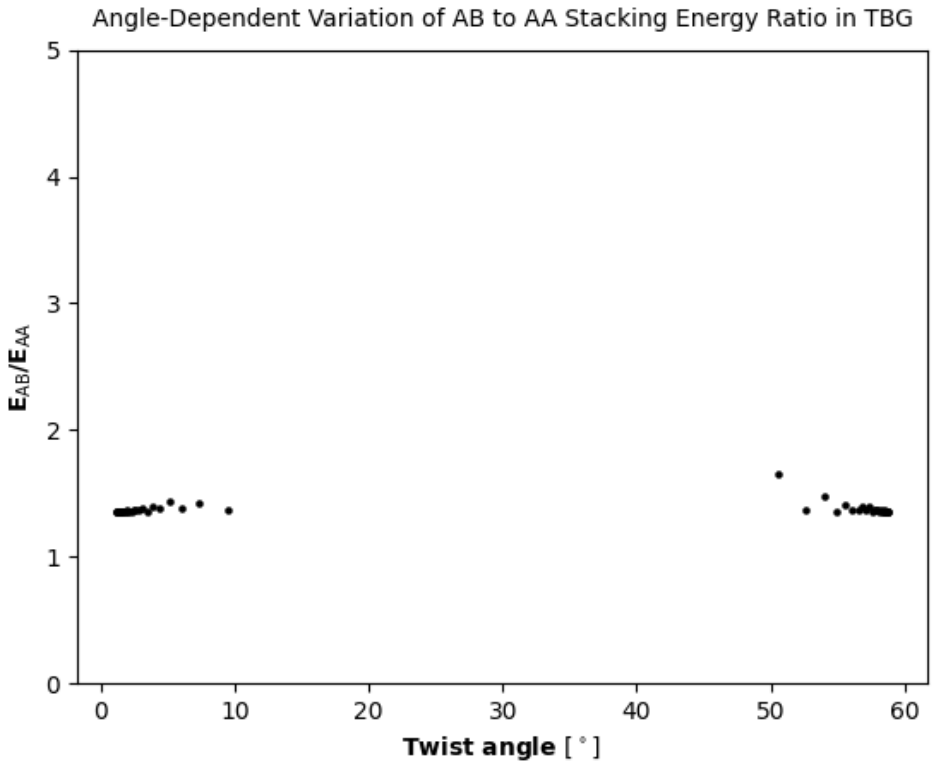

Figure 3.14: Angle-dependent variation of the AB to AA stacking energy ratio (E_{AB}/E_{AA}) in twisted bilayer graphene across twist angles from 0° to 60°.

In summary, our study demonstrates that the intricate atomic variations in twisted bilayer graphene have minimal impact on its total energy, emphasizing its stability for practical applications. This finding advances our understanding of the material's behavior and may inform future research and development in graphene-based technologies.

Chapter 4

Electronic Properties and Band Structures in Twisted Bilayer Graphene

4.1 Electronic Structures of Basic Graphene Configurations: A Review

Twisted bilayer graphene has drawn significant attention due to its exceptional electronic properties, including a linear dispersion relation near the Dirac points.[19] These unique properties hold promise for various technological applications, such as high-speed transistors and quantum computing. The primary objective of this chapter is to plot and analyze the electronic structure of TBG using the tight-binding method.

We begin by reviewing the electronic spectrum and band structures of monolayer and bilayer graphene, including AA-stacked and AB-stacked configurations. This preliminary analysis is crucial for a comprehensive understanding of the band structure of TBG and will provide valuable insights for our subsequent

investigation. We then use this foundational information to delve into the electronic properties of TBG, highlighting its unique characteristics and potential applications.

Two primary methods are commonly employed to derive the electronic spectra of graphene: ab initio Density Functional Theory (DFT) calculations and the tight-binding approximation. While DFT calculations provide accurate results, they are computationally expensive, especially for large unit cells of twisted bilayer graphene with small twist angles. In contrast, the tight-binding approximation presents a more computationally efficient alternative. Consequently, this chapter adopts the tight-binding method to determine the electronic spectra of graphene, utilizing parameters derived from DFT calculations.[20] In this analysis, our focus is on the energy bands near the Fermi level. we will concentrate on the weaker π bonds, which are the primary contributors to graphene's electronic properties. Consequently, our analysis will focus exclusively on the p_z orbitals.[21]

4.1.1 Single Layer Graphene

The initial step involves reviewing the electronic structure of monolayer graphene, whose structure is depicted in Figure 2.1. To construct the Brillouin zone of monolayer graphene, we derive the reciprocal lattice vectors $\mathbf{b}_1$ and $\mathbf{b}_2$, from the lattice vectors $\mathbf{a}_1$ and $\mathbf{a}_2$ defined in Equation 2.1. These vectors can be expressed as follows:

$$\begin{aligned} \mathbf{b}_1 &= \frac{2\pi}{3a_0}[1, \sqrt{3}] \\ \mathbf{b}_2 &= \frac{2\pi}{3a_0}[1, -\sqrt{3}] \end{aligned} \tag{4.1}$$

Using these reciprocal vectors, we construct the first Brillouin zone of monolayer graphene in momentum space. The Brillouin zone is hexagonal, with six vertices known as Dirac points. Among these, the vertices K and K' are shown in the Figure. The center of this structure is denoted as Γ, while M represents the midpoint of the edge of the hexagonal Brillouin zone. These points, along with the denoted vertices, are called high-symmetry points since they remain invariant

under some symmetry operations. It is evident that the Brillouin zone of graphene exhibits six-fold rotational symmetry, also known as hexagonal symmetry.

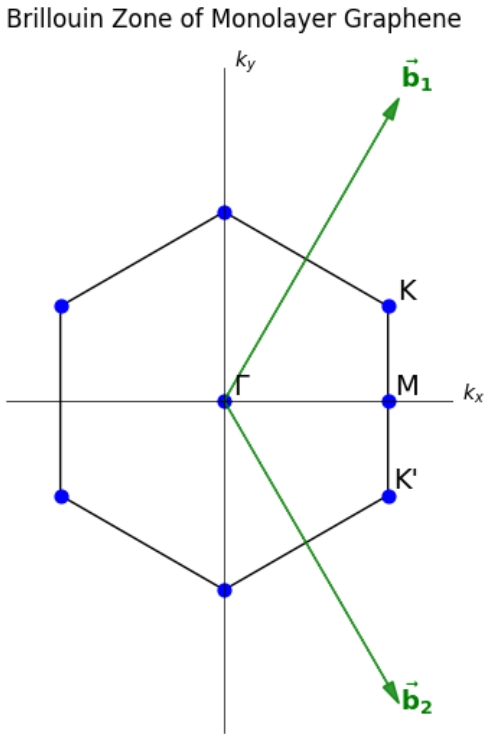

Figure 4.1: The first Brillouin zone of monolayer graphene in momentum space, depicting the reciprocal lattice vectors $\mathbf{b}_1$ and $\mathbf{b}_2$. Key high-symmetry points, including K, K', M, and Γ, are also shown.

A possible choice for the K and K' points is:[20]

$$\begin{aligned} K &= \frac{2\pi}{3a_0}[1, \frac{1}{\sqrt{3}}] \\ K' &= \frac{2\pi}{3a_0}[1, -\frac{1}{\sqrt{3}}] \end{aligned} \tag{4.2}$$

The fundamental tight-binding Hamiltonian for monolayer graphene, in its most simple form, is given by:

$$\hat{H} = -t \sum_{\langle ij \rangle \sigma} a^{\dagger}_{i\sigma} b_{j\sigma} + \text{H.c.}, \tag{4.3}$$

where t represents the nearest-neighbor hopping amplitude, taken to be $2.8meV$ in our calculation. $a^\dagger_{i\sigma}$ and $a_{i\sigma}$ symbolize the creation and annihilation operators for electrons on the A sublattice of position i, and $b^\dagger_{i\sigma}$ and $b_{j\sigma}$ represent the analogous operators for the B sublattice of position j. σ labels the spin projection and the angular brackets signify summation over nearest-neighbor pairs, while $h.c.$ denotes the Hermitian conjugate of the preceding term. To transform the Hamiltonian into momentum space, we employ the Fourier transforms of the a and b operators:

$$a_{k\sigma} = \frac{1}{\sqrt{\mathcal{N}}} \sum_{\mathbf{n}} e^{i\mathbf{k}\cdot\mathbf{r}_n^A} a_{n\sigma}, \quad b_{k\sigma} = \frac{1}{\sqrt{\mathcal{N}}} \sum_{\mathbf{n}} e^{i\mathbf{k}\cdot\mathbf{r}_n^B} b_{n\sigma}, \tag{4.4}$$

where n indexes the unit cells in the honeycomb lattice, $\mathcal{N}$ represents the total number of unit cells, and $\mathbf{r}_n^\alpha$ (α= A,B) corresponds to the position of the atom in the respective sublattice. Applying these operators, and using the identity $\sum_i e^{-i(\mathbf{k}-\mathbf{k}')\cdot\mathbf{r}_i} = \mathcal{N}\delta_{\mathbf{k}\mathbf{k}'}$, the Hamiltonian simplifies to:

$$\hat{H} = -t \sum_{\mathbf{k}\sigma} a^\dagger_{\mathbf{k}\sigma} b_{\mathbf{k}\sigma} \sum_{\delta_j} e^{i\mathbf{k}\cdot\delta_j} + \text{H.c.}, \tag{4.5}$$

where δ_j spans the nearest neighbors of the carbon atom. defining

$$f(\mathbf{k}) = \sum_{\delta_j} e^{i\mathbf{k}\cdot\delta_j} = \exp(-ia_0k_x)\left[1 + 2\exp\left(\frac{3ia_0k_x}{2}\right)\cos\left(\frac{\sqrt{3}a_0k_y}{2}\right)\right], \tag{4.6}$$

and by grouping the electron operators into a spinor: $\Psi^\dagger_{\mathbf{k}\sigma} = (a^\dagger_{\mathbf{k}\sigma}, b^\dagger_{\mathbf{k}\sigma})$, the Hamiltonian can be reformulated as:

$$\begin{aligned} &\hat{H} = \sum_{\mathbf{k}\sigma} \Psi^\dagger_{\mathbf{k}\sigma} \hat{H}_{\mathbf{k}} \Psi_{\mathbf{k}\sigma}, \text{where} \\ &\hat{H}_{\mathbf{k}} = -t \begin{pmatrix} 0 & f(\mathbf{k}) \\ f^*(\mathbf{k}) & 0 \end{pmatrix}. \end{aligned} \tag{4.7}$$

Diagonalizing the $\hat{H}_{\mathbf{k}}$ matrix, we find the eigenvalues, which correspond to the energy spectrum:

$$\varepsilon^{(1,2)}_{\mathbf{k}} = \pm t|f(\mathbf{k})|. \tag{4.8}$$

This analysis reveals that the energy spectrum of graphene consists of two bands, a finding that is consistent with the fact that the unit cell contains two atoms.

The simplest tight-binding Hamiltonian of monolayer graphene is illustrated in Figure 4.2(a), which shows the electronic dispersion of the graphene monolayer. Simultaneously, Figure 4.2(b) illustrates the band structure in momentum space, providing a comprehensive view of the electronic states as a function of wave vector. The upper band, known as the conduction band, and the lower band, referred to as the valence band, are observed to converge at the K point of the Brillouin zone. Given the six-fold symmetry of the Brillouin zone, it can be generalized that these bands intersect at all Dirac points, a characteristic feature of graphene's electronic structure.

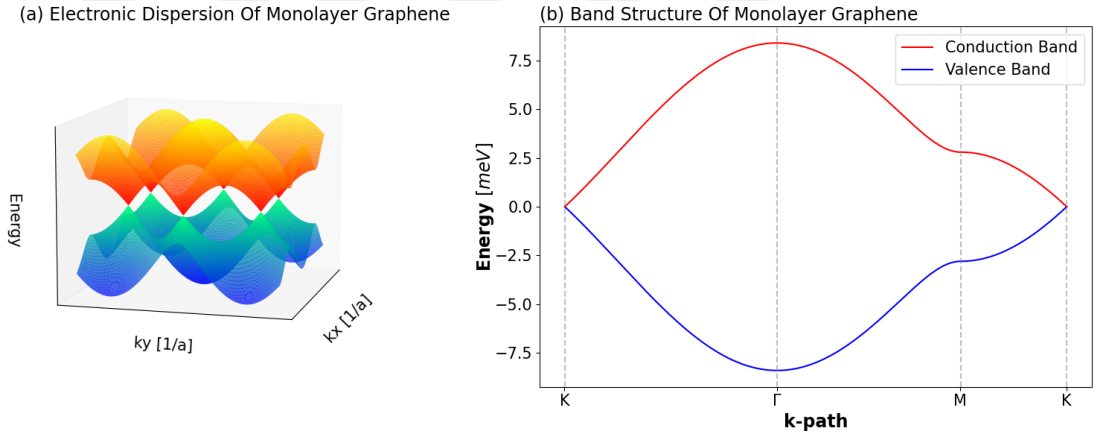

Figure 4.2: (a) Electronic dispersion of monolayer graphene, showing the conduction and valence bands converging at Dirac points. (b) Band structure of monolayer graphene in momentum space, illustrating the energy states as a function of wave-vector along high-symmetry points. The convergence of the bands at the K points is also observed.

In the vicinity of the Dirac point, the electronic dispersion exhibits a linear behavior, implying that the electrons near these points obey an effective massless Dirac equation, behaving as massless pseudo-particles, often termed Dirac fermions.[19] These quasiparticles navigate through the graphene lattice at the Fermi velocity v_F, which can be determined to be $v_F \approx 10^6 m/s$.[22] Because they obey the Dirac equation, these electrons are referred to as Dirac electrons and exhibit unique characteristics. One notable phenomenon derived from the electronic

properties of graphene is the Klein paradox, where, in a one-dimensional configuration, a potential barrier becomes completely transparent to electrons, making it challenging to localize Dirac electrons using an electrostatic potential.[23] Additionally, the quantum Hall effect in graphene is quantized with integer plus half values and can even be observed at room temperature.[19][22] The Hamiltonian in Equation 4.3 is symmetric with respect to electron–hole exchange. This symmetry dictates that the Fermi level in an undoped graphene sample resides at zero energy, corresponding to a state where there is precisely one electron for each carbon atom. In this state, single-layer graphene is classified as a semimetal due to its zero energy gap and zero density of states at the Fermi level.

4.1.2 AA-stacked Bilayer Graphene

The next objective of this investigation focuses on reviewing the electronic structure of bilayer graphene with different stacking configurations. Given their distinct geometries, we anticipate significant differences in their electronic properties. We begin by examining the electronic structure of AA-stacked bilayer graphene, which is illustrated in Figure 4.3(a). The figure also elucidates the unit cell of AA-stacked bilayer graphene, comprising four atoms: A_1 and B_1 from the lower layer, and A_2 and B_2 from the upper layer. Alongside this, Figure4.3(b) presents the Brillouin zone of AA-stacked bilayer graphene depicted with dashed lines, and the BZ of monolayer graphene is shown in faded orange. From this figure, it can be inferred that the BZ of AA-stacked bilayer graphene is identical to that of monolayer graphene.

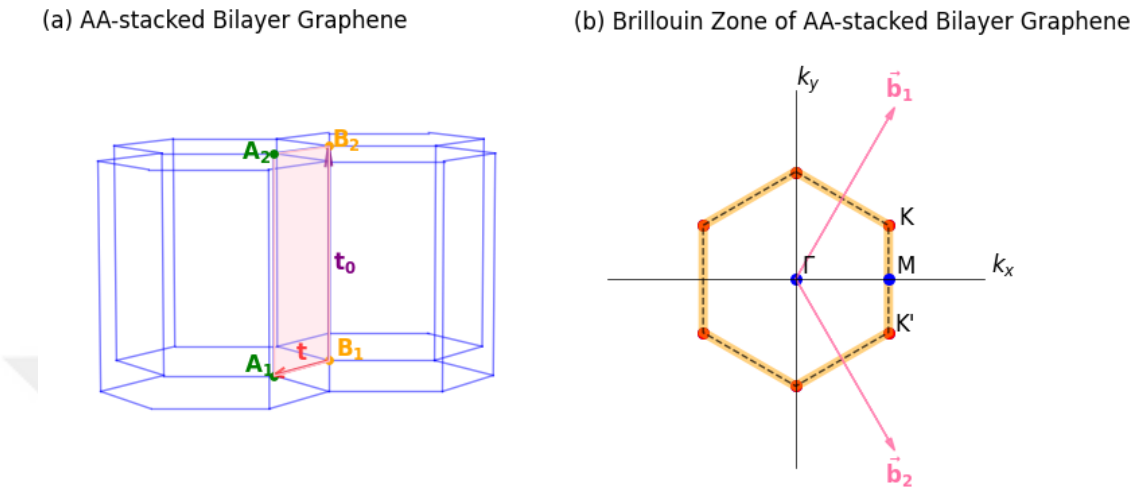

Figure 4.3: (a) Electronic structure of AA-stacked bilayer graphene, illustrating the unit cell composed of four atoms: A1 and B1 from the lower layer, and A2 and B2 from the upper layer. (b) Brillouin zone of AA-stacked bilayer graphene depicted with dashed lines, with the BZ of monolayer graphene shown in faded orange for comparison.

The tight-binding Hamiltonian for all bilayer graphene configurations is generally expressed as the sum of the Hamiltonians for each graphene layer, along with the interaction term between them, denoted as

$$H = H_1 + H_2 + H_{12} \tag{4.9}$$

where H_1 and H_2 are the Hamiltonians of graphene layers 1 and 2, while H_{12} represents the interlayer interaction Hamiltonian. We use a Hamiltonian based on the p_z orbitals of each atom to model the system, which is expressed as follows:

$$\begin{aligned}\hat{H} = &-t \sum_{\langle ij\rangle\alpha\sigma} a^{\dagger}_{i\alpha\sigma} b_{j\alpha\sigma} + t_0 \sum_{i\sigma} \left(a^{\dagger}_{i1\sigma} a_{i2\sigma} + b^{\dagger}_{i1\sigma} b_{i2\sigma} \right) \\ &- t' \sum_{\langle\langle ij\rangle\rangle\alpha\sigma} \left(a^{\dagger}_{i\alpha\sigma} a_{j\alpha\sigma} + b^{\dagger}_{i\alpha\sigma} b_{j\alpha\sigma} \right) + t_g \sum_{\langle ij\rangle\sigma} \left(a^{\dagger}_{i1\sigma} b_{j2\sigma} + a^{\dagger}_{i2\sigma} b_{j1\sigma} \right) + \text{h.c.}\end{aligned} \tag{4.10}$$

The first term in this expression is identical to that encountered in Equation 4.3, corresponding to the in-plane nearest-neighbor hopping of a graphene sheet. The second term accounts for inter-plane interactions, with t_0 being the nearest-neighbor inter-plane hopping amplitude, taken to be $0.35\,meV$ in our calculation.

The subsequent two terms in the expression are associated with the in-layer and interlayer next-nearest-neighbor interactions, which will be neglected in our calculations. The parameters were found by ab initio calculations and they suggest that interplane interactions are an order of magnitude weaker than their inplane counterparts, which is expected given the larger interlayer distance compared to the carbon-carbon bond length. Given that the unit cell of AA-stacked bilayer graphene contains four atoms, it's expected that the electronic structure of this bilayer is constituted by four bands. These bands can be derived using a similar method to that employed for monolayer graphene, where the Hamiltonian is transformed into momentum space and a spinor of four components is defined. The Hamiltonian can be then expressed as

$$H = \sum_{\mathbf{k}\sigma} \Psi^{\dagger}_{\mathbf{k}\sigma} \hat{H}_{\mathbf{k}} \Psi_{\mathbf{k}\sigma}, \text{ where } \hat{H}_{\mathbf{k}} \text{ is a 4x4 matrix given by:}$$

$$\hat{H}_{\mathbf{k}} = \begin{pmatrix} 0 & t_0 & -tf(\mathbf{k}) & 0 \\ t_0 & 0 & 0 & -tf(\mathbf{k}) \\ -tf^{(}\mathbf{k}) & 0 & 0 & t_0 \\ 0 & -tf^{(}\mathbf{k}) & t_0 & 0 \end{pmatrix}. \tag{4.11}$$

From this matrix, the energy bands of AA-stacked bilayer graphene can be calculated to be:[20]

$$\begin{aligned} \epsilon^{(1)}_{0\mathbf{k}} &= -t_0 - t|f(\mathbf{k})|, \epsilon^{(2)}_{0\mathbf{k}} = +t_0 - t|f(\mathbf{k})|, \\ \epsilon^{(3)}_{0\mathbf{k}} &= -t_0 + t|f(\mathbf{k})|, \epsilon^{(4)}_{0\mathbf{k}} = +t_0 + t|f(\mathbf{k})|, \end{aligned} \tag{4.12}$$

These energy bands are plotted in Figure 4.4(b), while Figure 4.4(a) illustrates the electronic dispersion of AA bilayer graphene, where these four bands can be observed. From the energy expressions and Figure 4.4(b), it is evident that the spectrum is composed of two copies of the single-layer graphene spectrum. One set of bands (2 and 4) is shifted to higher energies by the magnitude t_0, while the other set (1 and 3) is shifted to lower energies by the same value. This observation leads to the conclusion that the spectrum, similar to monolayer graphene, exhibits electron-hole symmetry.

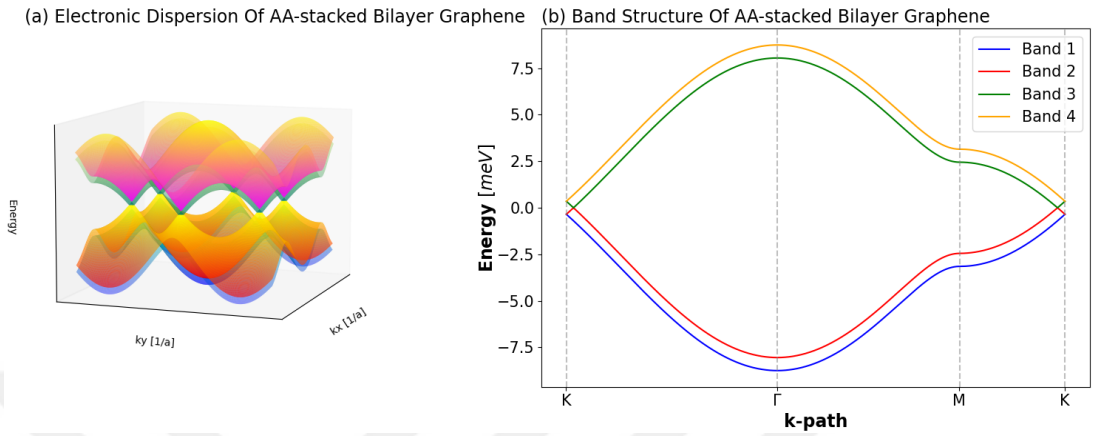

Figure 4.4: (a) Electronic dispersion of AA-stacked bilayer graphene, illustrating the four distinct energy bands. (b) Band structure of AA-stacked bilayer graphene, showing a spectrum that is composed of two copies of the single-layer graphene spectrum. Bands 2 and 4 are shifted to higher energies by the magnitude t_0 , while bands 1 and 3 are shifted to lower energies by the same value.

By analyzing the energies near the Fermi surface, we can conclude that pure AA-stacked bilayer graphene is metallic in nature.[24] Furthermore, it is noteworthy that, similar to the case of single-layer graphene, the spectrum of AA-stacked bilayer graphene is linear near the Dirac points, and the Fermi velocity is determined to be the same as that of monolayer graphene, with a value of $v_F \approx 10^6 m/s$.[25]

4.1.3 AB-stacked Bilayer Graphene

Next, we review the electronic structure of AB-stacked bilayer graphene. The distinct geometry of AB stacking leads us to anticipate different electronic properties compared to the AA-stacked bilayer. The structure and unit cell of the AB-stacked bilayer are depicted in Figure 4.5. The Brillouin zone of AB-stacked bilayer is the same as AA-stacked bilayer, since the fundamental periodicity of the lattice remains unchanged. In the AB bilayer, given that we have pairs of atoms vertically aligned and other pairs where one atom is laterally displaced, it

is anticipated that the aligned pairs will have a more significant contribution to the interlayer binding energy.

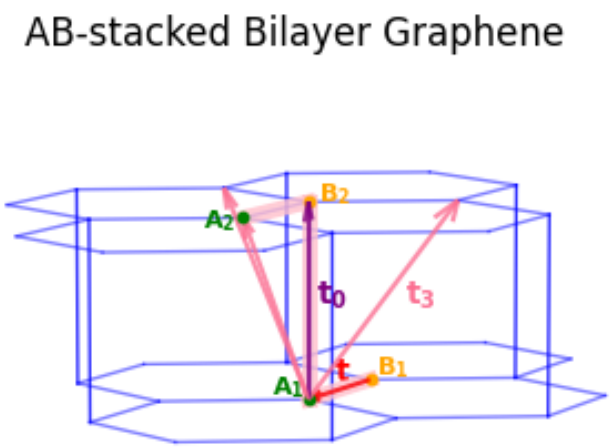

Figure 4.5: Structure and unit cell of AB-stacked bilayer graphene, highlighting the atoms within the unit cell.

Utilizing the same methodology employed in our preceding calculations, we can express the Hamiltonian for AB-stacked bilayer graphene as:

$$\begin{aligned}\hat{H} = &-t \sum_{\langle ij\rangle\alpha\sigma} a^{\dagger}_{i\alpha\sigma} b_{j\alpha\sigma} + t_0 \sum_{i\sigma} \left(a^{\dagger}_{i1\sigma} b_{i2\sigma} + b^{\dagger}_{i1\sigma} a_{i2\sigma} \right) \\ &- t' \sum_{\langle\langle ij\rangle\rangle\alpha\sigma} \left(a^{\dagger}_{i\alpha\sigma} a_{j\alpha\sigma} + b^{\dagger}_{i\alpha\sigma} b_{j\alpha\sigma} \right) + t_3 \sum_{\langle ij\rangle\sigma} \left(a^{\dagger}_{i1\sigma} a_{j2\sigma} + b^{\dagger}_{i2\sigma} b_{j1\sigma} \right) + \text{h.c.}\end{aligned} \tag{4.13}$$

Here, t is, as in Equation 4.3, the inlayer hopping amplitude, while the interlayer hopping amplitude for the aligned pairs is t_0 with a value of $0.35\,meV$, t_3 denotes the next-nearest-neighbor interlayer hopping amplitude, corresponding to the atom pairs that are not aligned, with the value of $t_3 = 0.3\,meV$. t' denotes the next-nearest-neighbor inlayer hopping amplitude, and this summation was disregarded in these calculations, as it was in previous calculations. By transforming the Hamiltonian into k-space and employing the four-component spinor,

we can formulate the Hamiltonian in k-space as

$$H_{\mathbf{k}}^{AB} = \begin{pmatrix} 0 & 0 & -tf(k) & t_3 f^*(k) \\ 0 & 0 & t_0 & -tf(k) \\ -tf^*(k) & t_0 & 0 & 0 \\ t_3 f^*(k) & -tf^*(k) & 0 & 0 \end{pmatrix}. \tag{4.14}$$

By diagonalizing the Hamiltonian matrix, we are able to determine our four energy bands:[20]

$$\begin{aligned} \left(\varepsilon_{\mathbf{k}}^{(1,4)}\right)^2 &= t^2|f(\mathbf{k})|^2 + \frac{1}{2}t_0^2 + \sqrt{t_0^2 t^2 |f(\mathbf{k})|^2 + \frac{1}{4}t_0^4}, \\ \left(\varepsilon_{\mathbf{k}}^{(2,3)}\right)^2 &= t^2|f(\mathbf{k})|^2 + \frac{1}{2}t_0^2 - \sqrt{t_0^2 t^2 |f(\mathbf{k})|^2 + \frac{1}{4}t_0^4}. \end{aligned} \tag{4.15}$$

These energy bands are illustrated in Figure 4.6(b) and can also be seen in Figure 4.6(a), where we have plotted the electronic dispersion of AB-stacked bilayer graphene.

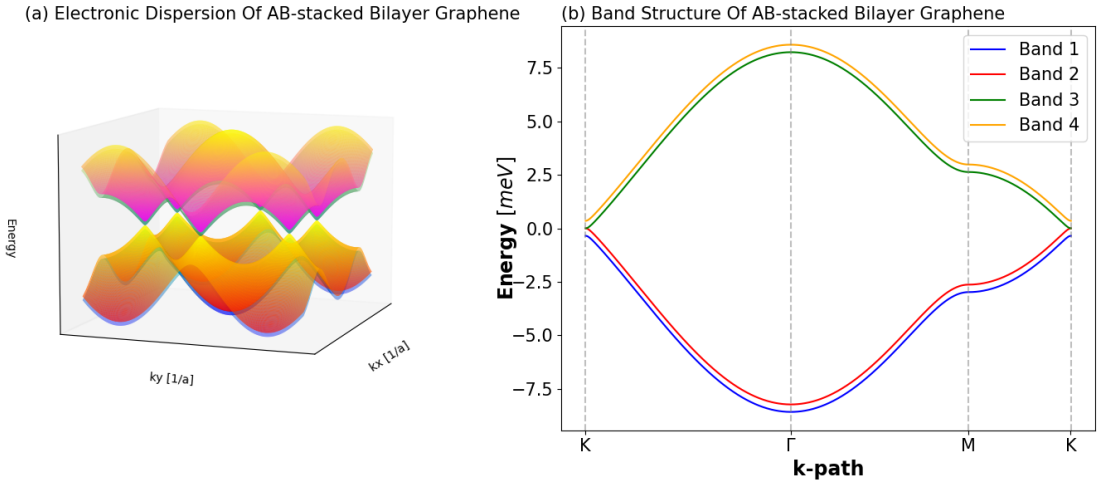

Figure 4.6: (a) Electronic dispersion of AB-stacked bilayer graphene. (b) Band structure of AB-stacked bilayer graphene, showing a parabolic dispersion near the Dirac points. Bands 2 and 3 converge at the Dirac points, while bands 1 and 4 are separated by an energy gap.

From Figure 4.6(b), it is evident that, unlike monolayer and AA-stacked bilayer graphene, the band structure of this system exhibits a parabolic dispersion in

the vicinity of the Dirac points. Additionally, bands 2 and 3 converge at the Dirac points, whereas the remaining bands, 1 and 4, are separated by an energy gap. The quadratic dispersion implies that AB bilayer graphene possesses a non-zero effective mass, and the Fermi velocity is reduced due to interlayer coupling. However, similar to monolayer graphene, AB-stacked bilayer graphene remains a semimetal.[26]

4.2 Twisted Bilayer Graphene: Structural and Electronic Properties

After reviewing the AA and AB configurations of bilayer graphene, we have understood that the structural geometry significantly influences the electronic characteristics of the system. With this understanding, we proceed to the subsequent step of investigating the electronic structures in twisted bilayer graphene. Twisted bilayer graphene consists of two graphene layers initially stacked with an interlayer separation distance, in our calculation, the original stacking is an AA configuration and the interlayer distance is $d_0 = 3.35$Å. The rotation of the top layer leads to a misalignment where the interlayer distance varies based on the lateral distance between atoms. To conduct reliable first-principles calculations on twisted bilayer graphene with varying twist angles, we need to develop a tight-binding Hamiltonian that incorporates distance-dependent parameters. This Hamiltonian can be expressed as the sum of the Hamiltonians for each individual graphene layer, along with an additional term describing the electron hopping between these layers, as shown in Equation 4.9. A significant challenge encountered in the study of TBG is that the size of the unit cell varies with the twist angle. At small angles, the unit cell size increases significantly, containing tens of thousands of atoms for angles below 2°. This substantial increase in unit cell size makes calculations computationally expensive. Nonetheless, through the application of advanced computational methods and the utilization of supercomputers, we have successfully generated band structure plots for large unit cells, incorporating up to 11908 atoms per unit cell, for the structure with the twist angle of 1.05°. In

the proceeding section, we will introduce and discuss our methodology. Before this, however, it will be useful to visualize the structures of several twisted bilayer graphene configurations and examine their respective Brillouin zones. In Figure 4.7(a), we depict the twisted bilayer graphene structure that corresponds to the parameters $(m, n) = (2, 1)$, exhibiting a twist angle of 21.787°. This particular configuration represents the TBG structure with the smallest unit cell. When a graphene layer is twisted, a Moiré superlattice with a periodicity larger than the original graphene lattice forms, altering the corresponding Brillouin zone. The reciprocal vectors of this superlattice structure are derived as follows:

$$\begin{aligned} \mathbf{B}_1 &= \mathbf{b}_1 - \mathbf{b}_1' \\ \mathbf{B}_2 &= \mathbf{b}_2 - \mathbf{b}_2' \end{aligned} \tag{4.16}$$

Utilizing these vectors, we identified the Brillouin zone of the superlattice and the corresponding Dirac points, which we designated as K_M and K'_M. In Figure 4.7(b), this Brillouin zone is illustrated. The high-symmetry points of the BZ of the twisted bilayer system are depicted in green, and the corresponding reciprocal lattice vectors found from Equation 4.16 are also shown.

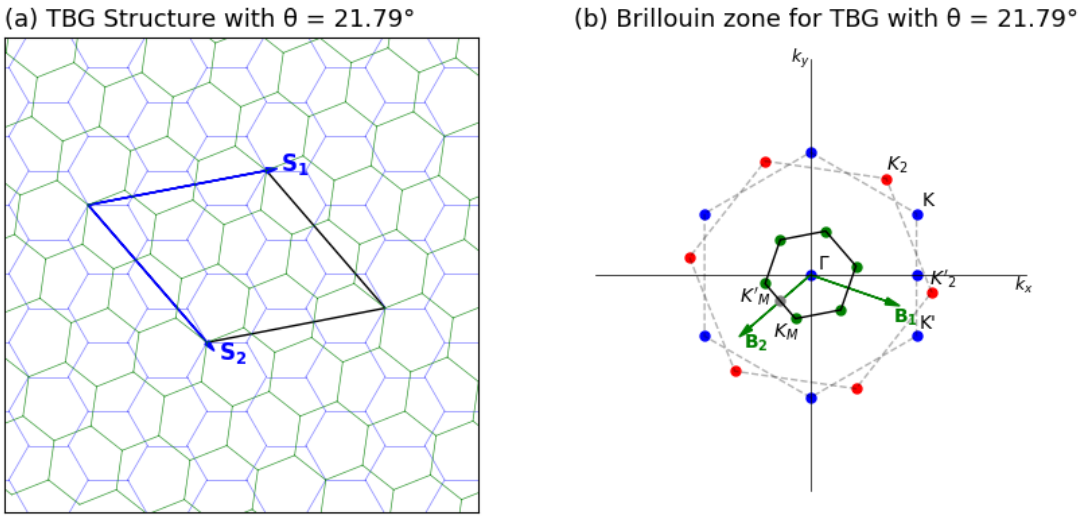

Figure 4.7: (a) The twisted bilayer graphene structure with a twist angle of 21.787°. (b) The Brillouin zone of the corresponding twisted bilayer graphene, alongside the Brillouin zones of the individual graphene layers. Vertices and high-symmetry points the reciprocal lattice vectors of the twisted bilayer BZ are depicted in green

For the purpose of comparison, we plotted in Figure 4.8(a) the TBG formed by the parameters $(6, 5)$ and a twist angle of $6°$. In Figure 4.8(b), its BZ in momentum space is depicted, and it is evident that this BZ is significantly smaller than the one depicted in Figure 4.7(b), corresponding to a structure with a larger twist angle.

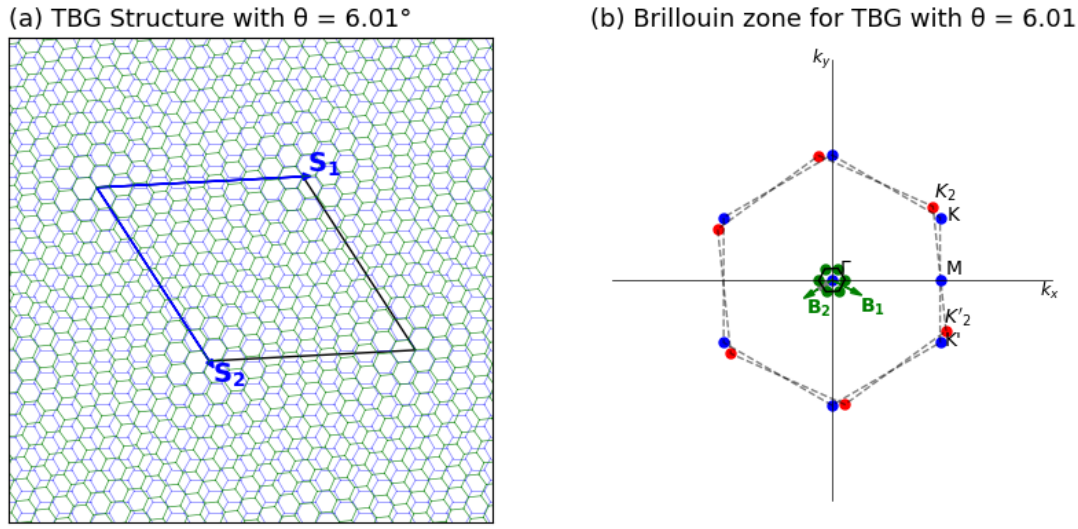

Figure 4.8: (a) The twisted bilayer graphene structure with a twist angle of $6°$, with the corresponding unit cell and lattice vectors plotted.(b) The Brillouin zone in momentum space, showing a significantly smaller BZ compared to Figure 4.7(b).

After observing these characteristics, we adopt a procedure to investigate the electronic properties of the TBG structures by plotting the band structure using the tight-binding Hamiltonian. Initially, we utilize the BZ and its symmetry to determine a **k**-path, along which we will compute the electronic band structure. This trajectory connects high-symmetry points: The center of the BZ Γ, the Dirac point K, and the midpoint of the edge of the Brillouin zone, M. This approach is effective because many properties are symmetric around these points, allowing us to avoid the computational complexity of calculating the band structure across the entire BZ, and capturing the essential features of the band structure. To plot the Hamiltonian, we first determine the number of carbon atoms in the unit cell using Equation 2.6 The Hamiltonian in momentum space is an $N \times N$ matrix

and is given by:[27]

$$\hat{H} = -t \sum_{\langle ij \rangle \alpha\sigma} a^{\dagger}_{i\alpha\sigma} b_{j\alpha\sigma} + t_{ij,pp\sigma}(R_i, R_j) \sum_{i\sigma} (c^{\dagger}_{i1\sigma} c_{i2\sigma}) + h.c. \tag{4.17}$$

The first term in this equation corresponds to the Hamiltonian of monolayer graphene, as seen in Equation 4.3, with the summation over α indicating summation over the two layers. The second term represents the interlayer hopping term, where $c_{i\alpha\sigma}$ is an annihilation operator, and it can correspond to either A or B atom, depending on the atom interacting. The summation extends over all atoms in the bottom layer and their corresponding interaction partners from the top layer, thereby calculating the interaction between them. The annihilation operator c_α is defined as:[27]

$$c_\alpha(\mathbf{r}) \rightarrow v_c^{1/2} \psi_{1,\alpha}(\mathbf{r}) \exp(\mathrm{i}\mathbf{k} \cdot \mathbf{r}), \tag{4.18}$$

In the context of TBG, the interlayer bond separation is not uniform across all atoms due to the displacement induced by the twist angle. The distance between the interacting atoms, denoted as $\mathbf{r}_{ij}$, is given by:

$$\mathbf{r}_{ij} = \sqrt{\rho_{ij}^2 + d_0^2} \tag{4.19}$$

where ρ_{ij} is the transverse distance between the atom in the bottom layer i, and the projection of the top layer atom j onto the plane of the first layer. The term $t_{ij}(R_i, R_j)$ observed in Equation 4.17 is the transfer integral between these two atoms, which is defined as:[5]

$$t(\mathbf{R}_i, \mathbf{R}j) = Vpp\pi \left[1 - \left(\frac{\mathbf{r_{ij}} \cdot \mathbf{e}_z}{|\mathbf{r}_{ij}|} \right)^2 \right] + Vpp\sigma \left(\frac{\mathbf{r_{ij}} \cdot \mathbf{e}_z}{|\mathbf{r}_{ij}|} \right)^2, \tag{4.20}$$

where[28]

$$\begin{aligned} V_{pp\pi} &= -\gamma_0 \exp\left(q_\pi \left(1 - \frac{|\mathbf{r}_{ij}|}{a_0} \right) \right) \\ V_{pp\sigma} &= \gamma_1 \exp\left(q_\sigma \left(1 - \frac{|\mathbf{r}_{ij}|}{d_0} \right) \right) \quad \text{with} \quad \frac{q_\sigma}{d_0} = \frac{q_\pi}{a_0} \end{aligned} \tag{4.21}$$

Here, the γ_0 and γ_1 parameters were adjusted to replicate the velocity of monolayer graphene and the average interlayer interaction, with $\gamma_0 = t$, being the

inlayer hopping amplitude, set to be $2.8\,meV$ in our calculations, and $\gamma_1 = t_0$, the interlayer hopping amplitude, equal to $0.35\,eV$. It is important to note that in Equation 4.17, the term $t(\mathbf{R}_i, \mathbf{R}j)$ was employed exclusively for calculating the interlayer interaction; hence, we have utilized the second term of Equation 4.20 only. Utilizing these definitions, we formulated the Hamiltonian for our TBG structures by determining the interaction of each bottom layer atom in the unit cell with its nearest neighbor from the second layer, along with the inlayer interactions for atoms in both layers with their nearest neighbors, and incorporating these interactions into the $N \times N$ H_k matrix. The interaction is given by:

$$I = \gamma_{ij}(\mathbf{k}) t_{ij}(\mathbf{k}) \tag{4.22}$$

where $\gamma_{ij}(\mathbf{k}) = e^{i\mathbf{k}\cdot\mathbf{r}_{ij}}$ and $t_{ij}(\mathbf{k}) = t_0 e^{-\beta(|\mathbf{r}_{ij}|-d_0)}$ for interlayer hopping and $t_{ij}(\mathbf{k}) = te^{-\beta(|\mathbf{r}_{ij}|-a_0)}$ for inlayer hopping, with $\beta = 3.37$ being the decay parameter. Employing all the preceding definitions, we computed all the inlayer and interlayer interactions and positioned them within the matrix. Subsequently, we calculated the eigenvalues of this matrix along the $\mathbf{k}$-path, allowing us to derive the band structures of various TBG configurations. Using this method, we plotted various band structures, some of which can be observed in Figure 4.9. This figure shows the band structures of TBG with twist angles of (a) 27.796°, (b) 9.43°, and (c) 4.408°.

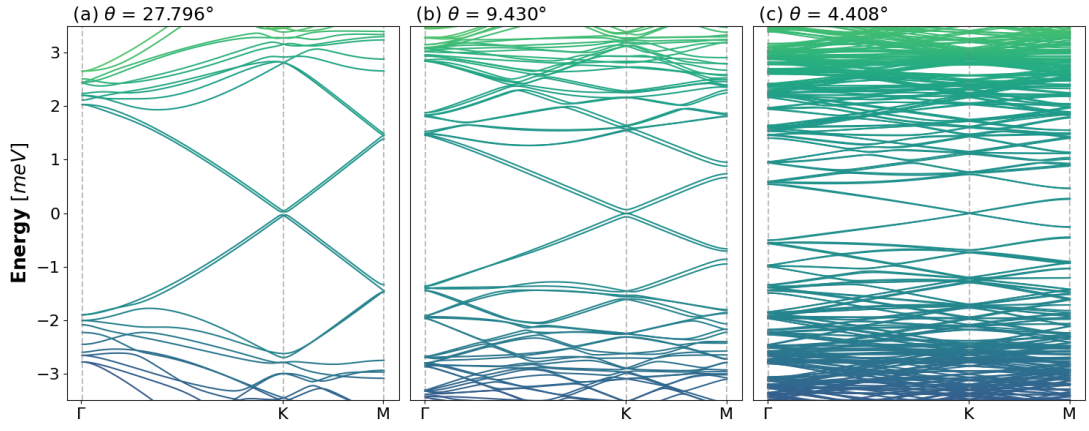

Figure 4.9: Band structures of twisted bilayer graphene (TBG) at different twist angles: (a) $(m, n) = (5, 2)$, $\theta = 27.796°$; (b) $(m, n) = (4, 3)$, $\theta = 9.43°$; (c) $(m, n) = (8, 7)$, $\theta = 4.408°$.

With these results in hand, we now proceed to a comprehensive analysis of the electronic spectra. The primary objective of this analysis is to examine the influence of the twist angle on the electronic properties and identify distinctive characteristics by analyzing the linearity near the Dirac points, as well as investigating the Fermi velocity and assessing the effective mass of the charge carriers. Additionally, we will conduct various other examinations to gain a deeper understanding of the electronic behavior influenced by the twist angle. It is noteworthy that TBG structures exhibit symmetry around the twist angle of 30°, as seen in Chapter 2. Consequently, the electronic properties under investigation are also symmetric with respect to this angle. Therefore, we focus our analysis on twist angles smaller than 30°. In twisted bilayers, the Moiré pattern generated by the superposition of two graphene layers induces a periodic interaction that couples the two Dirac electron gases. This interaction forms a large superlattice, which restores Dirac-like linear dispersion [28], a phenomenon clearly depicted in Figure 4.9 and Figure 4.10.

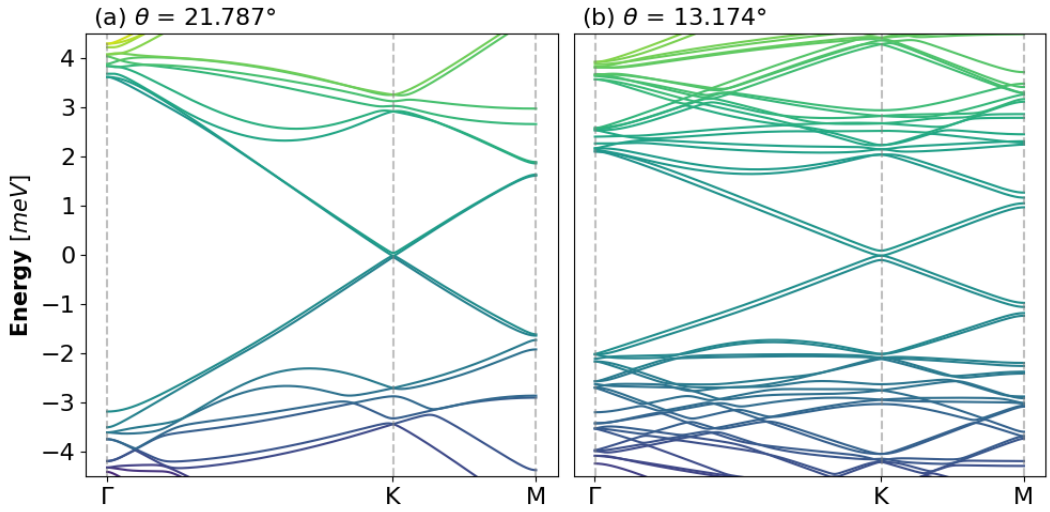

Figure 4.10: Band structures of twisted bilayer graphene at different twist angles: (a) $(m, n) = (2, 1)$, $\theta = 21.787°$; (b) $(m, n) = (3, 2)$, $\theta = 13.174°$.

To further investigate this linear dispersion, we calculate the electron velocity at the Fermi level of the band structures depicted in Figure 4.10 and compare it with the velocity in monolayer graphene. For this purpose, we employ the

equation

$$v_F = \frac{1}{\hbar}\frac{\partial E}{\partial k} \tag{4.23}$$

where $\hbar$ is the reduced Planck's constant, equal to $\hbar \approx 6.58212 \times 10^{-16}\, eVs$. By performing these calculations, we find that the Fermi electrons in TBG at angles 21.787° and 13.174° exhibit velocities close to those of single-layer graphene. These results are illustrated in Figure 4.12, which will be introduced later in this section. From the observed behavior, we can infer that at larger twist angles, the Fermi velocity approaches that of monolayer graphene, consistent with the findings of Ref. [29]. Under these conditions, the rotated graphene bilayers behave as two isolated layers, with the interaction term being negligible due to the weak coupling between the layers under these conditions.[30] In our next step, we proceed to investigate these properties for TBG with smaller twist angles.

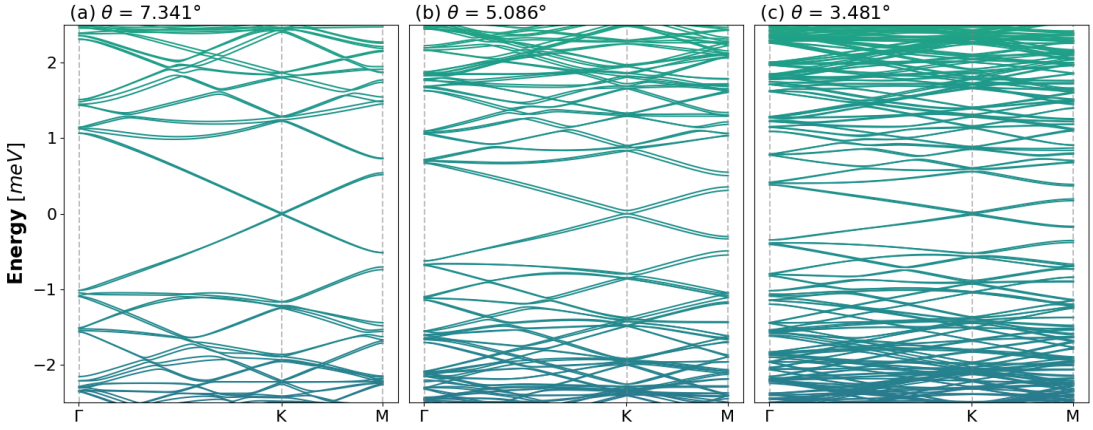

Figure 4.11: Band structures of twisted bilayer graphene at different twist angles: (a) $\theta = 7.341°$; (b) $\theta = 5.086°$; (c) $\theta = 3.481°$. As the twist angle decreases, the band structures exhibit linear dispersion around the K point, with a noticeable reduction in the slope of the bands near the Fermi level.

In Figure 4.11, we present the band structures of three TBG structures with angles of 7.341°, 5.086°, and 3.481°. These band structures also exhibit linear dispersion around the K point; however, there is a noticeable reduction in the slope of the bands close to Fermi level. To further investigate this behavior, we calculated the Fermi velocity for TBG structures with twist angles ranging from

0° to 30° using Equation 4.23, and plotted the results in Figure 4.12. This figure clearly illustrates a renormalization of the Fermi velocity, showing a decrease from values comparable to those of monolayer graphene at larger angles to significantly reduced velocities at smaller angles. This reduction has been confirmed by Lopez dos Santos.[27]

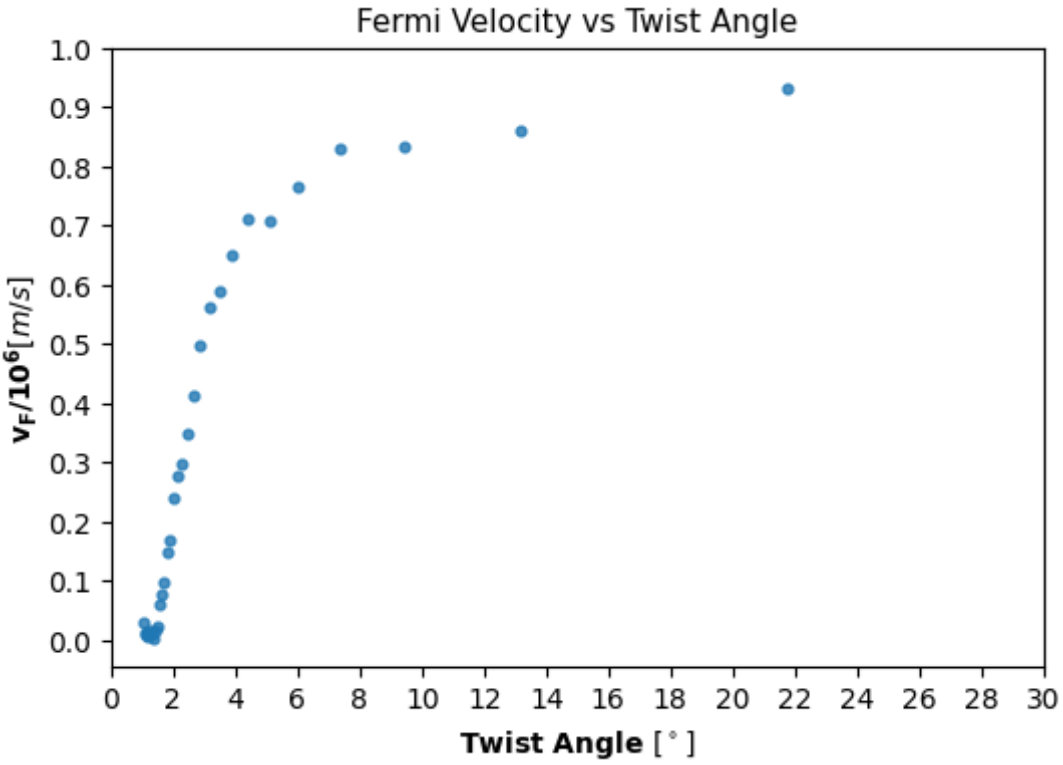

Figure 4.12: Fermi velocity (v_F) as a function of twist angle for twisted bilayer graphene structures, expressed as a fraction of the Fermi velocity of monolayer graphene. The plot indicates that the Fermi velocity increases with the twist angle, approaching the value for monolayer graphene at larger angles.

As we have observed from the preceding figures, the bands around the Fermi level become less dispersive as the angle decreases. To investigate the so-called "magic angles" of TBG, which have been extensively discussed in numerous studies [31][32], we generated band structures for small angles and we plotted them in Figure 4.13. At these small angles, the bands around the Fermi level show significant flattening. Notably, at an angle of 1.248°, the bands near fermi levels

become completely flat. The Fermi velocities of the TBG structures with small twist angles are presented in Figure 4.12, where it is evident that as the bands around the Fermi level flatten at magic angles, the Fermi velocity approaches zero. These observations align with the results obtained from previous band structure calculations.[28][31]

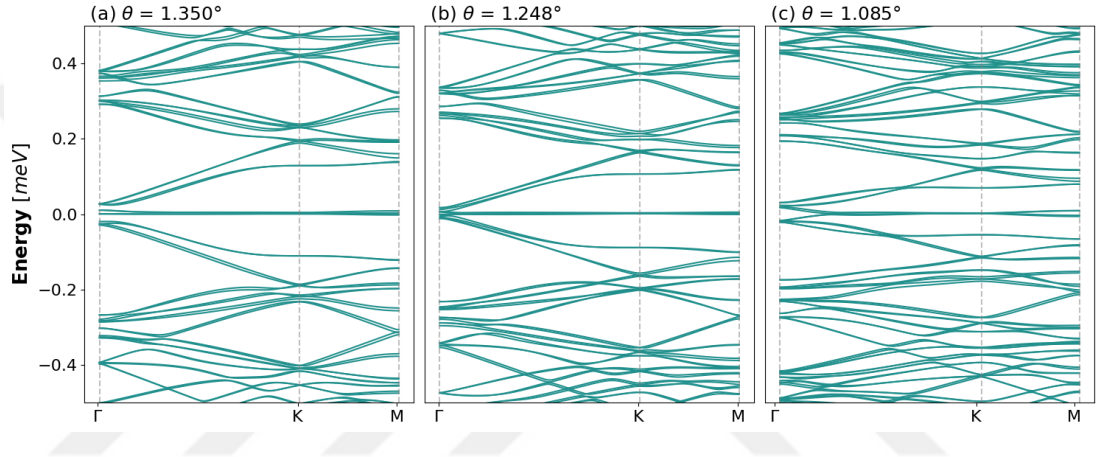

Figure 4.13: Band structures of twisted bilayer graphene at small twist angles: (a) $\theta = 1.350°$; (b) $\theta = 1.248°$; (c) $\theta = 1.085°$. The bands near the Fermi level exhibit significant flattening, with nearly flat bands observed at $\theta = 1.248°$.

To further investigate the band flattening near the Fermi level, we calculated the bandwidth of this band in various TBG configurations and plotted the results in Figure 4.14. The data clearly show that at small twist angles, the bandwidth of the Fermi band approaches zero, confirming the presence of flat bands. The emergence of flat bands at small twist angles can be attributed to the prominent Moiré pattern in TBG, which induces inhomogeneity and causes electron orbitals to localize at specific AA regions.[27] These flat bands are half-filled, suggesting that magnetic behavior arises when we twist the BLG structure by a small value. The reduced kinetic energy of electrons in these bands leads to electron localization and strong correlation effects, resulting in distinctive behaviors such as superconductivity or Mott insulators.[1]

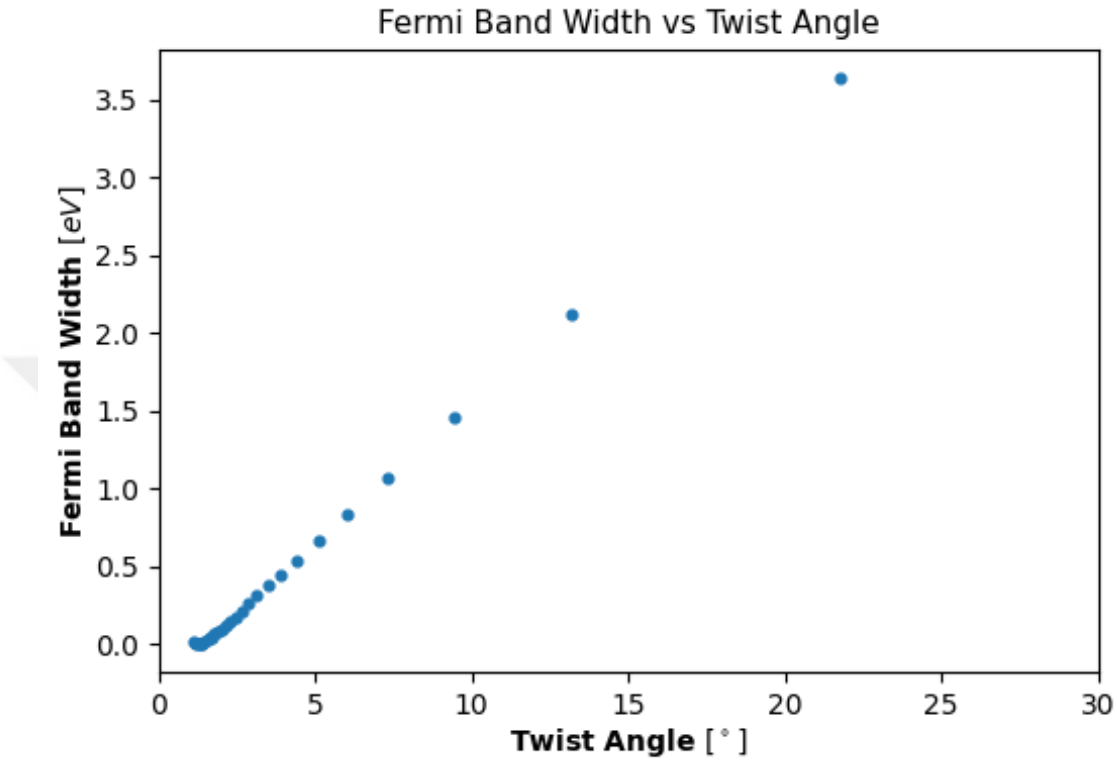

Figure 4.14: Fermi bandwidth as a function of twist angle for twisted bilayer graphene. The plot illustrates that at small twist angles, the bandwidth of the Fermi band approaches zero, confirming the presence of flat bands.

Based on our observations from Figures 4.10, 4.11, and 4.13, it is evident that the band gap around the Fermi level along the varies with increasing angle. To illustrate this behavior, Figure 4.15 presents this variation at several points along the ΓK path. It is important to note that the distance of the $\Gamma - K$ path changes with the twist angle due to variations in the size of the Brillouin zone. While Figure 4.15(a) shows the variation of the band gap at the Γ point as a function of the twist angle, Figure 4.15(b) presents this variation at the midpoint between Γ and K, and Figure 4.15(c) illustrates it at two-thirds of ΓK path. Finally, Figure 4.15(d) presents the band gap at the K point itself. It is evident that the variation of the band gap near the K point deviates from linearity, unlike the linear behavior observed in Figures 4.15(a), 4.15(b), and 4.15(c). This indicates that the linearity is disrupted in the vicinity of the K point.

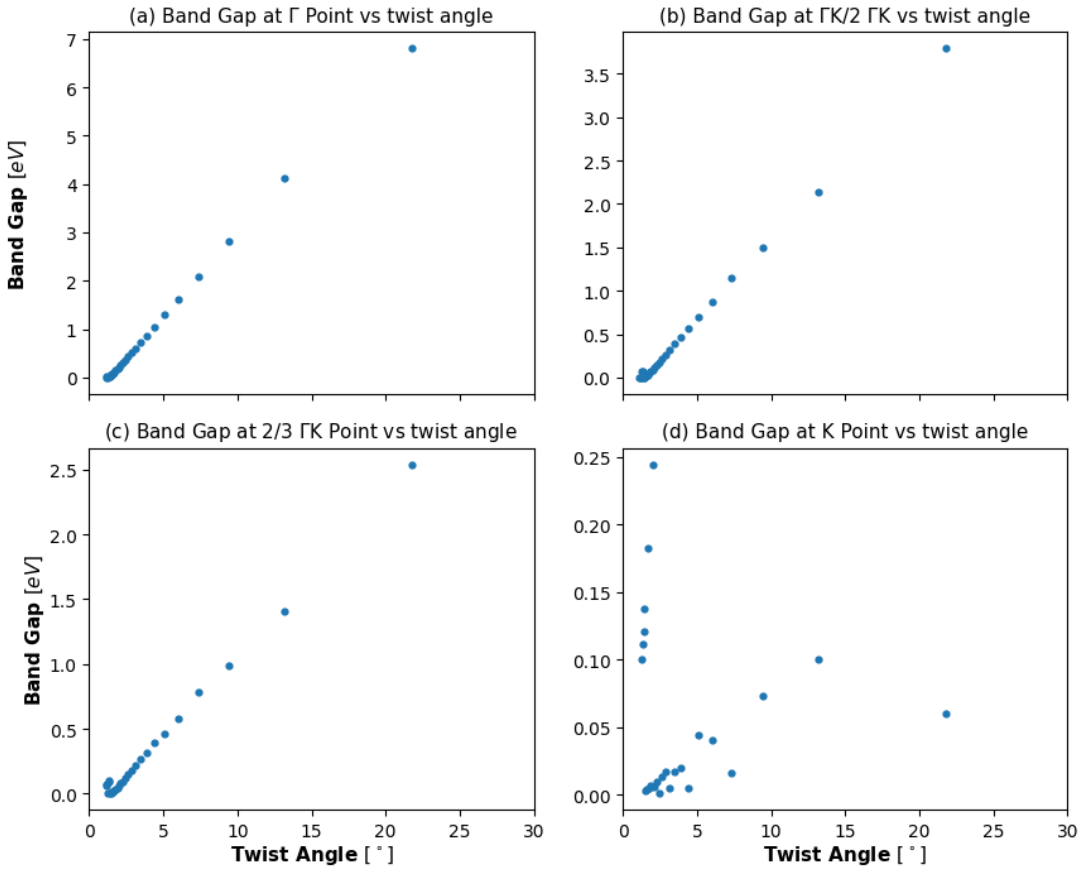

Figure 4.15: Variation of the band gap along the ΓK path with different twist angles. The subfigures show the band gap at (a) Γ point; (b) the midpoint between Γ and K; (c) Two-thirds of the ΓKpath; (d) K point. The deviation from linearity near the K point indicates a disruption in linearity in this region.

Subsequently, in our investigation, we aim to calculate the effective mass of electrons in twisted bilayer graphene. To achieve this, we utilized the definition provided in Ref. [33], which states:

$$m^* = \frac{p}{v_g} = \hbar^2 k (\frac{\partial E}{\partial k})^{-1} \tag{4.24}$$

Here, p represents the momentum in real space, v_g is the group velocity, and $\hbar$ is the reduced Planck constant, as previously defined. By applying this formula, we were able to determine the electron effective mass for twisted bilayer graphene structures. Figure 4.16 presents the outcomes of these calculations, highlighting

the effective mass's dependence on twist angle.

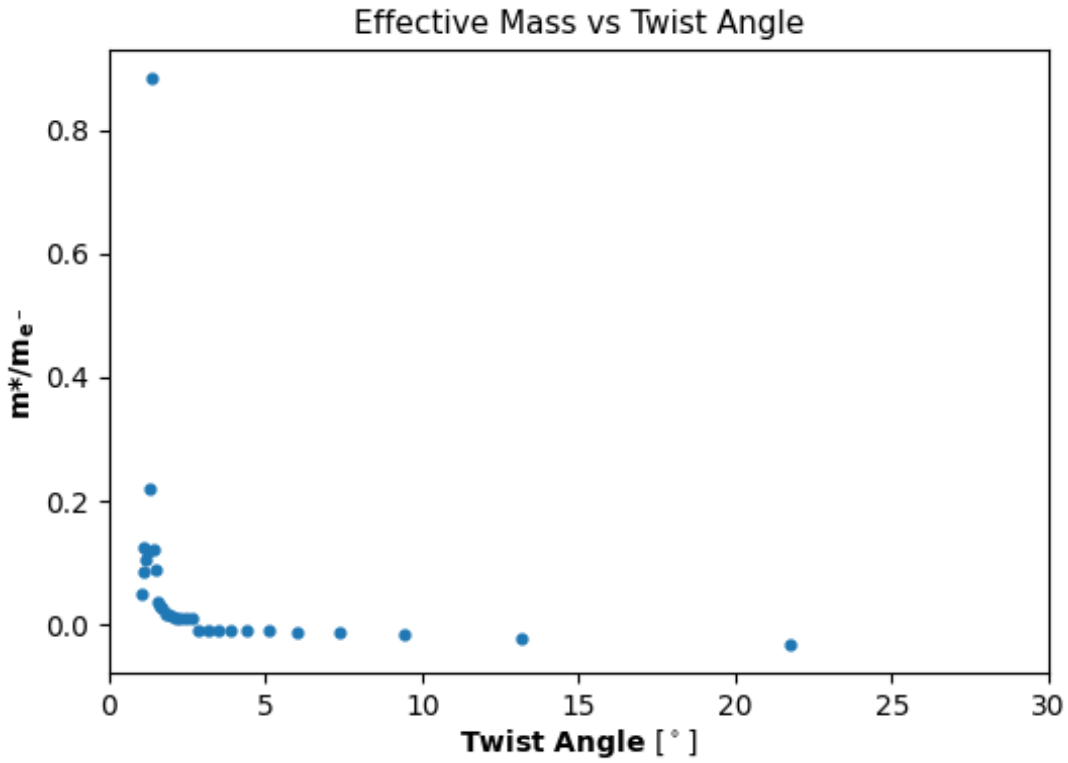

Figure 4.16: Ratio of the effective mass (m^*) to the electron mass (m_e) in twisted bilayer graphene as a function of twist angle.

During our investigation, we calculated the band structures for a wide range of twist angles, each constructed using various pairs of lattice vector parameters. In the course of these calculations, we observed a peculiar behavior at certain twist angles. While the band structures of the previously plotted TBG systems exhibited a single band crossing at zero energy at the Dirac point K, other configurations with distinct lattice parameters demonstrated an unusual behavior, where their bands crossed multiple times at various locations along the k-path. Examples of these structures are shown in Figure 4.17. In Figure 4.17(a), the symmetry around the band crossing locations is evident, indicating that the multiple crossings are symmetric repetitions of the same band structure. By analyzing these figures, we find that the number of crossings corresponds to the absolute difference between the lattice vector parameters ($|m - n|$). This observation is

consistent with our previous calculations, where $|m - n| = 1$ resulted in a single crossing.

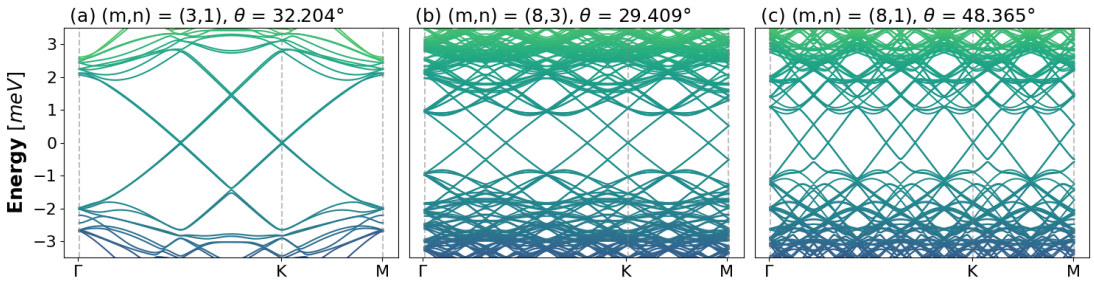

Figure 4.17: Band structures in twisted bilayer graphene systems for (a) $(m, n) = (3, 1)$ at a twist angle of 32.204°. (b) $(m, n) = (8, 3)$ at a twist angle of 29.409°. (c) $(m, n) = (8, 1)$ at a twist angle of 48.365°. The number of crossings at zero energy level in these band structures corresponds to the difference between the lattice vector parameters ($|m - n|$).

To investigate this behavior, we selected a twisted bilayer graphene structure with a twist angle of 32.204°, illustrated in Figure 4.17(a), then we untwisted the top layer, restoring it to its original AA stacking configuration. The resulting structure is depicted in Figure 4.18(a), and its corresponding band structure is shown in Figure 4.18(b). This band structure reveals a clear occurrence of band folding. These observations led us to conclude that the unusual features seen in Figure 4.17 are also a result of band folding.

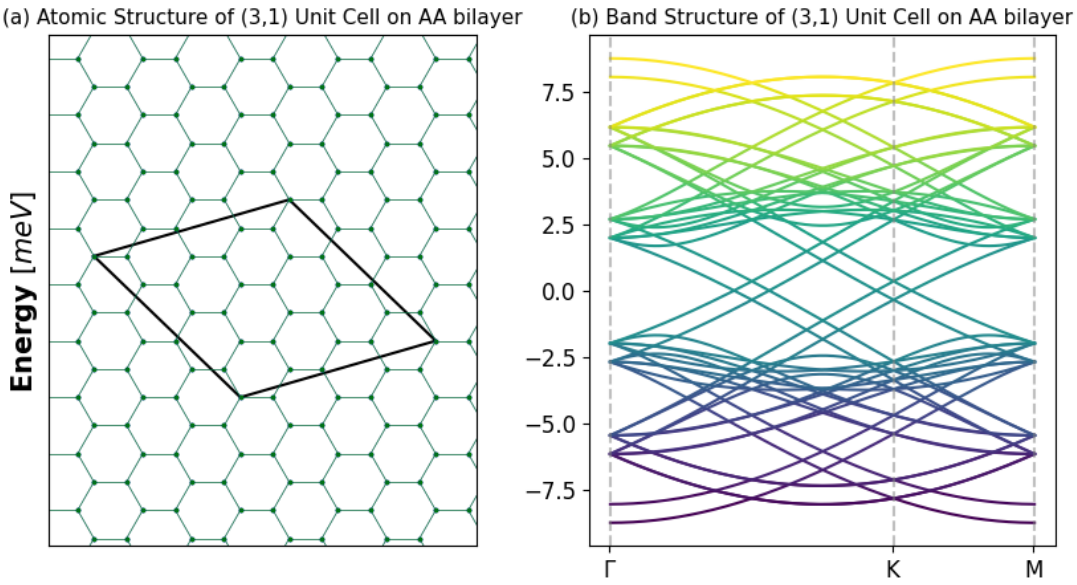

Figure 4.18: (a) Atomic structure of the $(3, 1)$ unit cell plotted on an AA-stacked bilayer, obtained by untwisting the top layer of the TBG structure with a twist angle of 32.204°. (b) Corresponding band structure of the $(3, 1)$ unit cell on AA-stacked bilayer graphene, showing the effects of band folding.

Consequently, we attribute the observed effects and multiple band crossings to this phenomenon. Band folding arises due to the enlarged dimensions of the corresponding unit cell. As the difference between the lattice vector parameters $(m-n)$ increases, the periodicity wavelength described in Chapter 2 also increases, resulting in an expanded unit cell and a correspondingly smaller Brillouin zone. This comprehensive analysis of the electronic spectra provides a robust foundation for exploring the advanced properties and applications of graphene-based materials.

Chapter 5

Conclusion

The primary objective of this research was to investigate the effect of altering the twist angle in twisted bilayer graphene on its intricate geometry, energetics, and electronic properties, thereby providing a comprehensive understanding of how this variation influences the material's fundamental characteristics.

Our investigation of twisted bilayer graphene yielded several key findings. In Chapter 2, we identified distinct patterns and symmetries in the relationship between unit cell size and twist angle. Chapter 3 focused on the energetic profiles of TBG across various twist angles, employing two different potentials: Lennard-Jones (LJ) and Kolmogorov-Crespi (KC). Both potentials demonstrated invariance with respect to the twist angle, with the KC potential providing more accurate results. This stability is attributed to the averaging effect of the energies corresponding to various local stacking regions. Chapter 4 focused on analyzing the electronic spectrum and band structures of diverse TBG configurations. We identified flat bands at magic angles and computed the variation of Fermi velocity and effective mass of electrons, along with other important parameters, as a function of twist angles. Moreover, we detected multiple band crossings at the zero energy level for particular angles, highlighting the complex behavior of electrons in TBG.

These observations significantly enhance our understanding of the fundamental properties of TBG and provide unique insights that could drive further research in this field. Future studies could build on our findings by incorporating relaxation effects, which were not considered in our analyses. Additionally, the use of more advanced hardware would facilitate computations for larger unit cells corresponding to smaller twist angles, potentially revealing even more intricate behaviors and properties.

To sum up, this study provides a comprehensive analysis of the structural, energetic, and electronic properties of twisted bilayer graphene, emphasizing the critical role of twist angles and local stackings. These findings have significant implications for material science and potential technological advancements, particularly in applications for advanced electronic devices and quantum computing.

Bibliography

[1] Y. Cao, V. Fatemi, S. Fang, K. Watanabe, T. Taniguchi, E. Kaxiras, and P. Jarillo-Herrero, "Unconventional superconductivity in magic-angle graphene superlattices," *Nature*, vol. 556, no. 7699, pp. 43–50, 2018.

[2] A. H. Castro Neto, F. Guinea, N. M. R. Peres, K. S. Novoselov, and A. K. Geim, "The electronic properties of graphene," *Rev. Mod. Phys.*, vol. 81, pp. 109–162, Jan 2009.

[3] Y. Cao, V. Fatemi, S. Fang, K. Watanabe, T. Taniguchi, E. Kaxiras, and P. Jarillo-Herrero, "Unconventional superconductivity in magic-angle graphene superlattices," *Nature*, vol. 556, p. 43–50, Mar. 2018.

[4] J. M. B. Lopes dos Santos, N. M. R. Peres, and A. H. Castro Neto, "Continuum model of the twisted graphene bilayer," *Physical Review B*, vol. 86, Oct. 2012.

[5] P. Moon and M. Koshino, "Energy spectrum and quantum hall effect in twisted bilayer graphene," *Phys. Rev. B*, vol. 85, p. 195458, May 2012.

[6] E. J. Mele, "Interlayer coupling in rotationally faulted multilayer graphenes," *Journal of Physics D: Applied Physics*, vol. 45, p. 154004, Mar. 2012.

[7] S. Shallcross, S. Sharma, E. Kandelaki, and O. A. Pankratov, "Electronic structure of turbostratic graphene," *Phys. Rev. B*, vol. 81, p. 165105, Apr 2010.

[8] M. Wen, S. Carr, S. Fang, E. Kaxiras, and E. B. Tadmor, "Dihedral-angle-corrected registry-dependent interlayer potential for multilayer graphene structures," *Phys. Rev. B*, vol. 98, p. 235404, Dec 2018.

[9] H. Li and W. K. Kim, "A comparison study between the lennard-jones and drip potentials for friction of graphene layers," *Computational Materials Science*, vol. 180, p. 109723, 2020.

[10] Y. Shibuta and J. A. Elliott, "Interaction between two graphene sheets with a turbostratic orientational relationship," *Chemical Physics Letters*, vol. 512, no. 4, pp. 146–150, 2011.

[11] K. Zhang and E. B. Tadmor, "Energy and moiré patterns in 2d bilayers in translation and rotation: A study using an efficient discrete–continuum interlayer potential," *Extreme Mechanics Letters*, vol. 14, pp. 16–22, 2017.

[12] J.-W. Jiang, B.-S. Wang, and T. Rabczuk, "Why twisting angles are diverse in graphene moiré patterns?," *Journal of Applied Physics*, vol. 113, May 2013.

[13] K. Uchida, "Energetics for twisted bilayer of circular graphene flake," *Journal of the Physical Society of Japan*, vol. 90, no. 4, p. 044602, 2021.

[14] A. N. Kolmogorov and V. H. Crespi, "Registry-dependent interlayer potential for graphitic systems," *Phys. Rev. B*, vol. 71, p. 235415, Jun 2005.

[15] Z. Kozioł, G. Gawlik, and J. Jagielski, "Van der waals interlayer potential of graphitic structures: From lennard–jones to kolmogorov–crespy and lebedeva models," *Chinese Physics B*, vol. 28, p. 096101, Sept. 2019.

[16] J. M. Campanera, G. Savini, I. Suarez-Martinez, and M. I. Heggie, "Density functional calculations on the intricacies of moiré patterns on graphite," *Phys. Rev. B*, vol. 75, p. 235449, Jun 2007.

[17] K. Uchida, S. Furuya, J.-I. Iwata, and A. Oshiyama, "Atomic corrugation and electron localization due to moiré patterns in twisted bilayer graphenes," *Phys. Rev. B*, vol. 90, p. 155451, Oct 2014.

[18] E. McCann and M. Koshino, "The electronic properties of bilayer graphene," *Reports on Progress in Physics*, vol. 76, p. 056503, Apr. 2013.

[19] K. S. Novoselov, A. K. Geim, S. V. Morozov, D. Jiang, M. I. Katsnelson, I. V. Grigorieva, S. V. Dubonos, and A. A. Firsov, "Two-dimensional gas of massless dirac fermions in graphene," *Nature*, vol. 438, p. 197–200, Nov. 2005.

[20] A. Rozhkov, A. Sboychakov, A. Rakhmanov, and F. Nori, "Electronic properties of graphene-based bilayer systems," *Physics Reports*, vol. 648, p. 1–104, Aug. 2016.

[21] L. E. F. Foa Torres, S. Roche, and J.-C. Charlier, *Introduction to Graphene-Based Nanomaterials: From Electronic Structure to Quantum Transport*. Cambridge University Press, 2014.

[22] Y. Zhang, Y.-W. Tan, H. L. Stormer, and P. Kim, "Experimental observation of the quantum hall effect and berry's phase in graphene," *Nature*, vol. 438, p. 201–204, Nov. 2005.

[23] P. E. Allain and J. N. Fuchs, "Klein tunneling in graphene: optics with massless electrons," *The European Physical Journal B*, vol. 83, no. 3, p. 301, 2011.

[24] C. H. Lui, Z. Li, Z. Chen, P. V. Klimov, L. E. Brus, and T. F. Heinz, "Imaging stacking order in few-layer graphene," *Nano Letters*, vol. 11, pp. 164–169, 01 2011.

[25] A. H. Castro Neto, F. Guinea, N. M. R. Peres, K. S. Novoselov, and A. K. Geim, "The electronic properties of graphene," *Reviews of Modern Physics*, vol. 81, p. 109–162, Jan. 2009.

[26] E. McCann and V. I. Fal'ko, "Landau-level degeneracy and quantum hall effect in a graphite bilayer," *Physical Review Letters*, vol. 96, Mar. 2006.

[27] J. M. B. Lopes dos Santos, N. M. R. Peres, and A. H. Castro Neto, "Graphene bilayer with a twist: Electronic structure," *Physical Review Letters*, vol. 99, Dec. 2007.

[28] G. Trambly de Laissardière, D. Mayou, and L. Magaud, "Localization of dirac electrons in rotated graphene bilayers," *Nano Letters*, vol. 10, p. 804–808, Feb. 2010.

[29] S. Shallcross, S. Sharma, and O. A. Pankratov, "Quantum interference at the twist boundary in graphene," *Phys. Rev. Lett.*, vol. 101, p. 056803, Aug 2008.

[30] G. Trambly de Laissardière, D. Mayou, and L. Magaud, "Numerical studies of confined states in rotated bilayers of graphene," *Physical Review B*, vol. 86, Sept. 2012.

[31] E. Suárez Morell, J. D. Correa, P. Vargas, M. Pacheco, and Z. Barticevic, "Flat bands in slightly twisted bilayer graphene: Tight-binding calculations," *Phys. Rev. B*, vol. 82, p. 121407, Sep 2010.

[32] R. Bistritzer and A. H. MacDonald, "Moiré bands in twisted double-layer graphene," *Proceedings of the National Academy of Sciences*, vol. 108, p. 12233–12237, July 2011.

[33] V. Ariel and A. Natan, "Electron effective mass in graphene," 2012.